DESIGN, PARAMETER OPTIMIZATION AND IN VITRO EVALUATION OF IMPLANTABLE MEDICAL DEVICES

by

Yanfei Chen

B.S., Peking University, 2012

Submitted to the Graduate Faculty of

the Swanson School of Engineering in partial fulfillment

of the requirements for the degree of

Doctor of Philosophy

University of Pittsburgh

2018

UNIVERSITY OF PITTSBURGH

SWANSON SCHOOL OF ENGINEERING

This dissertation was presented

by

Yanfei Chen

It was defended on

April 16, 2018

and approved by

Dr. Youngjae Chun, Associate Professor, Industrial Engineering, University of Pittsburgh, Pittsburgh, PA

Dr. Bopaya Bidanda, Ernest E. Roth Professor and Chairman, Industrial Engineering, University of Pittsburgh, Pittsburgh, PA

Dr. Woon-Hong Yeo, Assistant Professor, George W. Woodruff School of Mechanical Engineering, Georgia Institute of Technology

Dr. Sung Kwon Cho, Associate Professor, Mechanical Engineering and Materials Science, University of Pittsburgh, Pittsburgh, PA

Dr. Paul W. Leu, Associate Professor, Industrial Engineering, University of Pittsburgh, Pittsburgh, PA

DESIGN, PARAMETER OPTIMIZATION AND IN VITRO EVALUATION OF IMPLANTABLE MEDICAL DEVICES

Yanfei Chen, PhD

University of Pittsburgh, 2018

The number of implantable medical devices ranging from dental implants to cardiovascular implants has been exponentially increased in the last decades and various materials including metallic materials and polymeric materials are used in medical device manufacturing. In metallic materials, nitinol is widely used due to its superelasticity and well-known biocompatibility. Finite element modeling (FEM) along with *in vitro* and *in vivo* is being adopted to evaluate the medical device performance in patients and optimize medical designs.

In this dissertation, four innovative implantable medical devices were developed and their performances were evaluated using finite element modeling and *in vitro* testing: 1) ventriculoamniotic shunt for aqueductal stenosis treatment. It has the conduit to drain excessive cerebrospinal fluid (CSF) to lower intracranial pressure in fetal brains and the anchors to prevent the device dislocation during the treatment. The shunt tube design was optimized using computational fluid dynamics calculations. The anchor design was determined with ANSYS Static Structural and the prototype was manufactured based on modeling results. *In vitro* pressure and flow rate measurement within shunt device demonstrate that the pressure in fetal brain can be reduced by 95.2% while the pressure elevation in amniotic sac is negligible. 2) TFN flow-diverter integrated with flow sensing system for cerebral aneurysm post-treatment monitoring. The flexibility of TFN membrane was investigated using both computational modeling and stretching experiment. As the TFN was wrapped on a flow-diverter backbone with junction points, we evaluated the attachment patterns between a TFN and stent backbone. Finally, micro-scale flow sensor was designed and fabricated

based on the computational modeling. 3) compartmentalized stent to isolate the perfusion of the abdominal organs. The fluid dynamics inside the arterial and venous organ perfusion stent (OPS) was analyzed in terms of velocity distribution and wall shear stress (WSS). *In vitro* pressure difference both in arterial and venous OPS showed that the stent deployment with perfusion flow to the abdominal organs will not generate a significant load on the donor's heart. 4) retrievable stent graft for noncompressible hemorrhage control. The mechanical and biological properties of ePTFE membrane were investigated and the nitinol framed backbone was evaluated in terms of radial force.

TABLE OF CONTENTS

LIST OF TABLES

LIST OF FIGURES

PREFACE

Foremost, I would like to express my sincere gratitude to my advisor Dr. Youngjae Chun for the continuous support of my Ph.D studies and researches. Also I would like to thank the rest of my thesis committee: Dr. Bopaya Bidanda, Dr. Woon-Hong Yeo, Dr. Sung Kwon Cho and Dr. Paul Leu for their insightful suggestions.

My sincere thanks also goes to Dr. Bryan Tillman, Dr. Stephen Emery, Dr. Philip Carullo, Dr. Bryan Jankowitz for leading me working on diverse exciting projects.

I thank my previous and current lab members at University of Pittsburgh: Dr. Mahdis Shayan, Dr. Puneeth Shridhar, Moataz Mohsen Ah Elsisy, James Kern, Lacey Kostishack, Joseph Sukinik, Antonina Maxey for the help on the projects. I would like to thank all my friends at University of Pittsburgh, in particular, Dr. Junqi Yuan, Dr. Jian Feng, Dr. Tongchuan Gao, Dr. Kai He, Hongyao Geng, Shan Gong, Ya-Tang Chuang, Yuwen Yang, Zhaohui Geng, Chaosheng Dong, Wei Wang, Liang Xu, Tong Zhang, Xiaoshi Guo, Lingbo Jiang. I also would like to express gratitudes to all my friends at Carnegie Mellon University and Peking University.

Last but not the least, I would like to thank my parents and family for the unconditional support throughout my life.

1.0 INTRODUCTION

Medical devices and implants have attracted attentions in the last decades and the number of medical devices are exponentially increased these years. According to the Implantable Medical Devices market Analysis and Trends - Product, Material - Forecast to 2025, the global implantable medical devices market is poised to grow at a compound annual growth rate (CAGR) of around 5.4% over the next decade to reach approximately $54.28 billion by 2025 [1]. Novel medical devices are also being developed with emerging techniques such as 3D medical printing for customization and personalization [2] and nanofabrication for ultra-thin and low-profile medical devices [3].

1.1 TYPES OF MEDICAL DEVICES

The medical devices can be categorized into dental implants, orthopedic implants, cardiovascular implants, breast implants, intraocular lens, orthobiologics and other implantable products based on their applications.

1.1.1 Dental implants

Dental implants are inert, alloplastic materials for tooth loss management and lost orofacial structures replacement aid as a result of trauma, neoplasia and congenital defects. Endosseous comprising a single and discrete implant unit in the forms of screw or cylinder placed within dentoalveolar or basal bone is the most common dental implant. The most common materials of dental implants are commercially pure titanium or titanium alloy. Al-

ternative materials include ceramics such as aluminum oxide and other alloys such as gold and nickel-chrome-vanadium [4].

1.1.2 Orthopedic implants

An orthopedic implant is to replace a missing joint or bone or to repair a damaged bone. The most common types of orthopedic implants include pins, rods, screws and plates which are used to anchor fractured bones during the healing process [5]. The implant strain needs to be monitored regularly as indicators of potential fatigue failure as body movements and body weights impose a dynamic load upon implanted orthopedic devices [6].

1.1.3 Cardiovascular implants

Cardiovascular devices are used to diagnose and treat heart diseases such as strokes and associated health problems. Typical cardiovascular implants include aortic valve, cardiovascular conduit, mitral valve, tricuspid valve, vascular graft, cardiovascular occluder and pulmonary valve. The major complications associated with cardiovascular devices are infection and thromboembolism [7].

1.1.4 Intraocular lens

Intraocular lenses are medical devices implanted inside the eye to replace the eye's natural lens when it is removed during he surgery. They are also used in the vision correction surgery to restore a patient's eyesight. The evaluation of the optical performance and aberrations of the human eyes have been the research focus for many years and new advances in wavefront technology have allowed measurements that can quantitatively describe the optical performance [8].

1.2 MATERIALS FOR MEDICAL DEVICES

There are specific requirements that medical implants must meet for long-term use in the human body. Thus, a device must be properly "packaged" before installation in the human body. A wide of variety of polymers can be used in manufacturing biomedical implants and packaging devices including Polyvinylidene Fluoride (PVDF), Polyethylene (PE), Polypropylene (PP), Poly(methyl methacrylate) (PMMA), Silicones Parylene and PDMS, Polyurethane (PU), Polytetrafluoroethylene (PTFE), Polyamide (PA), Polyimide, Liquid Crystal Polymer (LCP) and Carbon Nanotube (CNT) Composites. The comparisons between these polymer materials can be found in [9].

Another category of widely used materials for medical devices are metallic materials including stainless steel, magnesium, titanium and nickel-titanium. Metallic implants can usually machine milled, cast and forged. These medical devices manufactured from metals range from simple wires and screws to fracture fixation plates and total joint prostheses (artificial joints) for hips, knees, shoulders, ankles, and so on. In addition to orthopedics, metallic implants are used in maxillofacial surgery, cardiovascular surgery, and as dental materials. Although many metals and alloys are used for medical device applications, the most commonly employed are stainless steels, commercially pure titanium and titanium alloys, and cobalt-base alloys [10].

Nickel-titanium, also known as nitinol, is a metal alloy of nickel and titanium in roughly equal atomic percentages. Since the initial discovery of nitinol in 1963 [11], the shape memory properties of the nitinol have been widely applied in a wide range of medical devices, specifically endovascular devices such as guidewires, stents, vena cava filters and arterial septal defect closure devices [12, 13, 14, 15, 16]. All the important device characteristics can be attributed to the specific properties of nitinol such as elastic deployment, thermal deployment, kink resistance, constant stress, dynamic inference, stress hysteresis, temperature dependence of stress, and other equally important properties of MRI compatibility, biocompatibility and corrosion rate [17]. We discussed some key properties of nitinol in the sections below.

1.2.1 Shape memory and superelasticity

The shape memory response is defined as a mechanical deformation in a low temperature state (i.e., martensite) with the deformations being fully recovered when the material is heated to the transformation temperature (i.e., austenite). nitinol material properties can be characterized by a specific stress-strain diagram different from conventional materials. Figure 1 shows the schematic diagram of stainless steel, nitinol and living tissues. Stainless steel has the elastic strain of below than 0.5% and shows plastic strain deformation once it exceeds the elastic limit. In the plastic deformation region, the materials show a permanent deformation and cannot be recovered after the stress is released. In the case of nitinol, the deformation is also linearly proportional to the applied stress in the early stage. Thereafter, the stress shows a plateau in the stress strain diagram and the strain is increased without a significant increase in the stress. During the unloading, it also shows a plateau in the stress, but with a different path in the diagram. Nitinol is recoverable up to 8% of deformation [18]. Living tissues such as bones also exhibit hysteresis in the loading-unloading cycles and this similarity contributes to the biomechanical compatibility of nitinol in the medical implants.

An example of shape memory property in nitinol is self-expanding vascular stents. A conventional vascular stainless steel with balloon expansion does not expand uniformly and a rigid non-uniformly expanded stainless steel stent often causes significant arterial wall injury as well as thrombosis formation. While the nitinol stents exhibit a more uniform expansion and can prevent undesirable changes in stent position despite the vessel movements [20]. Therefore, lower vascular injury resulting from the mechanical action of nitinol stents on the vessel wall is associated with a tremendous reduction in their thrombogenic potential compared to stainless steel stents. Self-expanding nitinol stents are manufactured from a diameter larger than that of the target vessel and the transformation temperature is typically set to 30°C. They can be easily collapsed below room temperature in a delivery system such as catheters. The stent is often constrained by a retractable sheath or by other means in order to prevent premature expanding during the delivery. At the target vessel site, the stent is deployed from the delivery system and expands until it hits the vessel wall and conforms to the shape of vessels. The stent now becomes superelastic at body temperature [21].

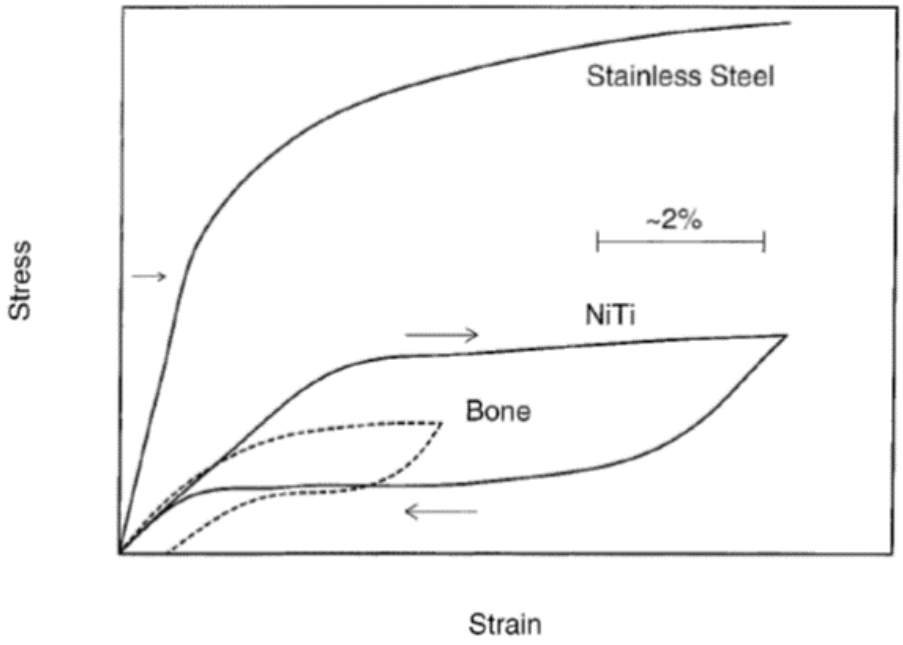

Figure 1: Stress-strain diagram (schematic), for living tissues, NiTi superelastic alloy and stainless steel (the left arrow indicates the elastic limit in stainless steel) [19].

1.2.2 Biocompatibility and surface treatment

The biocompatibility of nitinol material has been extensively investigated. An *in vitro* study conducted by Ryhänen *et.al* concluded that nitinol has good compatibility with human osteoblasts and fibroblasts. Despite the higher initial nickel dissolution, which is the main cause of allergic contact dermatitis, nitinol induced no toxic effects, decrease in cell proliferation, or inhibition on the growth cells in contact with the metal surface [22].

The biological response to implant materials is directly related to their surface conditions. Specifically, parameters such as chemical composition, crystallinity and heterogeneity, roughness and wettability are all of great importance for biological response. Therefore, surface treatment and modification can be used to improve the biological response to implant materials.

Table 1: Surface treatments of the thin film nitinol

Symbol	Treatment methods
Pretreatments	
CT	Cleaning: cleaning with acetone, methanol, and alcohol
PT_1	Pretreatment 1: passivated in HNO_3 for 40 min
PT_2	Pretreatment 2: placed in BOE and passivated in HNO_3 for 40 min
Surface treatments	
UVT_a	Treated with UV for 15-60 min
$TT_{b,c}$	Treated thermally at 300-600 °C in 10-40 min
$HPT_{d,f,g}$	Treated with 3%-30% H_2O_2 at 25-110 °C for 0-15 h

Chun *et al.* proposed a superhydrophilic surface treatment in thin film nitinol (TFN) to reduce thrombogenic behavior in thin film nitinol devices [23]. The thin film samples were surface treated using one of the following three processes shown in Table 1. For each surface treatment study, hydrophilicity was determined by measuring the wetting angles produced by a water droplet on the film surface. Among the three processes, hydrogen peroxide treatment (HPT) of 30% H_2O_2 solution at room temperature (25°C) for 15 h shows that superhydrophilic response is not associated with an increased brittleness as well as a sufficient titanium oxide layer on the film. In an *in vitro* platelet assay study, superhydrophilic treated TFN (S-TFN) demonstrated neither platelet adhesion nor aggregation over time. An S-TFN covered stent was placed in a 3.5 mm diameter left external iliac artery in a swine model. S-TFN covered stent was observed to remain patent and rapidly endothelialized. This neointimal growth suggests that the small amount of platelet adhesion on S-TFN contributes to the healing process [24]. As thrombotic complications represent the key problems in the management of vascular diseases, the TFN covered stent with a superhydrophilic surface treatment may reduce the incidence in-stent thrombosis.

The main challenges regarding the materials in implantable medical devices are biocompatibility and device delivery. The biocompatibility issue always occurs at the interface between implants and tissue or blood. The device materials should cause very little or no

long-term damage to the artery and a long-term inflammation response from the surrounding tissues. As most of the medical devices are fabricated from rigid or 'hard" materials, the sharp edges and corners in the medical device might impose serious damages to the relatively soft tissues during the surgical placement and implantation. In addition, these implantable medical devices are quite bulky and could cause disturbance in the blood flow or even significant coagulation or clot after being implanted in the blood vessels. As the new trends of minimally invasive techniques in both vascular and orthopedic applications enable the device to be delivered with a tiny puncture either in the blood vessel, tissue, or bones. These techniques reduce the hospital stay of the patients, as well as reduce the risk and pain from open invasive surgical procedures. While these techniques are a new trend and are widely used for various implantable devices, rigid and bulky devices cannot be delivered via these methods. Therefore, the 'new generation" implantable medical devices should address these issues with low-profile, and the use of soft and biocompatible materials.

1.3 FINITE ELEMENT MODELING

Finite element modeling (FEM) is a numerical method to solve the problems including structural analysis, heat transfer, fluid dynamics and electromagnetic fields, where the analytical solution is typically intractable. FEM formulates the problems into finding the solutions in a system of algebraic equations by dividing the domain of interest into discrete number of elements. FEM is widely used in medical device design and parameter optimizations, among which structural analysis is the most common area of interest for device mechanical characteristics prediction. The governing equation for structure in static equilibrium is defined by

$$[K]\{u\} = \{F\} \tag{1.1}$$

where $[K]$ is the stiffness matrix defined by the material properties, $\{u\}$ is the nodal displacement vector, and $\{F\}$ is the associated load vector.

FEM has been employed to investigate the mechanical properties of various stent designs ranging from balloon expanding stents to nitinol self-expanding stents under different loadings such as crimping, deployment and bending in tortuous vessels. The physics in the stent behaviors can be very complicated and FEM can be used to optimize the device design.

Larry et al. compared two different stent designs in terms of induced levels of stress in the vascular wall. The coronary artery was modeled as an idealized vessel and represented by a cylinder. Arterial tissue and stenotic plaque were modeled using a 5-parameter third-order Mooney-Rivlin hyperelastic constitutive equation and the parameters were fitted by the data from tension test of human femoral arterial tissue. Deformable-deformable contact was used to describe the contact between the artery and the stent. It thereafter concludes that an optimum stent design should retract sufficiently to prevent overstressing the vessel wall but still maintain patency of the vessel and plaque scaffolding [25].

Wu *et al.* proposed an FEM to describe the expansion of a balloon expanding stent in a curved vessel and the interactions between the stent and vessels. During the simulations, conformity of the stent to the vessel, the minimum lumen area and the severest stenosis, tissue prolapse between the struts and the stress in the tissues were calculated. As the blood vessels are typically tortuous, stent bending is mainly attributed to tissue contact and link deformation [26, 27].

Auricchio *et al.* evaluated the outcome of carotid artery stenting in the target vessel model constructed from patient-specific images using finite element analysis [28]. The DICOM CTA images of a stenosed carotid bifurcation of a 83 years-old male patient were processed to generate an STL file defining the lumen profile. Three self-expanding stent designs with different configurations and sizes were evaluated and the stress induced to the vessel wall as well as lumen gain and the vessel straightening were adopted as measures of stenting impact on the vessel anatomy.

1.4 DISSERTATION OUTLINE

Figure 2(a) shows the outline of medical device designing and manufacturing. The research focus in this thesis dissertation is the design, modeling, parameter optimization and *in vitro* testing of the developed medical devices. Figure 2(b) shows the types of medical devices during my PhD researches and the red circled medical devices are the focus in this thesis dissertation.

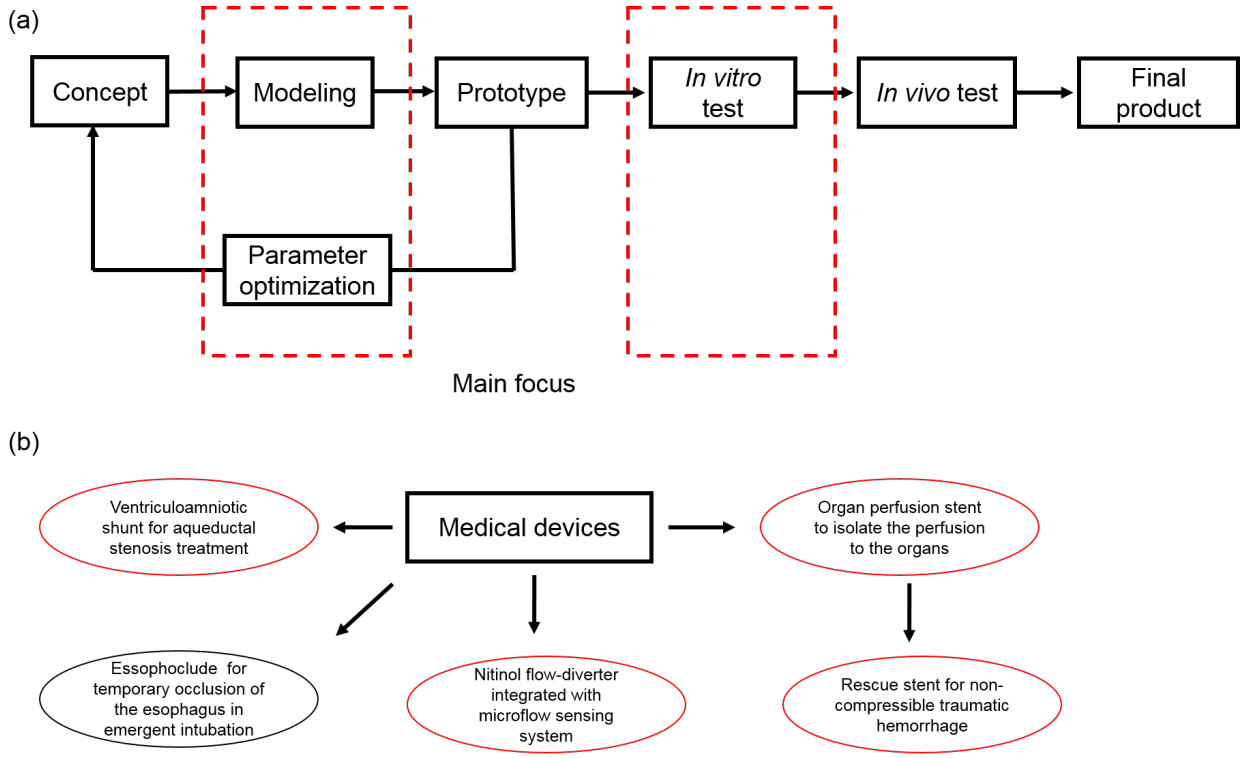

Figure 2: (a) Flow chart for medical device manufacturing process and red dashed box is main focus in this dissertation. (b) Medical devices investigated in this dissertation and red circled is the focus.

2.0 VENTRICULOAMNIOTIC SHUNT TO TREAT FETAL AQUEDUCTAL STENOSIS

2.1 INTRODUCTION

Children with an obvious pre-natal onset of hydrocephalus have been found to at high risk for early death and multiple neurological complications [29]. According to the published report, fetal hydrocephalus occurs at rate of 0.2-1 per 1,000 deliveries [30, 31, 32, 33]. AS is a neurodevelopmental anomaly that causes pressure hydrocephalus and subsequent neurological injury on developing neurons. Therefore, fetus with AS may benefit from decompression of the ventricular system to prevent ongoing brain damage. In-utero shunting was first attempted in the early 1980s as a means of improving pregnancy outcomes for fetal neuroanatomy, but later was abandoned due to a perceived lack of effect [34, 35], probably due to the poor patient selection and technical difficulties. Shunts were placed in fetus with lesions other than AS in the 1980s, leading to no clear benefit for shunting. Therefore, a moratorium was placed on fetal ventriculoamniotic shunting [36] and there has been no progress in treatment. Since there are no commercial available ventriculoamniotic shunts, current management for fetal hydrocephalus caused by AS involves either pre-term delivery followed by post-natal shunting or expectant management to term and then shunting. The problems associated with these management options are that they will place mothers and new-born babies at risks of disability or even death. In order to preserve the neurological functions and allow for normal brain development while the pregnancy progresses to term, a novel low-profile ventriculoamniotic shunt device needs to be developed for those fetuses with AS.

Emery *et al.* recently demonstrated the pre-natal detection for patient population with AS for shunting using both ultrasound and MRI techniques [37]. In that case, the in-utero ventriculoamniotic shunting can be performed on specific patient population to arrest brain injury while allowing the pregnancy to proceed to term and after which, standard ventriculoperitoneal shunting can be performed in the new-born period. The innovations of the proposed ventriculoamniotic shunt include the following aspects: (1) It has the conduit to drain excessive CSF to lower intracranial pressure in fetal brain; (2) The anchors can prevent the device dislodgement during the treatment; (3) The one-way valve prevents the reflux of CSF into the fetal brain to minimize potential complications.

2.2 METHODS

The schematic diagram of our proposed ventriculoamniotic shunt system implanted in a fetal brain is illustrated in Figure 3. The catheter tube serves as the conduit to drain the excessive CSF from the abnormal fetal brain to amniotic sac. Thermal shaped nitinol wires are attached to the catheter tube using a Nylon suturing method as the anchors to prevent device dislocation. The poly (ester urethane) ureas (PEUU) valve was partially fixed on the distal end of the catheter tube to prevent the reflux of CSF. A detailed fabrication process of the ventriculoamniotic shunt device is described in Section 2.4.1. The inset figure (in rectangular box) in Figure 1 demonstrates the ON and OFF states of the one-way valve. The PEUU valve remains closed (at OFF state) until the incoming CSF flow pushes it open (at ON state). Thus, only the flow from fetal brain to amniotic sac is allowed.

2.2.1 Materials

2.2.1.1 Shunt tube materials Two different types of commercially available catheter materials were used in prototyping. The 3 Fr and 4 Fr size tubes were obtained by mechanical cut-trim process from Neuroform3 Microdelivery Stent System (Boston Scientific, MA) and the Angiographic Catheter (SRD6913, Cordis, Johnson & Johnson Co., FL), respec-

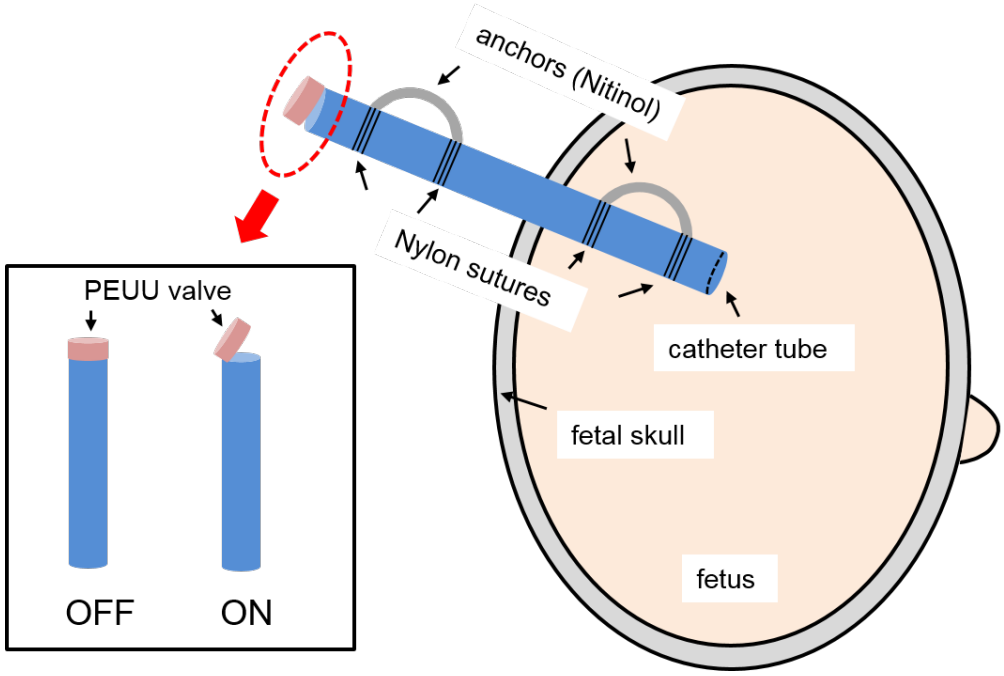

Figure 3: Schematic diagram of the proposed shunt system implanted in a fetal brain. The inset figure demonstrates the OFF and ON state of the micro PEUU valve. The dimensions of the shunt device are exaggerated as opposed to the fetal brain.

tively. These commercially available catheter materials are composites that contain multiple polymer layers with the ultra-thin braided metal wires and are commonly used in either neurovascular or coronary artery interventional. The catheter materials are one of the best options for the prototype shunt because they have great kink resistance along with a certain level of longitudinal flexibility, as well as biocompatibility.

2.2.1.2 Anchor materials Nitinol wires were used for fabricating anchors in ventriculoamniotic shunt prototypes. Nitinol is a common and well-known material widely used in implantable biomedical devices because of its shape memory effect, superelasticity and biocompatibility. After the rediscovery of the shape memory effect in equiatomic Ni-Ti in 1962, there has been an extensive research on this material. One of the most common reasons to use nitinol in a medical device is to allow the efficient deployment in a less invasive procedure

with its superelastic attribute. Most of the vascular disease treatment procedures require instruments and devices that can pass through very small openings and then elastically spring back into the desired shapes. Nitinol clearly allows the greatest freedom in design compared with other flexible materials [14]. The biocompatibility of the nitinol was also great. It has been confirmed that almost no toxic effects or decrease in cell proliferation can be observed, as well as there is no inhibiting effect on the growth of cells in contact with the metal surface for clinical uses [22].

Various cold-drawn supelastic nitinol wires (Nitinol Devices & Components, Inc., CA) were used for fabricating anchors. The elastic moduli of these wires are in the range of 41-75 GPa with the ultimate tensile strength of 1070MPa. The transformation temperature (i.e., Austenite finish temperature) is in the range between -25 and 30^{o}C. The composition between Nickel and Titanium is 55.8 wt.% and 44.2 wt.%, respectively.

2.2.1.3 Valve materials Biodegradable polyurethane materials have been applied in reconstruction of the cardiac valves and it showed satisfactory valvular functions [38]. PEUU has been shown to possess good biocompatibility with non-toxic degradation products and great elastomeric properties [39]. The PEUU was prepared by a two-step polymerization process whereby polycaprolactone diol, 1,4-diisocyanatobutane, and 1,4-diaminobutane were combined in a 1:2:1 molar ratio. In the first step, the pre-polymer was formed by reacting polycaprolactone diol with1,4-diisocyanatobutane. In the second step, the pre-polymer was reacted with 1,4-diaminobutane to extend the chain and to form the final polymer. The PEUU coating and PEUU valve were fabricated by electrospinning [40]. Briefly, PEUU was dissolved in 1,1,1,3,3,3-hexafluoroisopropanol (HFIP) at a concentration of 12% (w/v), and electrospun either directly onto the superelastic nitinol mesh anchor to achieve a thin layer of coating, or onto a rotating and translating stainless steel mandrel to yield a PEUU membrane. The feeding rate of the PEUU solution through a charged capillary was kept at 1.5 ml/h. The collecting target (nitinol anchor or rotating mandrel) was located 10 cm from the tip of the capillary. The voltage between the capillary and target was 19 kV.

2.2.2 *In vitro* assessment of both pressure and flow rates with the shunt devices

Figure 4 shows the test set-up for ventriculoamniotic shunt functionality assessment. The syringe itself on the syringe pump (Model 100 Series, Cole-Parmer, IL) mimics the fetal brain and the pump is used to mimic the pressure level increase in fetal brain. Either 3 Fr size of 4 Fr size device was connected to the test system to work as the shunt. The balloon was attached on one end of the device mimicking the amniotic sac. Two micro pressure sensors (Pendotech, NJ) were connected in the flow circuit to measure the pressure levels both in the artificial fetal brain and amniotic sac, respectively. The pressure signals were collected by a data acquisition system (NI USB-9162, National Instruments, TX) and recorded in Labview (National Instrument, TX). The flow rates in the shunt were measured by an accurate liquid flow sensor (SLI-2000, Sensirion, CA). We also connected a one-way valve between the syringe pump and flow sensor to manually control the incoming flow to the shunt to evaluate the shunt functionality by comparing the pressure levels without and with shunt.

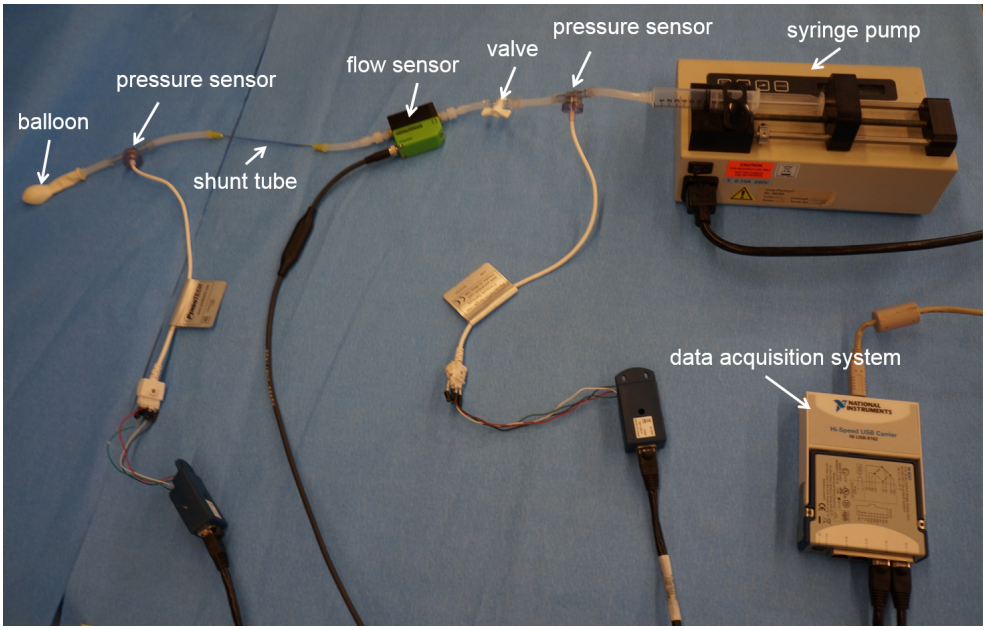

Figure 4: *In vitro* pressure and flow rate measurement set-up.

It was reported that cerebrospinal fluid (CSF) has the similar viscosity as water [41], so we used deionized (DI) water as the working fluid for the *in vitro* tests. First, the valve was closed and the pressure levels were increased in artificial fetal brain with the pump flow rate set as 50 mL/h. This experiment mimicked the gradual pressure elevation in fetal brain induced by the CSF accumulation. Both the pressure levels in fetal brain and amniotic sac were recorded after 7.2 s with total flow volume equal to 0.1 mL. This is marked as the control group without shunt. Next the pressure levels were restored to the initial values. Then, we turned on the valve and this process mimicked the shunting procedure. After all the pressure levels were stabilized, we turned on the syringe with the same settings. Again, this process mimicked the pressure elevation in fetal brain. And the corresponding pressure levels and flow rates were measured and recorded. This is marked as the group with the shunt.

2.2.3 Anchor functionality evaluation

The anchors functionality was evaluated by measuring the frictional force generated during the shunt movement in the fetal skull and this frictional force served to prevent the shunt dislocation. Figure 5 shows the top-view and front-view of the platform built on the isolation table. A 5mm thick polydimethylsiloxane (PDMS) membrane was fixed on the optics mount (Thorlabs, NJ), which acted as the simulating fetal skull due to their similar elastic modulus [42, 43]. The PDMS membrane was punctured with a needle to create the incision. The vertical translation stage with maximal travel distance 13 mm (Thorlabs, NJ) was used to provide the shunt advancement through the artificial fetal skull layer and the corresponding frictional force was measured by a load cell (LSB200, Futek, CA) mounted on the translation stage.

2.2.4 One-way valve functionality evaluation

The ventriculoamniotic shunt device contains a low-profile one-way valve fabricated by PEUU membrane. The functionality of this valve was qualitatively evaluated by visualizing the fluid flow around the valve area. The whole device was immersed in the saline solution then

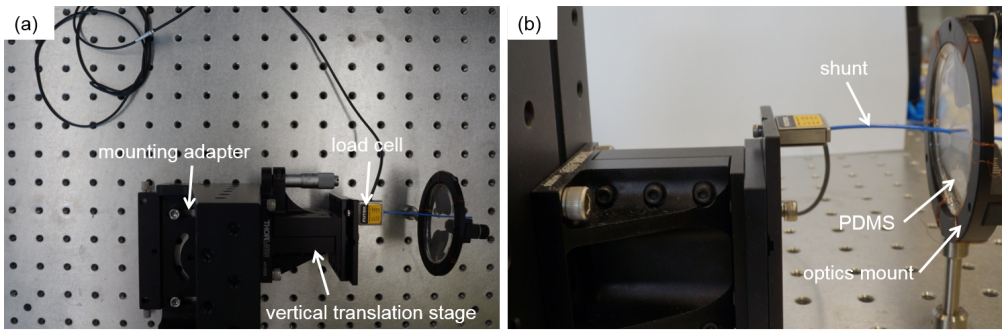

Figure 5: Anchor resistance force measurement set-up; (a) top-view and (b) front-view of the test system.

the red coloured food dye (Colorante rojo para alimentos, McCormick Culinary, MD) was injected into the shunt. Both the valve motion and red dye flow in saline solution were monitored under a high resolution digital camera (NEX-3, SONY, Japan) equipped with stereomicroscopy (SZ61, Olympus, PA) at 4.5 times magnification.

2.3 ANALYSIS

2.3.1 Theoretical analysis and computational fluid dynamics (CFD) modelling

For an incompressible flow in the circular tube, the pressure drop can be calculated by Darcy-Weisbach equation

$$\Delta P = f_D \cdot \frac{L}{D} \cdot \frac{\rho v^2}{2} \tag{2.1}$$

where f_D is Darcy friction factor, L and D is the length and diameter of the tube, ρ is the fluid density and v is the mean flow velocity of the liquid. For the laminar flow, Darcy friction factor f_D is related to the Reynolds number (Re) by

$$f_D = \frac{64}{\mathrm{Re}} \tag{2.2}$$

Therefore, the volume flow rate Q can be calculated analytically and the result is given as

$$Q = \frac{\Delta P \cdot \pi D^4}{128 \mu L} \tag{2.3}$$

For the turbulent flow with Reynolds number greater than 4,000, Darcy friction factor f_D is given by:

$$\frac{1}{\sqrt{f_D}} = -2 \log_{10} \left(\frac{\varepsilon}{3.7D} + \frac{2.51}{\mathrm{Re}\sqrt{f_D}} \right) \tag{2.4}$$

where ε is the roughness height. In this case, the volume flow rate Q needs to be calculated numerically.

The fetal intracranial and intrauterine pressure was reported to be 30-35 mmHg and 5-9 mmHg, respectively [44, 45]. Therefore, the pressure difference between the fetal brain and amniotic sac is estimated as 30 mmHg (4 kPa). Only the shunt tube was included in flow rate calculation and a simplified cylinder model in CFD calculations was employed to optimize the shunt design with maximal flow rate in the shunt when it was connected between the fetal brain and amniotic sac. The 4 kPa pressure difference between the inlet and outlet was maintained in the cylindrical tube (shunt) and the fluid in the tube has the density ρ =1000 kg m^{-3} and viscosity $\mu = 1.003 \times 10^{-4}$ Pa s^{-1} [46]. A laminar flow model was assumed for 3 Fr catheters and turbulent flow model for 4 Fr catheters. Then we were able to solve for the inlet velocity as well as flow rate for different length (from 3 cm to 10 cm with a 1 cm increment) and diameters (ID = 0.69 mm for 3 Fr catheter and ID = 0.94 mm for 4 Fr catheter).

2.3.2 Anchor resistance analysis

Nitinol wires with different pre-shaped structures will be attached on the outer surface of the catheter as an anchor to prevent the device dislocation by generating a sufficiently high frictional force. We assume that the frictional force is proportional to the support force when the anchor was compressed during the device movement through the skulls incision, so we can analyse the maximal compression force in the shunt movement. A line model with circular cross-section (diameter of the cross-section $d = 0.10$ mm) was employed in ANSYS Static Structural 15.0 (ANSYS Inc., Canonsburg, PA) (shown in Figure 6). The length of the

anchor L (mm) and the height H (mm) will be varied to evaluate the maximum compression force. Two vortices at two ends are assumed to be fixed and a downward displacement loading with the magnitude equal to H was applied in the middle section of the anchor. The material property of the nitinol is defined as Youngs Modulus $E = 60$ GPa and Poissons ratio ν =0.3. Then we are able to evaluate the compression force associated with the displacement.

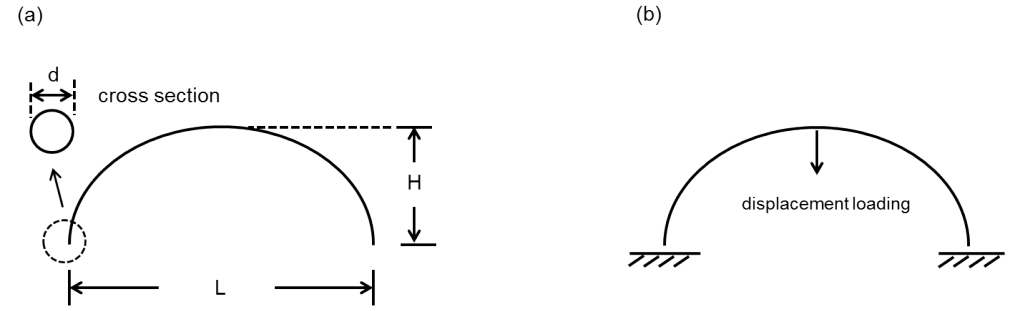

Figure 6: Simplified model to analyse anchor resistance in finite element modelling.

2.4 RESULTS AND DISCUSSIONS

2.4.1 Prototype devices

Figure 7 shows the first prototype shunt device with nitinol braided anchor. First, the commercially available catheter material (3 Fr catheter) was obtained by a precision mechanical cutting process in the required length as the shunt tube. Both ends were smoothed by eliminating any metal wires and burrs in composite structure with mechanical polishing and micro laser melting. Then, the ultra-thin nitinol wires (0.004-0.005" diameter) were integrated with the shunt tube using both biocompatible polymer adhesives and 7-11 size Nylon suturing materials as the anchor. The device can be easily collapsed into a PTFE tube with inner diameter 2 mm. The nitinol mesh will be released after compression due to the material superelasticity and it will prevent the device dislocation by deformation. Then all the anchor regions were covered with PEUU membrane with electrospun coating to prevent any leakage of the fluid flow.

Several prototype devices were designed and manufactured by integrating with three different anchor geometries, as shown in Figure 7. Anchor geometries were created with the ultra-thin nitinol wires (0.004-0.005") by thermal shape setting technique. Then, the anchors were attached on the middle of the shunt tube by mechanical clamping. As described earlier, both biocompatible polymer adhesives and 7-11 size Nylon suturing materials were used for the attachment. Figures 7(a-c) show the prototype devices with coiled spring anchors, two bumper anchors and two tilted elastic anchors, respectively. Finally, the PEUU membrane was partially attached on one end of the shunt tube using the micro-suturing methods with the size of 10-11 sutures (Figure 7(d)). This attached PEUU membrane functioned as the passive one-way valve of the ventriculoamniotic shunt device.

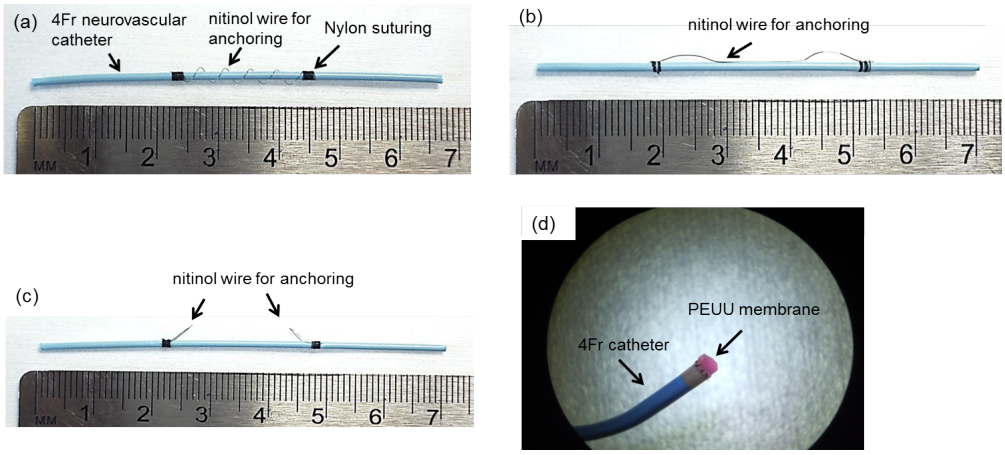

Figure 7: Prototype ventriculoamniotic shunt with anchors and one-way valve.

Figure 8 shows the deployment of the device *in vitro*. All three types of anchors can be easily collapsed and inserted into the 4 Fr size shunt tubes and successfully deployed with a 10 Ga needle simply by pushing the device using a push rod (Figures 8(a-d)). No significant damages or luminal side deformation were observed (Figure 8(d)). In the next section, we show the performance of the anchors by deforming upon compression to demonstrate the prevention of the device dislocation.

A new set of prototype device was also developed as shown in Figure 9(c) and (d). The new developed shunt device consists of two components, a cage at one end of the shunt tube to prevent tube occlusions and an anchor to prevent the device dislocation during the surgical

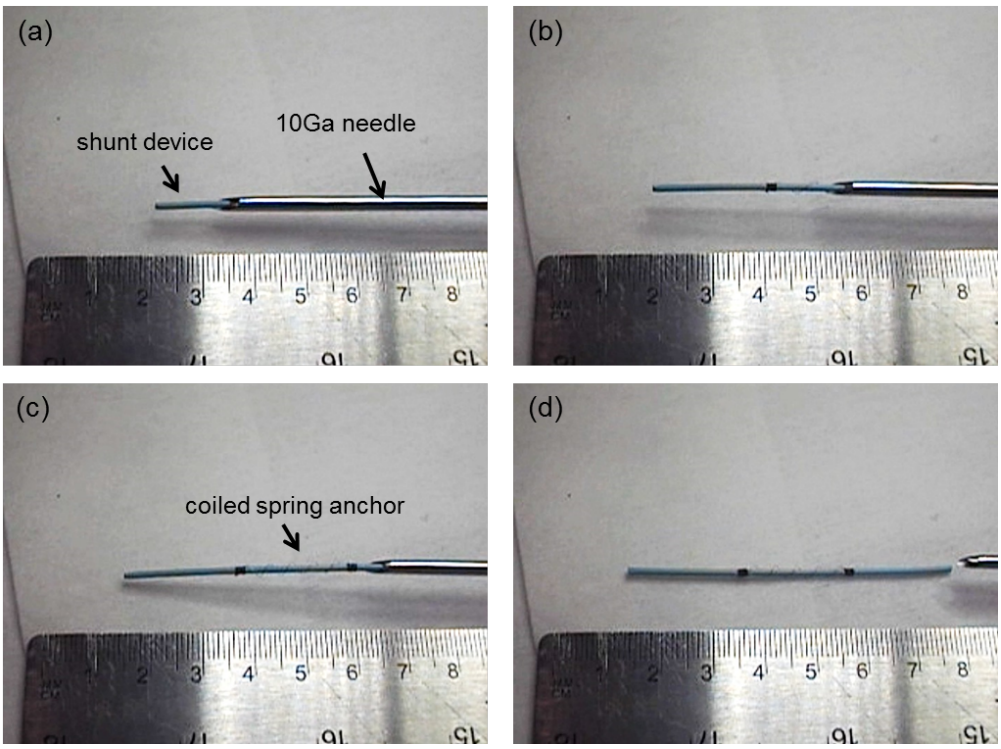

Figure 8: Captured images of the device deployment in a 10 Ga needle.

treatment. Both the cage and anchor were fabricated from nitinol wires (0.0090" diameter, NDC Inc., Fremont, CA, USA) and wrapped onto two types of aluminum rod (Figure 9(a). Stainless steel wires (Malin Co., Brook Park, Ohio, USA) were used to fix the nitinol wires on the lathed aluminum rod (Figure 9(b)). Then the whole parts were placed in furnace (Lindberg/Blue Moldatherm Box Furnaces, Fisher Scientific, Pittsburgh, PA, USA) with temperature set as 500° for 20 minutes. The nitinol wires were thermally set to the desired shapes as cages and anchors. Finally, the thermally shaped cage and anchor were attached on a 3 Fr catheter using the USP 6-0 Nylon sutures (Aros Surgical Instruments Corporation, Newport Beach, CA, USA) and biocompatible adhesive (Henkel, Stamford, CT, USA).

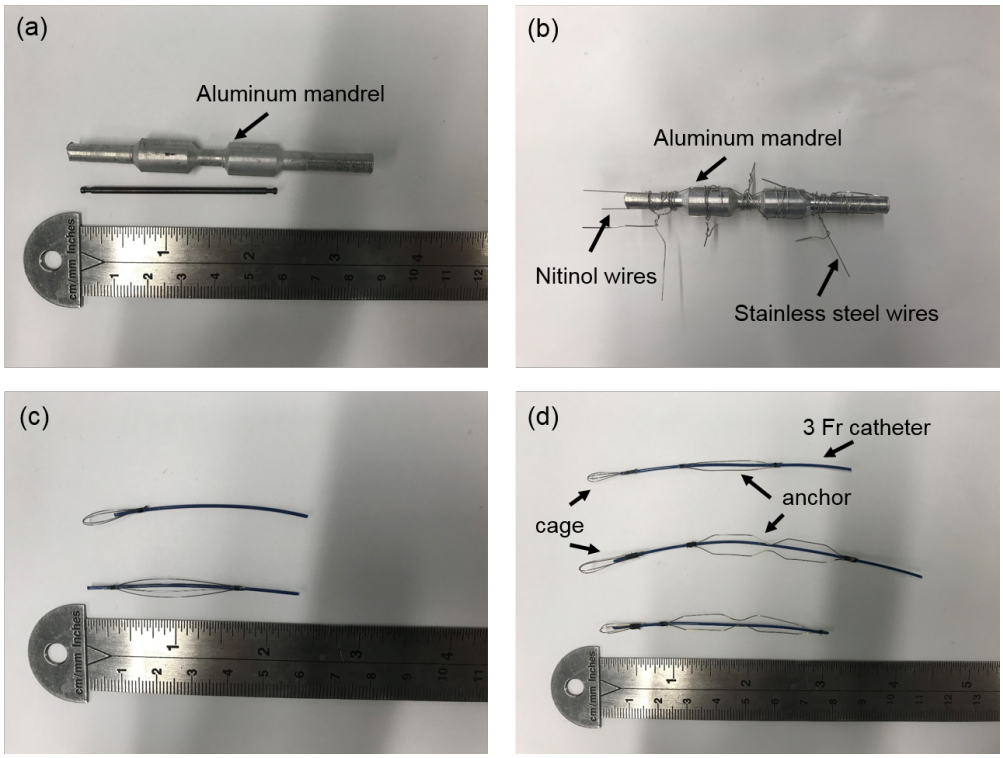

Figure 9: (a) Aluminum rods used for thermal shaping. (b) Wrapped nitinol wires on an aluminum rod for anchor fabrication. (c)-(d) Manufactured prototype shunt device with cages and anchors.

2.4.2 *In vitro* evaluation on pressure level and flow rate changes

2.4.2.1 Computational fluid dynamics (CFD) calculations Figure 10 shows the calculated flow rates with respect to different length (from 3 cm to 10 cm with a 1 cm increment) and diameters (ID = 0.69 mm for 3 Fr catheter and ID = 0.94 mm for 4 Fr catheter) of shunt tubes using both theoretical equations described above and CFD modeling. These results demonstrate that the flow rate increased with diameter and decreased with length of the shunt tube. Specifically, flow rate in a 4 Fr shunt decreased from ~1200 μL·s^{-1} to ~600 μL·s^{-1} when the shunt length was increased from 3 cm to 10 cm, while the flow rate in 3 Fr shunt decreased from ~450 μL·s^{-1} to ~200 μL·s^{-1}. Also, 4 Fr shunt shows a larger flow rate compared with 3 Fr shunt with the same length. The theoretical analysis results

also show the similar trends and CFD modeling results match quite well with it. Therefore, we can conclude that a catheter with a larger inner diameter and smaller length will be preferred as the candidate for shunt to drain maximal amount of CSF flows.

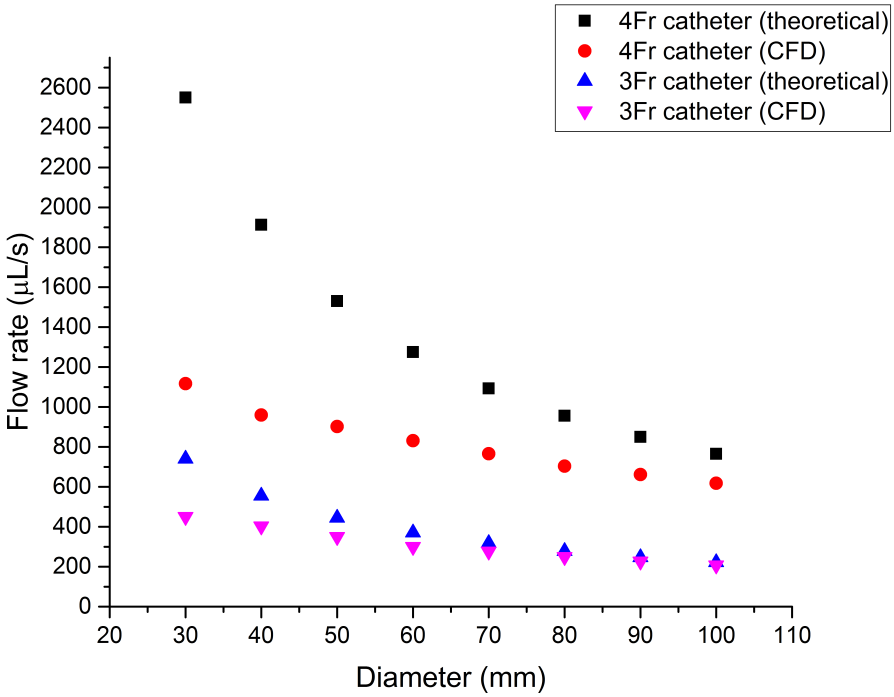

Figure 10: Calculated flow rate within device with respect to length and diameter of shunt tubes using theoretical equations and CFD modeling.

A shorter shunt will be challenging to be placed in the fetal skull, so longer shunts will be preferred in order to minimize the surgical difficulties in practice. Also a larger diameter of catheter will need a larger insertion needle, which means higher risks to the mother of premature labor, amniotic fluid leak, uterine trauma or placental separation and fetal brain trauma [47], so the 5Fr or larger catheters were not excluded in the shunt candidates. Taking these factors into account, a 7 cm long 4Fr catheter was finally chosen as the shunt candidate.

2.4.2.2 Pressure and flow rate measurement Figure 11 shows the measured pressure levels and flow rates with a 3Fr catheter (7 cm long) as the ventriculoamniotic shunt. The

initial pressure in the fetal brain was set as 0.86 psi and in the amniotic sac it was 0.24 psi. Therefore, the pressure difference between the two was 0.64 psi (32 mmHg). Figure 11(a) shows the pressure levels in the fetal brain with the valve closed, i.e. the control group. The pressure in the fetal brain ramped to as high as 4.2 psi with the syringe pump running for 7.2 s if the shunt was not connected in the system. The pressure elevation in fetal brain is 388% and this high pressure represented the high risk of fetal brain damage. Figure 11(b) shows the pressure levels in the fetal brain and amniotic sac with the valve open, i.e. the shunt was connected and functioning. We can see that the pressure level in fetal brain first dropped to $\sim$ 0.15 psi and the pressure level in amniotic sac slightly increased to $\sim$ 0.25 psi once we turned on the valve. The pressure redistribution occurred between the fetal brain and amniotic sac and the excess CSF drained from the brain to the amniotic sac. The corresponding flow rate in the shunt during this process was measured and represented by the peak value in Figure 11(c), which is 2237.2 μL min^{-1}. After all the pressure levels became stable, the pressure level in fetal brain only rose to $\sim$ 0.48 psi with the syringe pump running for 7.2 s. There was also a slight increase in the pressure level from 0.24 psi to 0.30 psi in the amniotic sac, as shown in Figure 11(b). Therefore, the pressure decrease in fetal brain is 88.6% (from 4.2 psi to 0.48 psi) while the pressure elevation in the amniotic sac is 25%.

Figure 12 shows the measured pressure level and flow rate with 4 Fr catheter (7 cm) as the ventriculoamniotic shunt. The initial pressure levels in fetal brain and amniotic sac were still set as 0.86 psi and 0.24 psi, respectively. Figure 12(a) shows that the pressure in fetal brain dropped suddenly to $\sim$ 0.15 psi after turning on the valve. The corresponding flow rate in the shunt during this process was represented by the peak value in Figure 12(b), which is 4134.6 μL min^{-1}. This flow rate is larger than the one in the 3 Fr case. Then, the pressure level in fetal brain slowly increased to $\sim$ 0.2 psi with the syringe pump running for 7.2 s. There was also a slight increase in the pressure level from 0.24 psi to 0.29 psi. Therefore, the pressure decrease in fetal brain is 95.2% (from 4.2 psi to 0.2 psi) and the pressure elevation in the amniotic sac is 20.8%.

The pressure measurement demonstrates that the ventriculoamniotic shunt relieved the high pressure in the fetal brain with draining the excess amount of CSF to the amniotic sac.

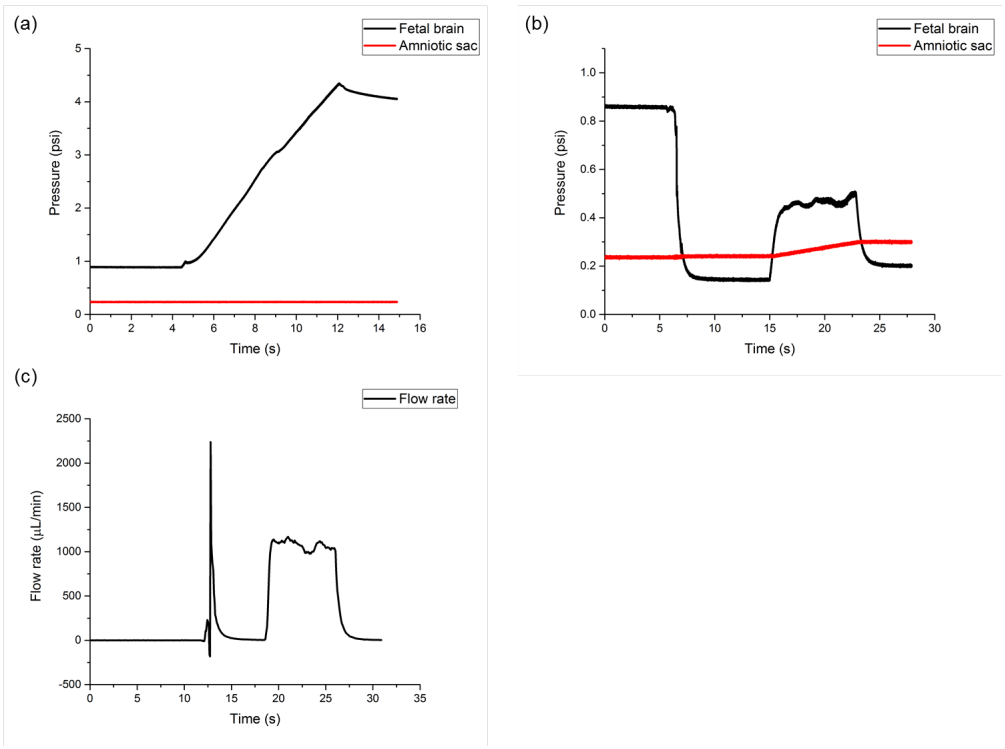

Figure 11: (a) Pressure levels in the simulated fetal brain and amniotic sac in control group; (b) Pressure levels in the simulated fetal brain and amniotic sac with 3 Fr catheter shunt device; (c) Flow rate in the 3 Fr shunt device.

Further pressure increase in fetal brain will also be relieved after inserting the shunt. We can see that 4 Fr shunt shows superior performance on CSF draining and pressure relieving. This result matches well with our theoretical analysis. The measured peak flow rates for 3 Fr and 4 Fr shunt are much lower than the CFD calculations, mostly because we did not take the length of silicone tube in the experiment as well as frictional loss in the tube connections into account in our calculations. Considering all the factors, the 4 Fr catheter proves to be a good candidate for the ventriculoamniotic shunt. It can relieve 95.2% of the abnormal high pressure in foetal brain while only increasing the amniotic sac pressure by 20.8%. The actual amniotic sac size is much larger than the fetal brain, so the impact on the amniotic sac will be negligible.

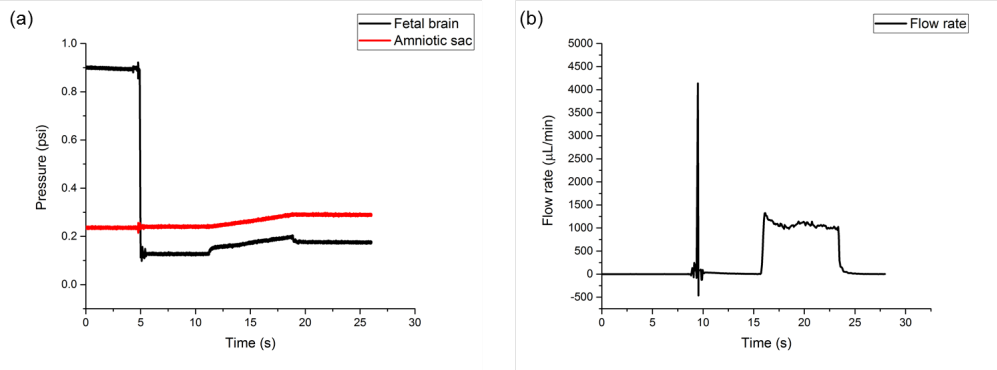

Figure 12: (a) Pressure levels in the simulated fetal brain and amniotic sac in control group; (b) Pressure levels in the simulated fetal brain and amniotic sac with 4 Fr catheter shunt device; (c) Flow rate in the shunt device.

2.4.3 Anchor functionality

2.4.3.1 Finite element (FE) analysis of anchors In order to evaluate the effect of anchor height and length on the compression force, we varied the anchor height from 1 mm to 4 mm with fixed length L= 8 mm and the result is shown in Figure 13(a). An asymptotic function was fit to the results in Origin 2015 (OriginLab, Northampton, MA) and the data reveals that increasing the anchor height will elevate the generated compression force, but the improvement is not significant after the height is beyond 4 mm. We also varied the anchor length from 10 mm to 30 mm with fixed height H =1 mm and the result is shown in Figure 13(b). An exponential function was fit, which shows that decreasing the anchor length will increase the generated compression force significantly. Therefore, we may conclude that an anchor design with larger height and lower length provides the optimal frictional force during the movement. However, considering the manufacturing difficulty and performance improvement, a height between 3-4 mm and length between 5-10 mm were considered as the design parameters.

This FE analysis only applies to the two bumper anchor structure (Figure 7(b)), while the behaviors for coiled spring and tilted curves are more complicated since other deformations

such as twisting will be involved when the anchor part moves through the PDMS membrane. Therefore, more complicated boundary conditions need to be considered for the FE analysis in more realistic situations.

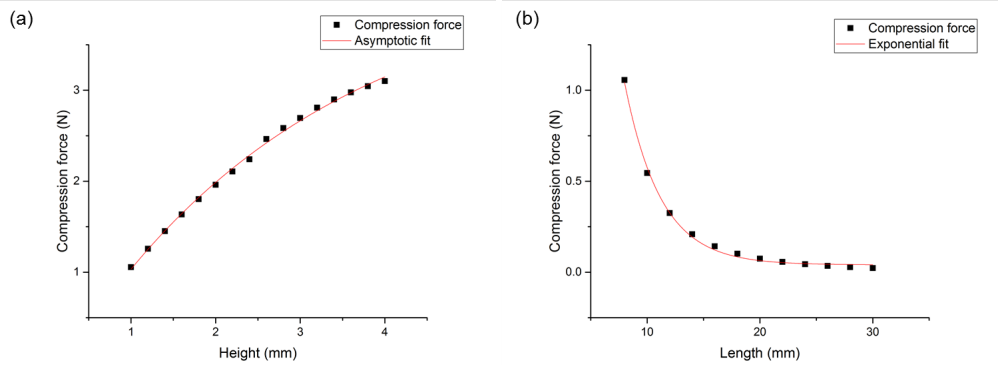

Figure 13: Calculated compression force by anchor with respect to length and height in finite element analysis.

2.4.3.2 Force measurement of the anchors Three prototype shunts with different anchor designs were evaluated for anchor functionality. If the shunt anchor is effective in preventing the dislocation, then it will generate higher frictional force during the shunt movement in the PDMS membrane. According to this assumption, we measured the force in three prototype shunts with different anchor designs shown in Figure 7. In order to evaluate the effectiveness of several anchor designs, we compared the measured frictional forces in different prototype anchors. Although PDMS may not provide the same surface condition as the one of fetal skull in terms of frictional coefficients, it does not influence our comparison results on anchors.

Figure 14(a) shows the the measured force for prototype with coiled anchors (Figure 7(a)). The black line represents the corresponding frictional force when only the bare shunt (no anchor) region was pushed through the PDMS membrane and the averaged force is 0.18 N. The red line represents the corresponding frictional force when the anchor region was pushed through the PDMS membrane and the averaged force is 0.27 N. It shows that the presence of anchor provided 0.1 N frictional force to prevent the shunt dislocation during the

surgery operation. Figure 14(b) shows the measured force for prototype with two bumpers (Figure 7(b)). The shunt anchor region first went through the PDMS membrane and the averaged frictional force is 0.15 N (left on the red dashed line). Once the no-anchor region was pushed through the PDMS membrane, the frictional force abruptly ramped to 0.20 N (right on the red dashed line). The frictional force on the anchor region is lower than the no anchor region, possibly due to the smoother nitinol anchor region compared to the bare catheter. Therefore, the anchor shows no effects to prevent the shunt dislocation. Figure 14(c) shows the measured force for prototype with two tilted curves (Figure 7(c)). The movement pattern is similar. First the shunt anchor region was pushed through the PDMS membrane and the frictional force generated by the anchor is up to 1.0 N (left on the red dashed line). After the anchor passed the PDMS membrane, the frictional force ramped down to 0.2 N (right on the red dashed line). Therefore, a prototype anchor with tilted curves provided an additional ∼0.80 N frictional force to prevent the shunt dislocation.

2.4.3.3 One-way valve functionality The one-way passive used in the ventriculoamniotic shunt was adopted from the geometry of bi-leaflet valve [48]. Figure 15 shows the finite element modelling results of the simplified one-way valve in ANSYS Workbench Static Structural 15.0. The Youngs Modulus for valve material is 3 MPa with Poissons ratio 0.49 and Youngs Modulus is 1 GPa with Poissons ratio 0.46 for catheter material. Figure 15(a) shows that the poly(ester urethane) urea (PEUU) valve is deformed outward and pushed open with the forward flow. Figure 15(b) shows that the PEUU valve is deformed inward and remains closed with the reversed flow. Therefore, it proves the functionality of the passive one-way valve in allowing the forward flow while resisting the reversed flow.

Figure 16 shows the in vitro testing result of the one-way valve with flow visualisation. Figures 16(a-c) show that the injected red dye into the shunt tube created high pressure and forwarded the flow to push the PEUU membrane valve open. Therefore, the red dye diffused into the clear DI water in all directions through the gap between the valve and end of the tube. Due to the elasticity of the PEUU membrane, the valve restored to its original position (Figure 16(d)) when the red dye flow in the shunt stopped. There was no flow observed around the shunt when the valve was closed. This flow visualisation is a qualitative

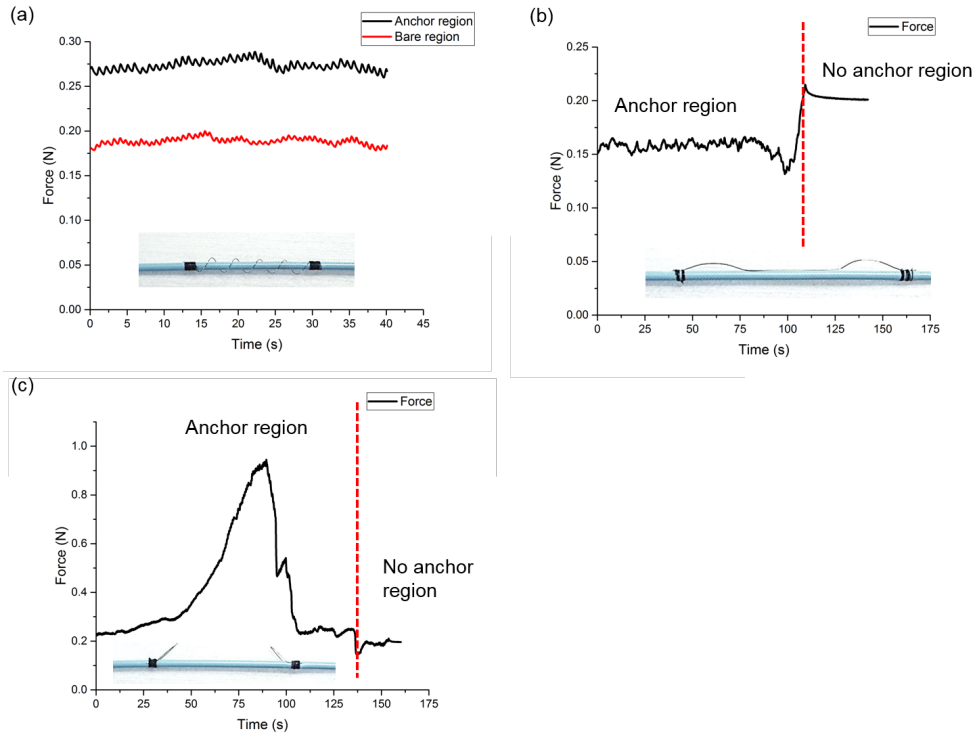

Figure 14: Anchor force measurement results. (a) Frictional force on the anchor region and bare shunt region for coiled spring anchor structure. (b) Frictional force on the anchor region and no anchor region for two bumpers anchor structure. (c) Frictional force on the anchor region and no anchor region for two tilted curves anchor structure.

way to show the proof-of-concept of the valve testing that confirmed the functionality of the one-way valve for controlling the flow in the shunt device. And the experimental and modeling results agreed with each other.

2.5 CONCLUSIONS

In this study, we proposed an improved shunt design to readdress the concept of ventriculoamniotic shunting for fetal isolated aqueductal stenosis. The low-profile prototype ventricu-

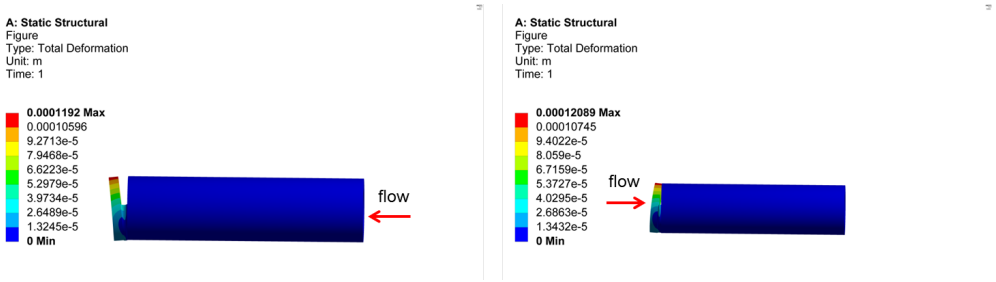

Figure 15: Finite element modelling of the one-way valve in ANSYS Workbench 15.0. (a) The valve is open with forward flow. (b) The valve is closed with reversed flow.

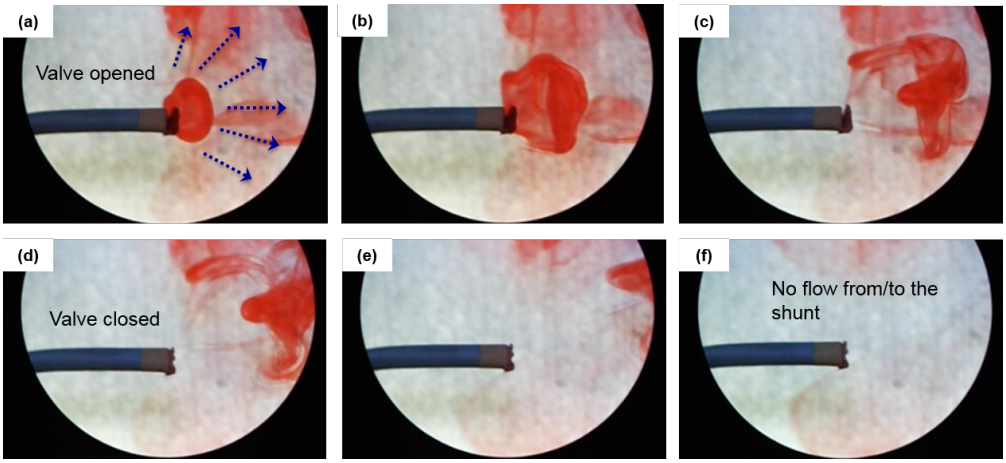

Figure 16: Flow visualization of the one-way valve functionality using food dye.

loamniotic shunt integrated with dislodgement prevention anchors and the passive one-way valve was designed and manufactured. Both 3 Fr and 4 Fr catheters served as the shunt tube and thermal shaped nitinol wires were attached on the outer tube surface to form the anchors. Finally, the PEUU membrane was attached on one end of the shunt tube as a passive one-way valve. In vitro pressure level and flow rate measurement proved the shunt functionality as the 3 Fr shunt relieved 88.3% while the 4 Fr shunt relieved 95.2% of the abnormal high pressure in fetal brain. The measurement of frictional force generated by anchors upon compression through the simulated fetal skulls compared the anchor performance of three

different designs quantitatively. The flow visualization of passive one-way valve functionality was evaluated with flow visualization. In summary, our new ventriculoamniotic shunt prototype showed superior performance of draining the excess cerebrospinal fluid from the high pressurized fetal skull, reducing the likelihood of device dislodgement during the surgery operation and preventing the reflux of amniotic fluid into the cerebral ventricles. Future work will include the in vivo functionality studies and the biocompatibility testing of the device using sheep models. And the one-way valve will be optimized to prevent thre reflux of CSF.

3.0 TFN FLOW-DIVERTER INTEGRATED WITH SENSING SYSTEM FOR CEREBRAL ANEURYSM TREATMENT

3.1 INTRODUCTION

Cerebral aneurysm is a cerebrovascular disorder caused by the local ballooning in the blood vessels that allows blood to flow into a sac outside of its normal flow path. The reported prevalence of unruptured cerebral aneurysm varies from 3.6% to 6% in the population [49] and the aneurysm represents the potential for a rupture or leak which results in hemorrhagic stroke, permanent nerve damage or death. Effective monitoring and early treatment is therefore critical to prevent further arising complications. Current treatments of cerebral aneurysm involve surgical procedure and endovascular embolization. Due to the high risk of morbidity associated with clipping [50], coiling has been adopted as a common procedure and the risks were reduced by 7.4% [51]. While coiling is less invasive, the cure rates still lag behind those of clipping, due to persistent blood flow into the aneurysm in up to 38% of patients [52].

A more recent and compelling treatment technique is the use of a flow diverter deployed inside the vessels adjacent to the aneurysm. A flow diverter effectively reduces blood flow into the aneurysm and a complete occlusion rate of 76% has been seen in the clinical outcome [53]. Complete occlusion of the aneurysm after treatment significantly reduces the risk of a rupture compared to partial occlusion and it has shown risk of re-rupture to be 1.1% [54] in the cases of a ruptured aneurysm.

A neurovascular catheter is typically used to deliver a flow diverter to the cerebral aneurysm site. However, it presents a challenge in that it can cause the flow diverter's metal film to undergo extreme radial deformation and extreme bending as it navigates the

highly tortuous vessels. In this case, the microflow sensor should be flexible and stretchable to accommodate utilization in the cerebral blood vessels.

High-quality catheter angiography is generally employed to evaluate subarachnoid hemorrhage for unruptured aneurysms. But angiography examination is qualitative and fails to disclose an aneurysm in 10 to 20 percent of cases of subarachnoid hemorrhage [50]. Another approach to monitor the aneurysm is pressure sensing. Both the direct intra-aneurysmal sac pressure measurement using tip-pressure sensors and wireless pressure sensing for endovascular aneurysm repair has been reported [55, 56, 57]. However, these sensors are not sufficiently flexible for use in intracranial endovascular procedures, which typically require a 1.7 Fr micro-delivery catheter (i.e., OD=0.56 mm). Also the recent studies have confirmed that the intra-aneurysm pressure is not significantly changed after the coil placement [58, 59, 60, 61, 62], which means the pressure sensor is not suitable for monitoring intra-aneurysm hemodynamic quiescence. Therefore, a flow sensing system needs to be developed and can be integrated with the TFN flow-diverter for cerebral aneurysm treatment monitoring.

In this work, we demonstrated the microfabricated thin film nitinol (TFN) as the porous mesh in the flow diverter can be stretched up to 500% and deformed up to 180° in bending without mechanical failures, suggesting the safe deployment of TFN covered flow diverter in a neurovascular aneurysm. The proposed stretchable microflow sensor package can be conformally integrated with a TFN covered stent to monitor the cerebral aneurysm hemodynamics quantitatively inside the blood vessels. Therefore, the efficacy and progress of the aneurysm treatment process can be evaluated by measuring the incoming flow rate into the aneurysm sac.

3.2 METHODS

The proposed TFN flow-diverter integrated with the flow sensing system consist of three components: nitinol backbone frame, micropatterned TFN as the stent graft and a microscale wireless flow sensing system. In the methods section, we described the methods for

analyzing the fluid patterns inside the cerebral aneurysm, TFN flexibility and stretchability, microflow sensor flexibility and the functionality of the proposed smart TFN flow-diverters for cerebral aneurysm treatment and monitoring.

3.2.1 Computational modeling

3.2.1.1 TFN flexibility evaluation The desired micropatterned TFN needs to withstand large deformation along with the nitinol backbone frame, therefore, we need to evaluate the flexibility of the TFN as the covering membrane for flow-diverter device. 3D computational study employs a simplified geometric model of a microstructured TFN membrane. The finite element modeling estimated the mechanical behavior of the structure upon uniaxial stretching in radial and longitudinal directions, biaxial stretching and bending. ANSYS Structural Analysis 15.0 was utilized with user-defined material properties for the TFN membrane to calculate the stress and strain fields. To reduce the computational complexity, only a small fraction of the TFN membrane structure (6 repeated patterns) was modeled.

For radial loading, the TFN structure was modeled with purely *Hex20* elements (Figure 17(A)) and two symmetric displacement loadings in radial direction were applied on two edges of the structure (Figure 17 (B)). The structure surface was constrained from out-of-plane motion to simplify the problem into 2 dimensional motion. The magnitude of the displacement loadings was gradually increased and the maximal equivalent stress as well as maximum principle strain fields were calculated to determine the potential fracture locations in the structure. Here, we defined the strain % as the displacement loading over the original distance and assumed that the fracture occurred on the location where the maximum principle strain exceeded the strain limit of the nitinol material (Figure 17 (C)). The calculation iterations were also shown in Figure 17(D).

The TFN structure was modeled with a combination of *Hex20* and *Wed15* elements in longitudinal (axial) loading analysis (Figure 18). Similarly, two symmetric displacement loadings in axial direction were applied on two edges to stretch the TFN membrane out in horizontal direction. We gradually increased the magnitude of the displacement loading and the maximal equivalent stress as well as maximum principle strain field was computed.

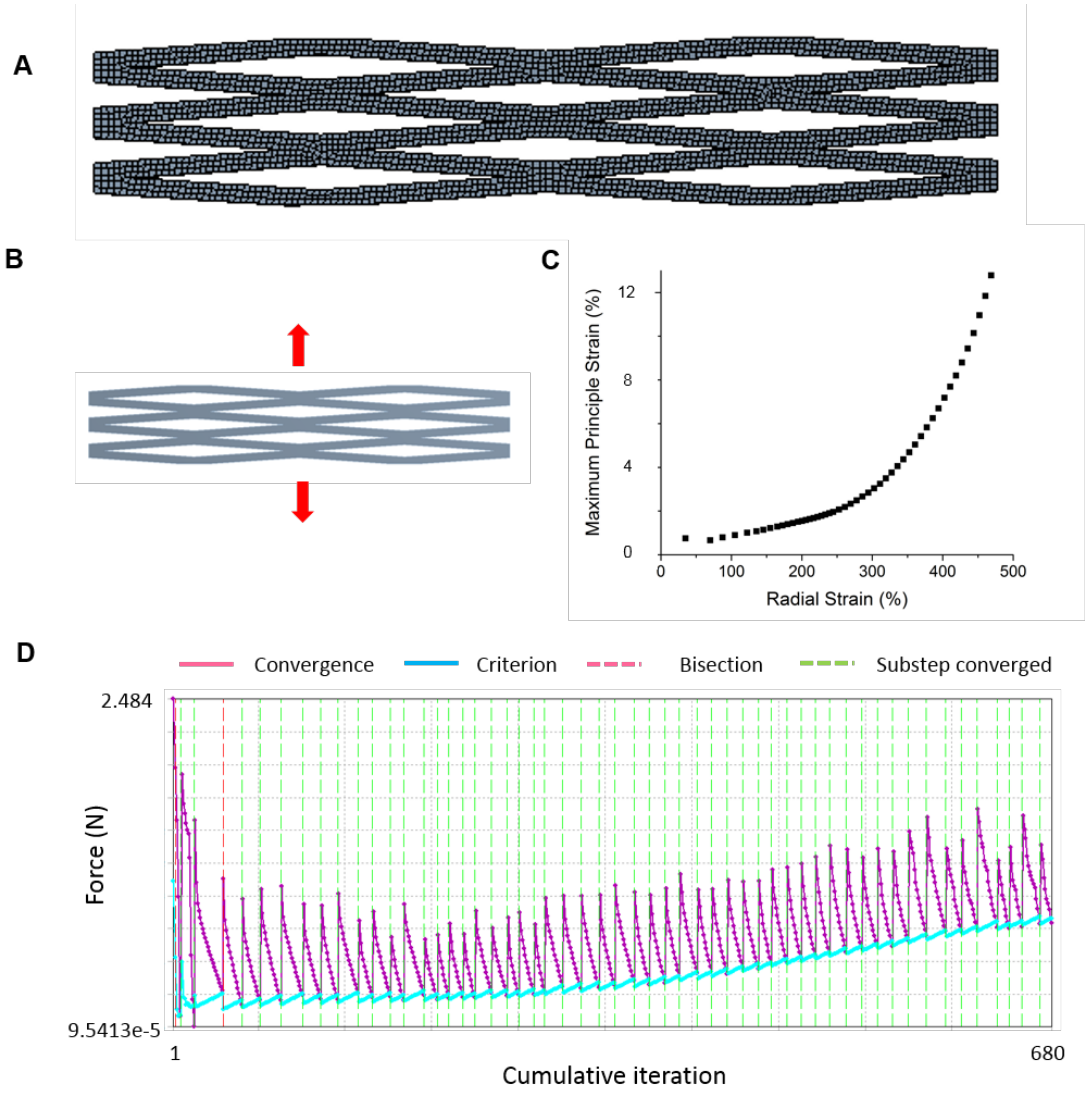

Figure 17: (A) The meshed model for TFN membrane in ANSYS Static Structural 15.0. (B) The boundary conditions in the modeling analysis. Red arrows represent the symmetric displacement loading directions (radial direction). (C) The relationship between the calculated maximum principle strain % (in y axis) and the applied strain % (in x axis). (D) The force convergence plot with Newton-Raphson method.

Figure 19 describes the details for modeling of the biaxial stretching. In first step, a 100% strain displacement was applied on two faces on the top and other two on the bot-

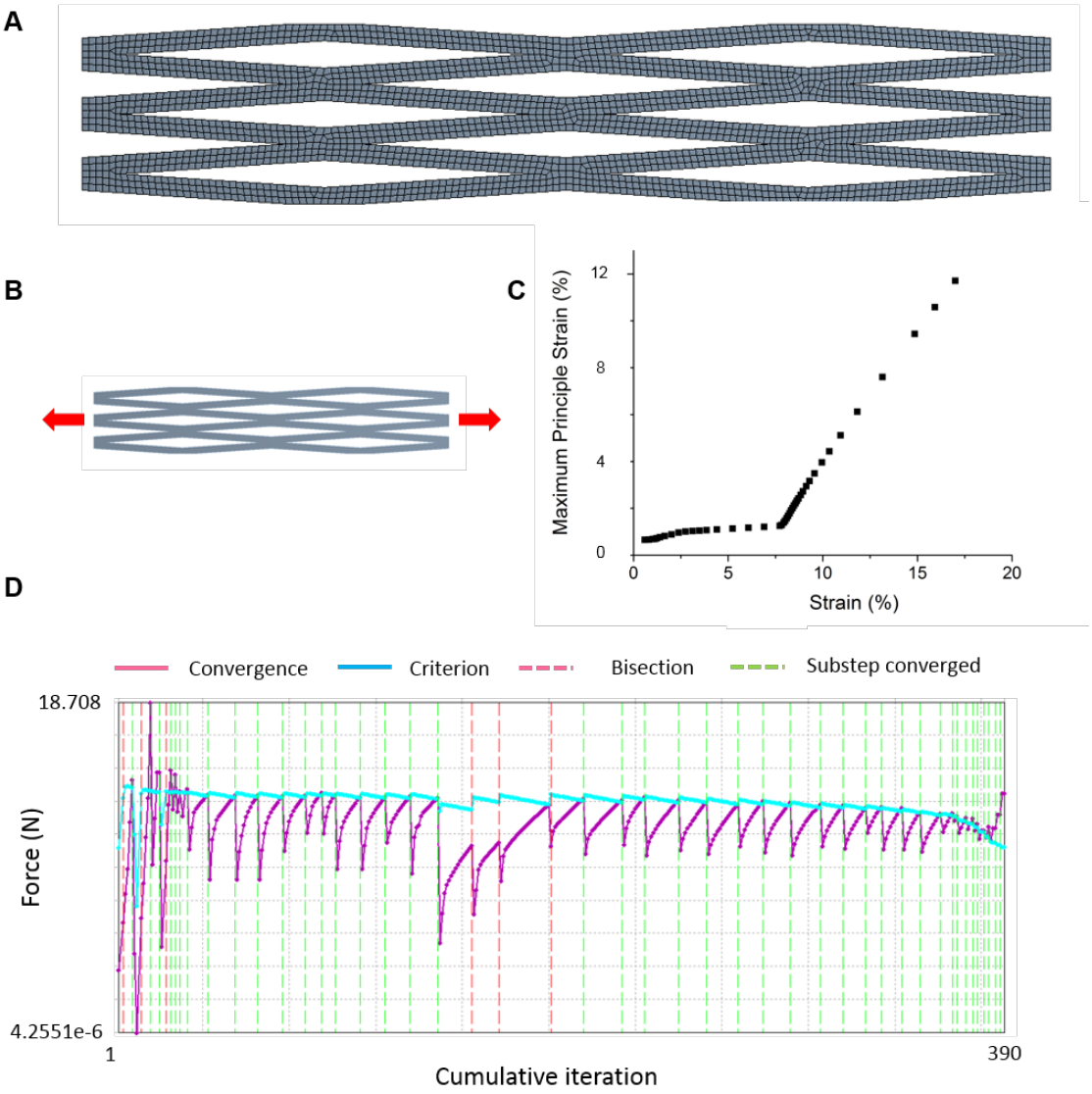

Figure 18: (A) The meshed model for TFN membrane in ANSYS Static Structural 15.0. (B) The boundary conditions in the modeling analysis. Red arrows represent the symmetric displacement loading directions (axial direction). (C) The force convergence plot with Newton-Raphson method. (D) The relationship between the calculated maximum principle strain % (in y axis) and the applied strain % (in x axis).

tom. This is the step where the TFN structure was stretched in the radial direction before being wrapped around a stent backbone. We only applied 100% strain displacement to min-

imize the buckling issues, which will increase the computation complexity [63]. This biaxial stretching experiment was to demonstrate the effects of radial strecthing on longitudinal stretching.

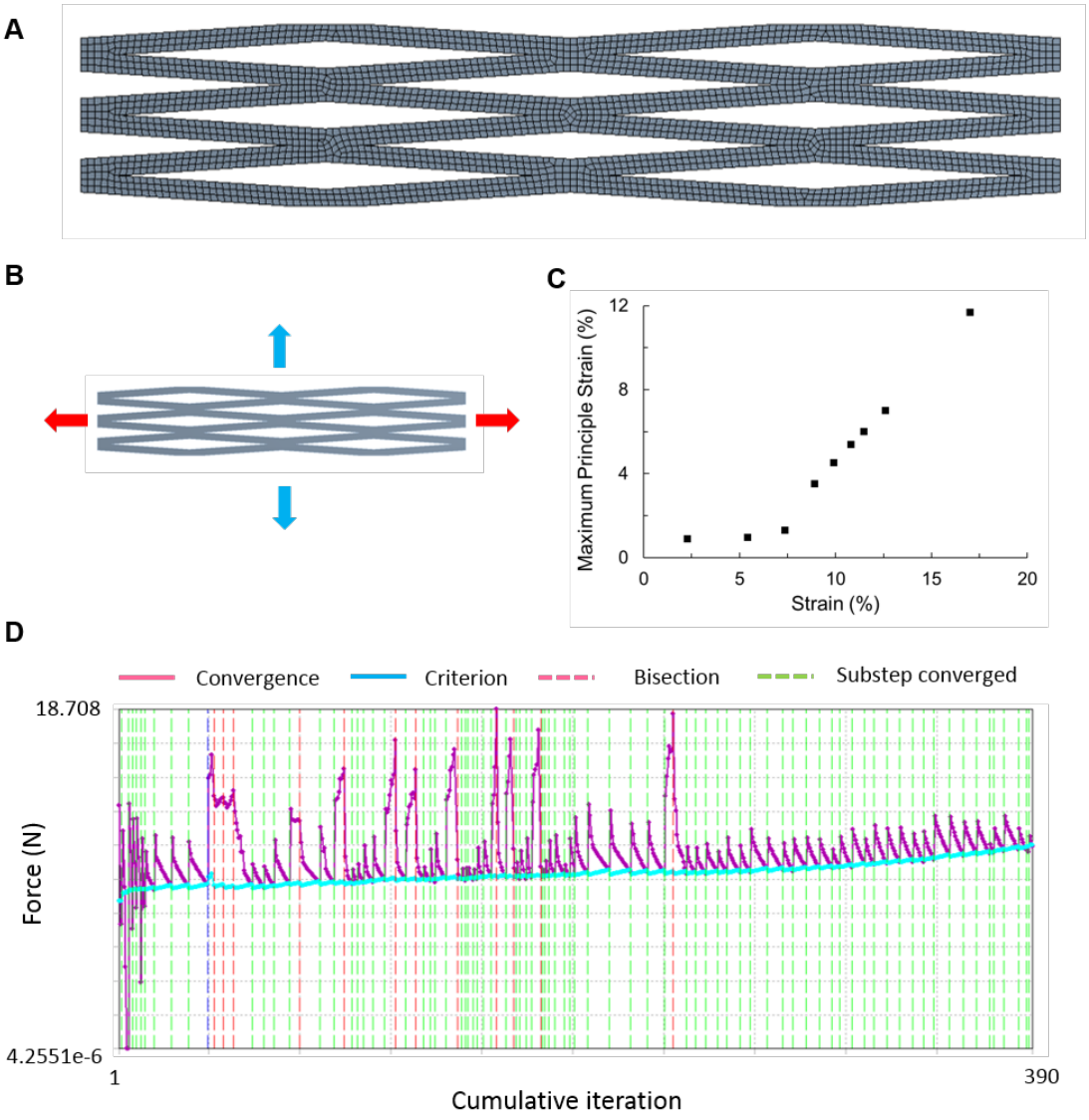

Figure 19: (A) The meshed model for TFN membrane in ANSYS Static Structural 15.0. (B) The boundary conditions in the modeling analysis. Blue arrows represent the displacement loading directions (radial) in the initial step and red arrows represent the displacement loading directions (axial) in the subsequent step. (C) The relationship between the calculated maximum principle strain % (in y axis) and the applied axial strain % (in x axis). (D) The force convergence plot with Newton-Raphson method.

Figure 20 presents the modeling results of the mechanical bending. To analyze the mechanical behaviors of the TFN structure subject to deployment in curved vessels, a three-point bending analysis was performed with a combination of *Hex20* and *Wed15* elements.

As the TFN membrane will be attached on the nitinol backbone using biocompatible glues. It is important to evaluate the glue patterns between the microporous TFN membrane and relatively rigid backbone. Figure 21 shows the details for the finite element calculation. We modeled 24 repeated patterns for TFN membrane and defined some glue positions between the TFN and stent backbone.

3.2.1.2 Sensor functionality analysis We integrated a flow sensor with the flow-diverter to monitor the hemodynamics within the cerebral aneurysm. The proposed flow sensing system is capable of detecting the incoming flow rate. The idea of a flow sensor is to adopt the parallel plate capacitor structure, i.e., a thin dielectric elastomer layer sandwiched between two metallic layers. The sensor capacitance change corresponds to the dielectric elastomer layer deformation in the flow environment to monitor fluid dynamics. For a rectangular layer of an incompressible, homogeneous elastomer that is bonded with rigid plates on both sides shown in Figure 22(a), the relationship between applied pressure P on two electrode plates and the resultant strain e can be described by [64]

$$P = \frac{EC}{2}(S^2 - S_0^2) - E\left[1 + \frac{1}{3}\left(\frac{B^2 - L^2}{B^2 + L^2}\right)^2\right]\log(1 - e) \tag{3.1}$$

where E is the Young's modulus of the elastomer, $2L$ and $2B$ are the length and width of the rectangular layer, respectively, C is a constant defined by

$$C = \frac{4}{3} + \frac{B}{L}\left(2 - \frac{11B}{10L}\right) \tag{3.2}$$

S is a geometric parameter known as shape factor and is defined by

$$S = \frac{BL}{2(L + B)t} = \frac{S_0}{1 - e} \tag{3.3}$$

where $2t$ is the resultant thickness of the layer upon compression and S_0 is the original shape factor with initial thickness $2T$ before compression. The strain can be calculated by

$$e = \frac{2T - 2t}{2T} = \frac{\Delta T}{T} \tag{3.4}$$

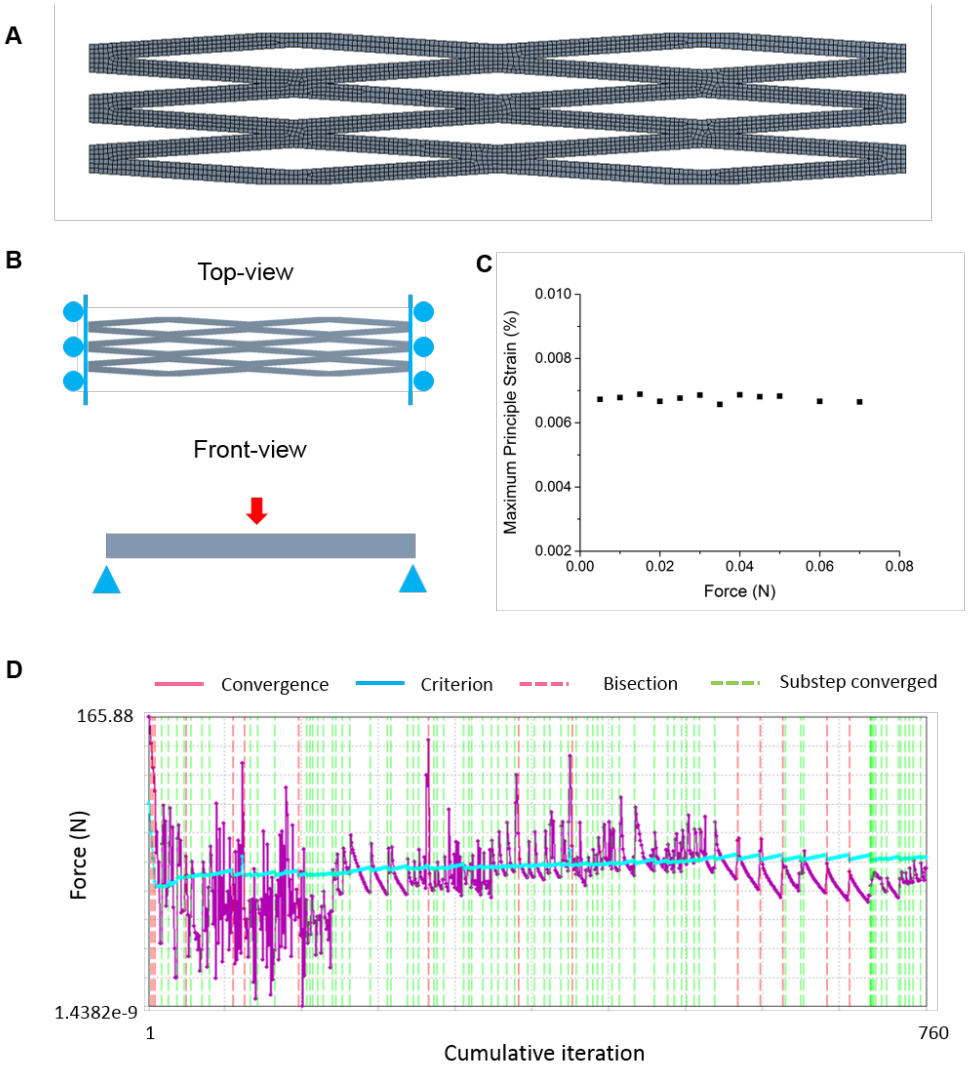

Figure 20: (A) The meshed model for TFN membrane in ANSYS Static Structural 15.0. (B) The boundary conditions in the modeling analysis. The blue rollers in the top view represent the unconstrained motion along the long axis direction. The red arrows in the front view represent the applied force direction and the blue triangles represent the constrained motion along the force direction. (C) The relationship between the calculated maximum principle strain % (in y axis) and the applied bending force (in x axis). (D) The force convergence plot with Newton-Raphson method.

A

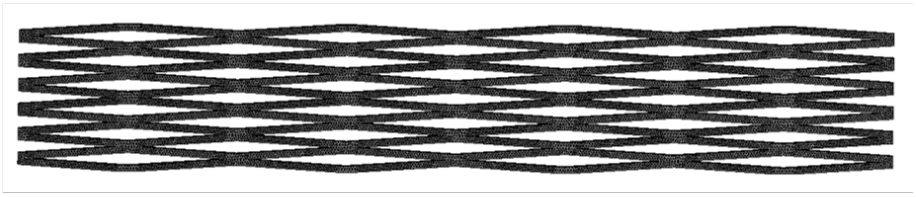

B

Mesh Metric	Element Quality
Min	0.1940
Max	0.9999
Average	0.8630

C

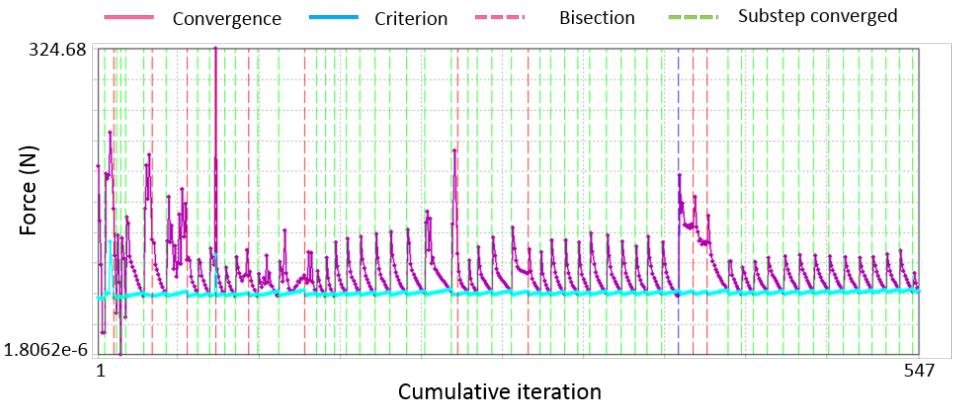

Figure 21: (A) The meshed model for TFN membrane in ANSYS Static Structural 15.0. (B) The quality of the meshed element and the value close to 1 represents high quality while the value close to 0 represents poor quality. The overall element quality is lower due to the addition of the glue junction points. (C) The plot of force convergence with Newton-Raphson method.

The dynamic pressure P generated by the liquid flow in a tube is defined as

$$P = \frac{1}{2}\rho v^2 \tag{3.5}$$

where ρ is the density of the liquid and v is the fluid velocity.

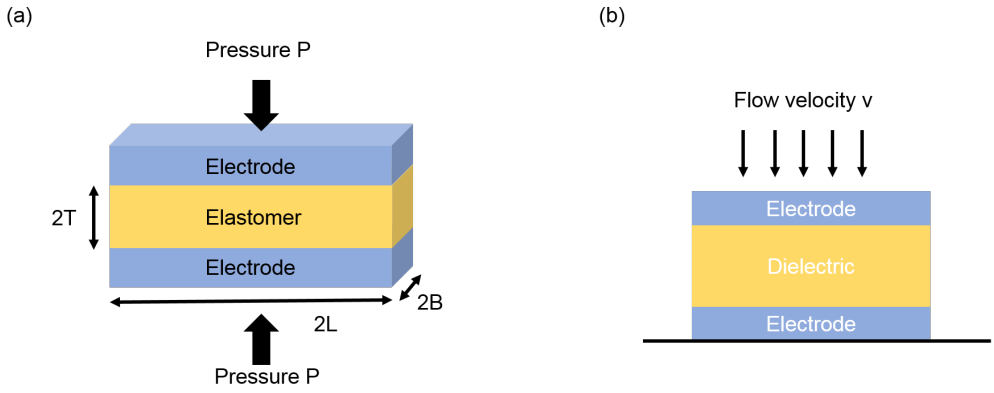

Figure 22: Concept of capacitive flow sensor. (a) Compression with applied pressure P; (b) Parallel plate capacitor model.

The theoretical equation to calculate capacitance of a parallel plate capacitor model (Figure 22(b))is given by

$$C = \frac{\varepsilon_r \varepsilon_0 A}{d} \tag{3.6}$$

where ε_0 is the permittivity of free space (8.85×10^{-12} F/m), ε_r is the relative dielectric constant of elastomer, A is the area of the electrode plate and d is the distance between these two plates, i.e., the thickness of the elastomer. Therefore, the flow velocity in the fluid environment is related to the capacitance change in the capacitive flow sensor by resultant strain upon dynamic pressure. The capacitance change can be determined by

$$\Delta C = C - C_0 = \frac{\varepsilon_0 \varepsilon_r (4BL\Delta T)}{Tt} \approx C_0 e \propto \frac{\Delta T}{T^2} \tag{3.7}$$

Here, we assumed that $\Delta T << T$ and $\Delta B, \Delta L \approx 0$ for simplicity. Thus the capacitance change can be assumed to be proportional to the elastomer thickness change over the square of the original thickness. Equation (3.7) can be used to calculate the sensor sensitivity in terms of capacitance change. This calculation provides the guideline for the capacitive flow sensor design in the later sections.

3.2.1.3 Computational fluid dynamics (CFD) modeling of the aneurysm

In order to determine the designed flow sensor locations within the cerebral aneurysm to maximize the input signals (i.e., flow rate), we assess the flow patterns in the aneurysm. A simplified aneurysm model with parent vessel was developed to calculate the flow velocity and pressure distributions with defined boundary conditions including inlet velocity and outlet pressure. Here, we simplified the saccular cerebral aneurysm into an ideal model in order to reduce the computational complexity. Another type of cerebral aneurysm (i.e., fusiform) was not considered.

3.2.1.4 Flow sensor mechanics analysis

Flexibility of the flow sensor is also a critical criteria as it will be integrated with the flow-diverter and the undergo large deformations such as collapse and deployment to the target site and navigation through the highly tortuous vessels in the brain. To study the mechanical behavior of the designed structures, we used finite element analysis (ABAQUS CAE 2016, Dassault Systems, USA) for radial stretching and bending (Figure 23). In the radial stretching, a deformable cylindrical surface was added in the model as an expander and then meshed with *SFM3D4R* elements (4-node quadrilateral surface element with reduced integration). In order to ensure the wrapped sensor was stretched radially along with the uniform expansion of the expander, the contact between the expander and sensor pattern was modeled as frictionless in the tangential direction and hard contact in the normal direction. The applied strains to the sensor was up to 500%, which was increased incrementally over time. For the bending model, a deformable cylinder was added and aligned with the sensor coaxially. It was meshed with *C3D8R* elements. A tie constraint was applied on the contact surface between outer base support and inner sensor surface to ensure. A pair of rigid cylindrical surface was added to the top and base support, then an upward displacement was applied to increase the bending angle from 0 to 180 degrees in the base. All the rigid cylindrical surfaces were meshed with *R3D4* elements (4-node 3-D bilinear rigid quadrilateral). The contact between the rigid support faces and the base support surface was modeled as frictionless in the tangential direction and hard contact in the normal direction.

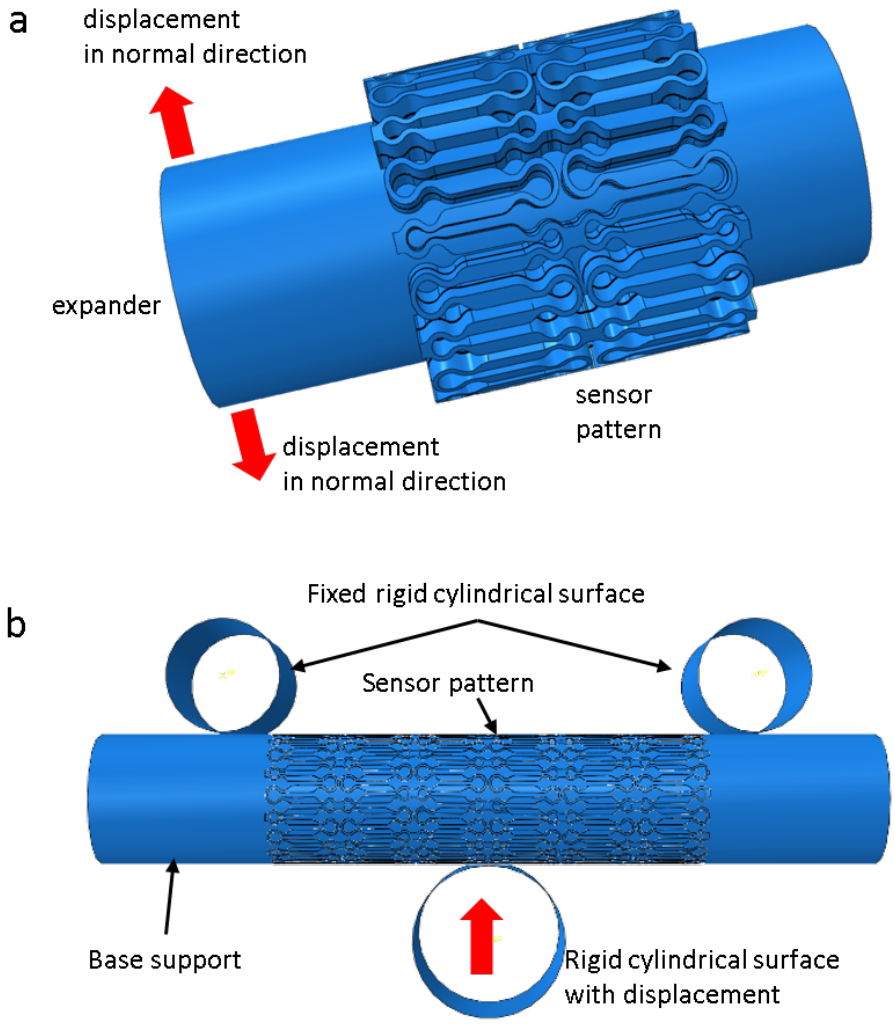

Figure 23: FEA geometric model. (a) Base setup for radial stretching simulation in which the sensor pattern (two unit cells in axial length) is wrapped circumferentially around an expandable cylinder. (b) Base setup for radial bending in which the sensor (6 unit cells in axial length) is fixed to a supporting base cylinder which undergoes bending up to 180^o by displacing the bottom rigid cylinder upwards against the two top rigid cylinders.

3.2.2 Experimental setup for TFN flexibility evaluations

3.2.2.1 Uniaxial stretching A small rectangular sample of TFN was cut and affixed to a custom-made mechanical stretcher [63, 65]. Two separate uniaxial loading tests were performed; one in the radial direction, and one in the longitudinal direction. For the radial loading, the sample was aligned vertically along the length of the stretching machine such that strain was only applied widthwise along the diamond fenestrations. For the longitudinal loading, the sample was aligned horizontally along the length of the stretching machine such that the strain was only applied lengthwise along the diamond fenestrations. The stretching machine had one fixed support block (slide) with a copper strip running down its length, the sample was glued to the copper and colloidal silver paste was applied to secure electrical conductance. The other side of the sample was affixed to an adjustable support block (slide) in the same fashion. The copper strips were connected to wires so that the electrical resistance of the sample could be measured via a digital multimeter (Model 2100, Keithley, Cleveland, OH). An initial resistance measurement was taken while the sample was at rest (0% strain) for a baseline. Resistance of the sample was recorded to document the structural integrity of the material whereas an increase of resistance would indicate structural degradation of the sample. The adjustable slide was then moved in approximately 2% increments to increase the distance between the two slides, thereby increasing the strain on the sample. The percentage of the strain was calculated by the percentage increase of distance over the original distance. The increase in resistance compared to the increase in strain was recorded and plotted for each increment until the mechanical failure of the sample. After the first fracture point on the sample occurred, the structure was investigated by scanning electron microscopy.

3.2.2.2 Biaxial stretching The samples were first placed under preloaded strains ranging from 300% to 360% along the width (in the radial direction) and then connected to two separate electrical wires. The samples were wrapped circumferentially around the wires to mimic the shape of the stent backbone. Similarly to the uniaxial sample, it was glued at every point around the wire and electrical conductivity was ensured using colloidal silver

paste. One wire was attached to the fixed slide, and the other attached to the adjustable slide. The testing then proceeded the same way as for the uniaxial sample.

3.3 RESULTS

In this section, we present the mechanics evaluation of the microstructured TFN, determination of the glue locations on a TFN flow-diverter, computational fluid dynamics calculation on the fluid patterns within cerebral aneurysm, flow sensor design and characterization as well as flow rate measurements in a porcine artery.

3.3.1 TFN structure mechanics

The diamond pore TFN structure has lateral (L) and vertical length (W) of 300 μm and 20 μm, respectively. The strut has lateral length (L_1) of 56 μm and vertical length (W_1) of 24 μm with the membrane thickness (t) of 6 μm (Figure 24(A)). In order to express the super-elasticity of the TFN, the user-defined shape memory alloy was employed as shown in Table 2. The fracture limit of the maximum principal strain for the TFN was 12% [66].

Table 2: Materials properties of the TFN membrane [67]

Parameters	Definition	Value
Youngs Modulus	Elastic modulus of the material	60 GPa
Poissons ratio	Ratio of transverse contraction to longitudinal extension	0.3
Sigma SAS	Starting stress value for the forward phase transformation	52000 psi
Sigma FAS	Final stress value for the forward phase transformation	60000 psi
Sigma SSA	Starting stress value for the reverse phase transformation	30000 psi
Sigma FSA	Final stress value for the reverse phase transformation	20000 psi
Epsilon	Maximum residual strain	0.07
Alpha	Material response ratio between tension and compression	0

Figure 24(B) presents the computational and experimental results when the structure is stretched up to 500% in the radial direction by a mechanical stretcher. Both the finite element modeling and experimental results suggest that TFN has a negligible effect under uniaxial stretching in the radial direction, which was verified by a highly accurate, electrical resistance measurement with the hysteresis (relative resistance change: $< 0.5\%$). The electrical resistance is related to mechanical properties and integrity of the overall structure. The initial electrical resistance shows variations due to the sample volume and electrical contact points difference. The calculated maximum principal strain of the structure is 11.5% below than the fracture limit and no fracture was observed during the experiment, which was confirmed by the measured electrical resistance in Figure 24(C). Overall, our result proves that the TFN can be stretched in the radial direction more than 500% and thus can be deployed in a blood vessel safely.

Figure 24(D) shows the maximum application strain of 17% where it reaches fracture limit in longitudinal (axial) direction in the computational study. The experimental results by optical microscope and electrical resistance measurement also agree with the modeling results. The relative resistance measurement upon the strain change (Fig. 24(E)) verifies the mechanical fracture at $\sim$17%. Three sets of tests demonstrate the mechanical response of the membrane according to the applied strains are consistent with mild increase up to $\sim$12% and steep increase until completely fractured . Over the transition point, the TFN structure seems to experience a localized necking and fracture. Experimental variations of the alignment and integration of the TFN on the mechanical stretcher caused the difference of the slope and resistance values in multiple tests.

The biaxial mechanical study (Figure 24(F)(G)) supports the uniaxial mechanical behaviors of the TFN, shown in Figure 24(D). The testing membrane was pre-stretched from 300% to 360% in the radial direction and an additional strain in the axial direction was applied to the structure with the increment of 2%. As long as the pre-loading was within the radial strain limit of the TFN ($\sim$500%), the amount of pre-loading did not directly affect to the amount of variations in axial stretching. Overall results show a great agreement with those from the uniaxial study, meaning that the pre-loading in the radial direction is negligible as expected and the mechanical failure is governed by the axial stretching. This experimen-

tal study reveals the structural safety of the TFN considering the direct integration with a conventional backbone stent to form a cylindrical flow-diverter.

In addition, a series of the mechanical bending tests was conducted to estimate the membrane integrity when the TFN is deployed in targeted, curved arteries (Figure 24(H),(I)). The electrical resistance of the structure was measured when the curvature changed from 0 to 180 degrees. Both computational and experimental results show that multi-modal bending does not cause any noticeable mechanical burdens on the structure. The calculated maximum principal strain value in the modeling is less than 1% and the electrical resistance varies less than 0.2% based on the repeated mechanical tests. The results present that the extremely compliant TFN is capable of undergoing bending in the deployment and navigating through the highly tortuous nature of neurovascular veins.

3.3.2 Determination of the junctions for a TFN flow-diverter

Figure 25 summarizes the evaluation of attachment patterns between a TFN and stent backbone, based on the values of maximal equivalent stress and maximum principle strain. A flow-diverter includes a TFN membrane and a stent backbone with several attachment locations (Figure 25(a)). When deployed in the curved arteries, the hyper-elastic TFN conforms to the geometry of the blood vessels. In this computational study, we modeled a TFN (24 repeated diamond patterns) with several attachment junctions (Figure 25(b)). The simulation model includes meshes with 303, 260 nodes and 157, 436 elements and shows a high quality of the meshed elements. The TFN membrane has 200% pre-strains in the radial direction. The faces of attachment locations are constrained in the longitudinal direction to simulate the attachment of the TFN on the stent backbone. We compared three representative patterns of glue joints to determine the optimal pattern when the same loading was applied on the vertical direction to stretch the TFN structures (Figure 25(c)). Case 1 considers six glue joints in the vertical direction on both sides, which results in 2.6% of the maximum principal strain (MPS) and 1.6 GPa of the maximum equivalent stress (MES). Diagonal (case 2) and uneven (case 3) glue points show 4.5% (MPS), 2.7 GPa (MES) and 4.4% (MPS), 2.6 GPa (MES), respectively. As summarized in the table (Figure 25(d)), case

1 shows the lowest MPS and MES compared to other cases. Thus, we choose the evenly distributed, symmetric glue patterns that provides the highest structural safety upon the given loading condition.

In addition to the determined glue pattern, we conducted another set of computational study to find out the effect of the number of glue points to the structure. Figure 26 shows five different cases with varying glue points from 10 to 2. To analyze the mechanical behavior, the same loading was applied to the structures vertically and the MPS and MES were compared. Figure 26(a)-(e) show the computational results with the applied loading and Figure 26(f) summarizes the values of MPS and MES for five cases. The testing result suggests to minimize the number of glue points for better structural safety upon the mechanical stretching; two symmetrical glue points show only 1.7% of MPS and 0.9 GPa of MES.

3.3.3 Computational fluid dynamics (CFD) analysis in cerebral aneurysm

It can be observed from refaneurysm cfd that the flow in the aneurysm sac region adopts the counterclockwise fashion, which means that the incoming flow will enter the sac at the distal end and exit at the proximal end. Also Figure 27(c) demonstrates that the fluid velocity has the maximum (in the range of 0.102-0.134 m/s) at the aneurysm neck and minimum (in the range of 0.0029-0.0036 m/s) at the dome. These results match well with previous experimental results using particle image velocimetry systems [69]. Figure 27(d) and (e) also show the static and dynamic pressure contour plots in the symmetry plane. The static pressure in the sac region is similar to the parent vessel while the dynamic pressure is significantly reduced from aneurysm sac to the dome due to the velocity drop. It confirms with the hypothesis that static pressure is approximately uniformly distributed among the sac region while the dynamic pressure or flow velocity should be monitored to assess hemodynamic quiescence within the aneurysm sac. It also suggests that the ideal location for the microflow sensor placement is near aneurysm neck to achieve the highest signals.

3.3.4 Flow sensor flexibility characterization

Finite element analysis (FEA; ABAQUS CAE 2016, Dassault Systems, USA) was used to design a highly compliant structure for a flow sensor. Considering the estimated deformation during sensor integration, catheter insertion, and deployment, we focused on ultra-stretchable and bendable building blocks. The computational model (Figure 23a) includes an array of serpentine-like mesh patterns, configured in a ring-type structure for assembly with a TFN and stent backbone. The model structure with seven sensor layers (bottom elastomer, PI, metal, dielectric, metal, PI, and top elastomer) were meshed with *C3D8R* elements (8-node linear brick, reduced integration, and hourglass control) and the mesh quality was monitored during calculation. In addition, an explicit dynamic method was employed to model the highly nonlinear deformation under radial loading and bending (details appear in Figure 23).

3.4 CONCLUSIONS

A flow-diverter can be deployed inside the targeted vessels for aneurysm treatment by occluding the incoming blood flows into the aneurysm sac. However, the hemodynamics inside the aneurysm sac needs to be monitored in real time as the blood flows can re-enter the aneurysm sac to cause the rupture. As the flow-diverter backbone is covered with a porous TFN membrane, the flexibility of the TFN was evaluated using 3D computational study. Different boundary conditions such as uniaxial, radial, biaxial and bending were applied on a simplified TFN structure to examine the structure integrity. Both the computational study and experimental results demonstrate that the TFN structure can undergo 500% radial stretching and 17% longitudinal stretching without failure. Also TFN can survive extreme bending up to 180° during the navigation in highly tortuous blood vessels. A computational study was also employed to determine the optimal junctions on the TFN flow-diverter. The results show that the number of glue points needs to be minimized for better structural safety. The optimal flow sensor location was determined by a CFD calculations with an

idealized aneurysm model. Then the flow sensor flexibility was modeled using Abaqus and it shows 500% stretching in uniaxial and radial directions without failure. All the results demonstrate the feasibility of a TFN flow-diverter integrated with a microflow sensing system for aneurysm treatment.

The collective results for the flow sensor also show that an ultra-stretchable, implantable flow-diverter system offers highly sensitive quantification of flow dynamics inside a blood vessel. This flow sensing package allows an alternative post-treatment monitoring of the intra-aneurysmal hemodynamics. There types of sensor materials including Au for a prolonged implantation, NiTi for a shape memory configuration and Mg as the transient use were explored to demonstrate the system versatility. Both the computational and experimental studies on the sensor flexibility demonstrated the system capability in a catheter-assisted deployment in neurovascular vessels.The future work will include the development of a miniaturized, wireless communication system based on the passive inductive coupling.

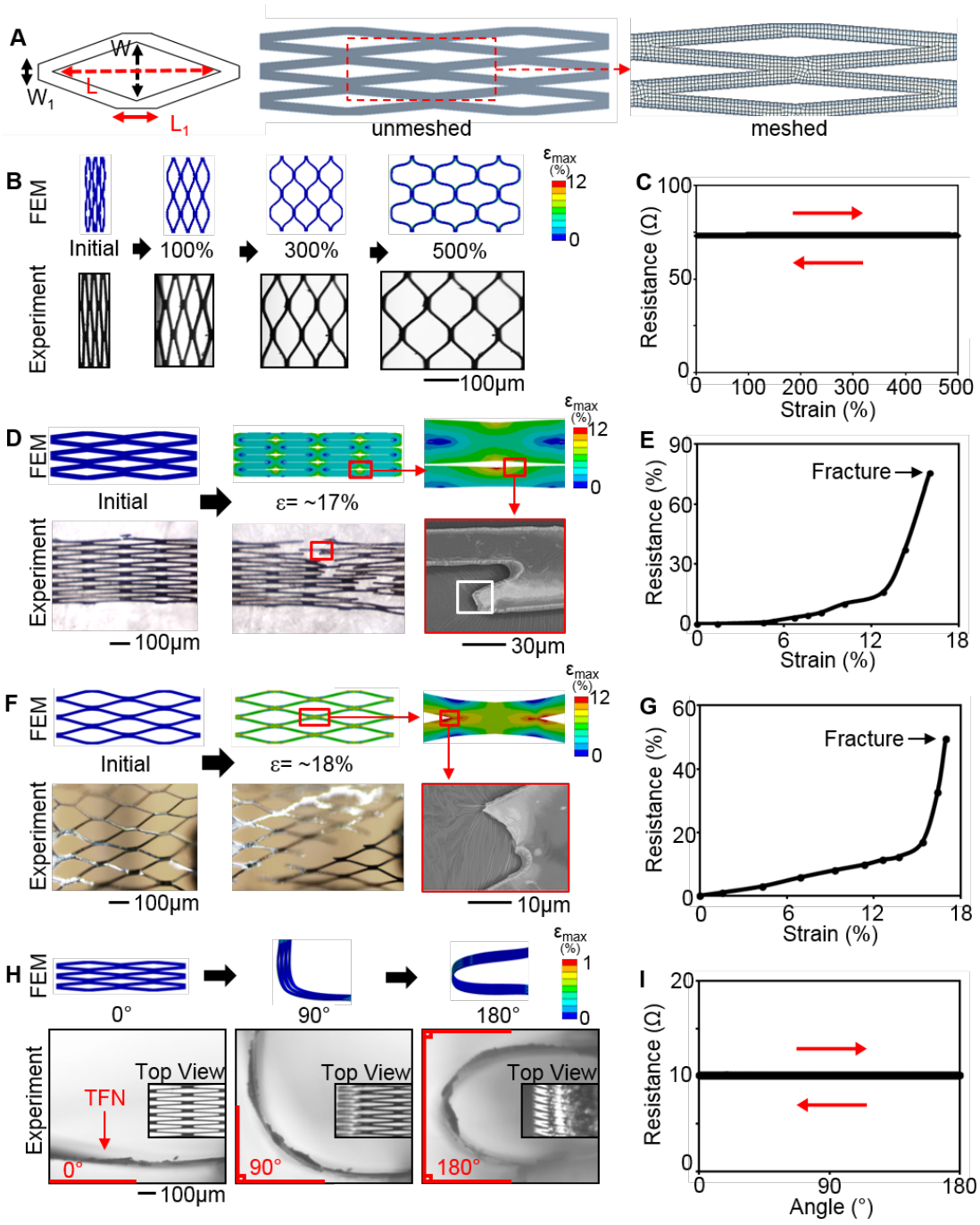

Figure 24: Mechanical behavior of a TFN. (A) A geometric model of a TFN with dimensions and meshed structure; lateral length: $L = 300$ μm and $L_1 = 56$ μm and vertical length: $W = 20$ μm and $W_1 = 24$ μm. (B,D,F,H) Comparison between the FEM results and optical and scanning electron microscopic images of a TFN for radial stretching (B), axial stretching (D), biaxial stretching (F), and bending (H). (C,E,G,I) Plot of electrical resistances of a TFN according to the applied strains (C,E,G) and the bending curvature (I). [68]

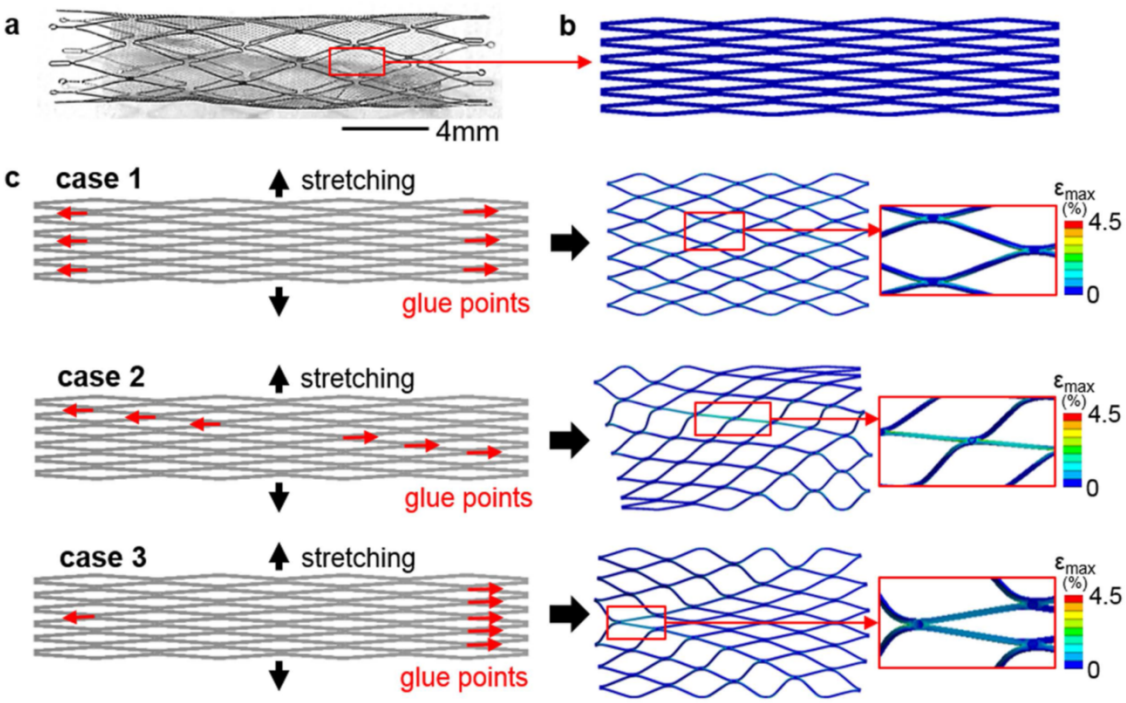

d

	Case 1	Case 2	Case 3
Maximum principal strain (%)	2.6	4.5	4.4
Maximum equivalent stress (GPa)	1.6	2.7	2.6

Figure 25: Determination of the optimal junctions according to the attachment patterns. (a) Optimal microscopic image of a TFN flow-diverter. (b) A TFN geometry for the FEM study. (c) Three representative patterns of glue points (six locations) with the vertical stretching for integration with a backbone stent. (d) Table summarizing the maximum principal strain and maximum equivalent stress; case 1 shows the lowest values in both criteria.

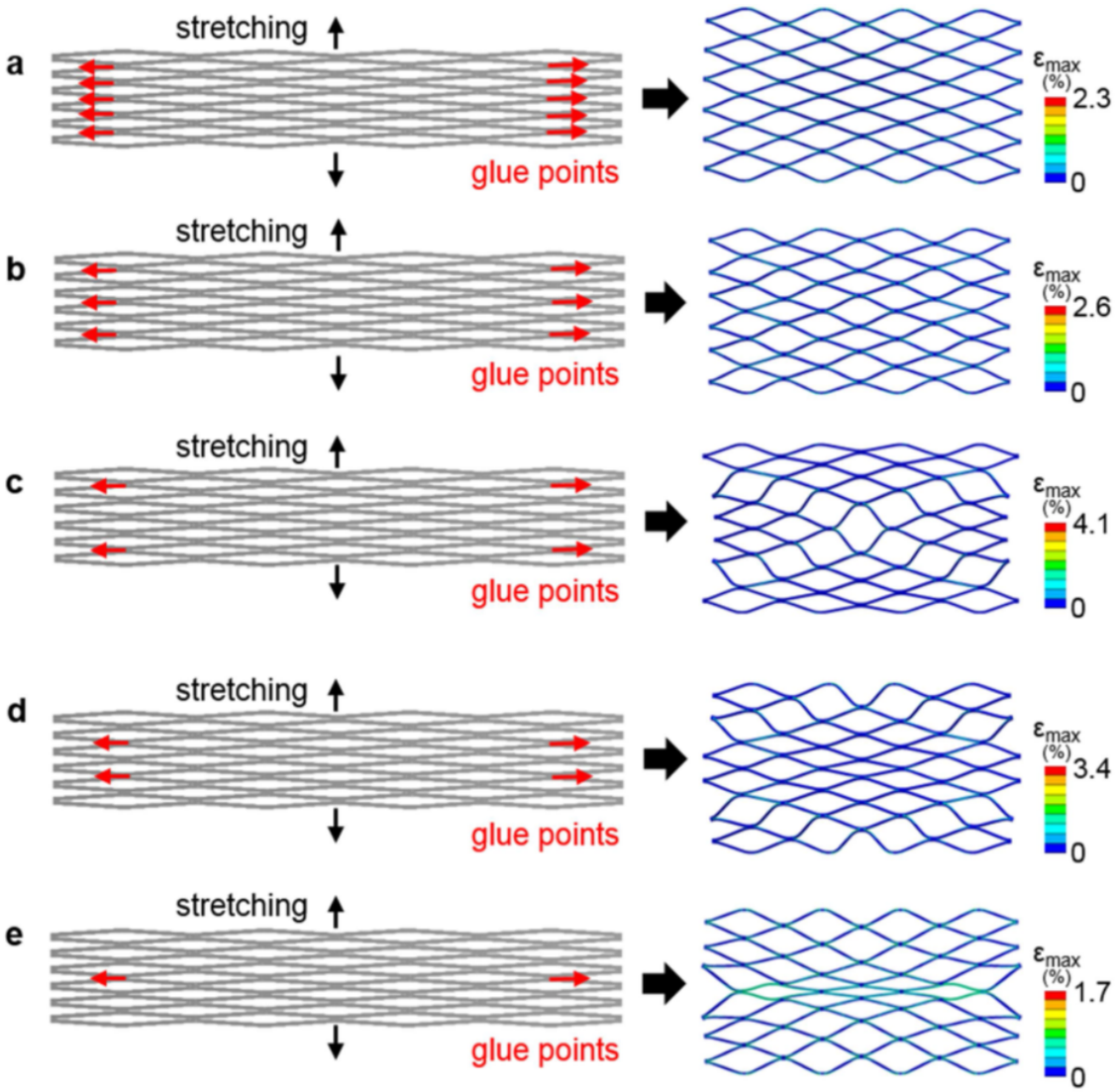

f

	Case (a)	Case (b)	Case (c)	Case (d)	Case (e)
M.P.S. (%)	2.3	2.6	4.1	3.4	1.7
M.E.S. (GPa)	1.4	1.6	2.5	2.1	0.9

Figure 26: Determination of the optimal junctions according to the number of glue points. (ae) Five different cases with different numbers of glue locations and their FEM results that show the deformation patterns and the maximum principal strains. (f) Table summarizing the maximum principal strain (MPS) and maximum equivalent stress (MES); case (e) shows the lowest MPS and MES.

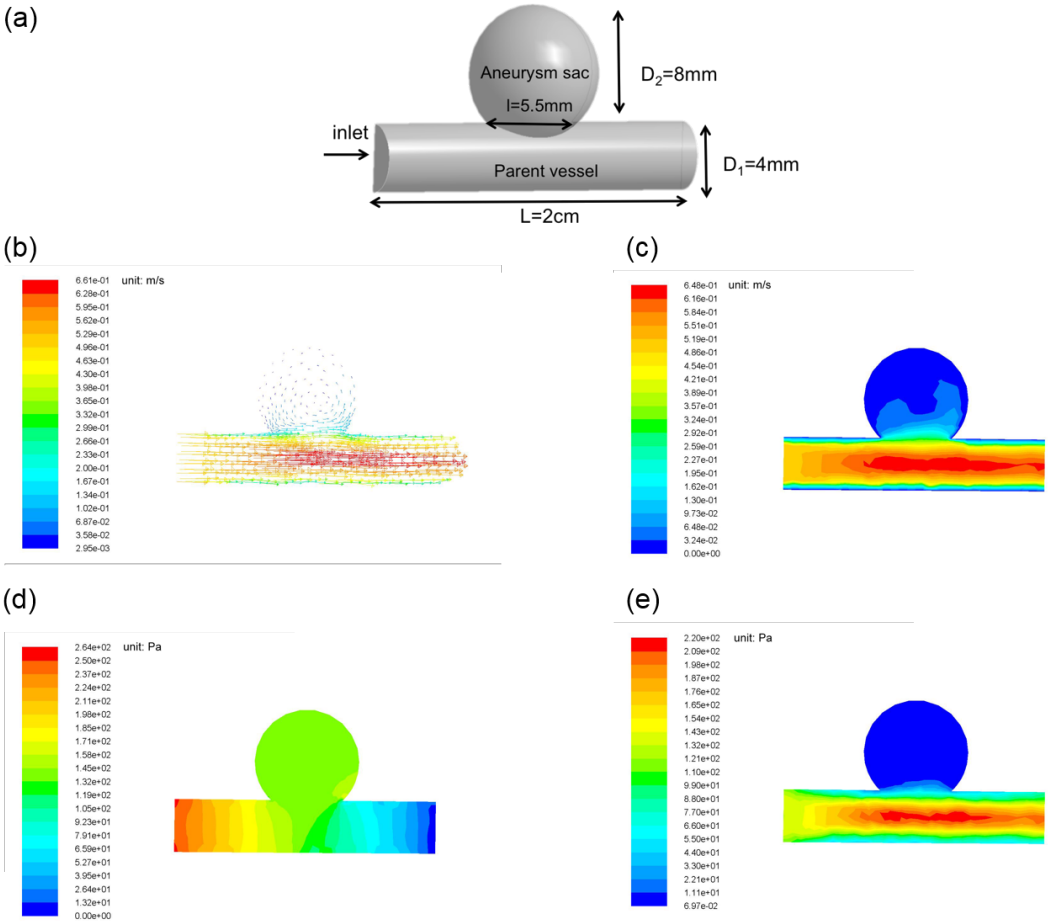

Figure 27: CFD results for the blood flow profiles with an aneurysm sac. (a) Geometry model. (b) Velocity vector on the symmetry plane in the aneurysm model. (c) Velocity contour on the symmetry plane in the aneurysm model. (d) Static pressure contour on the symmetry plane in the aneurysm model. (e) Dynamic pressure contour on the symmetry plane in the aneurysm model.

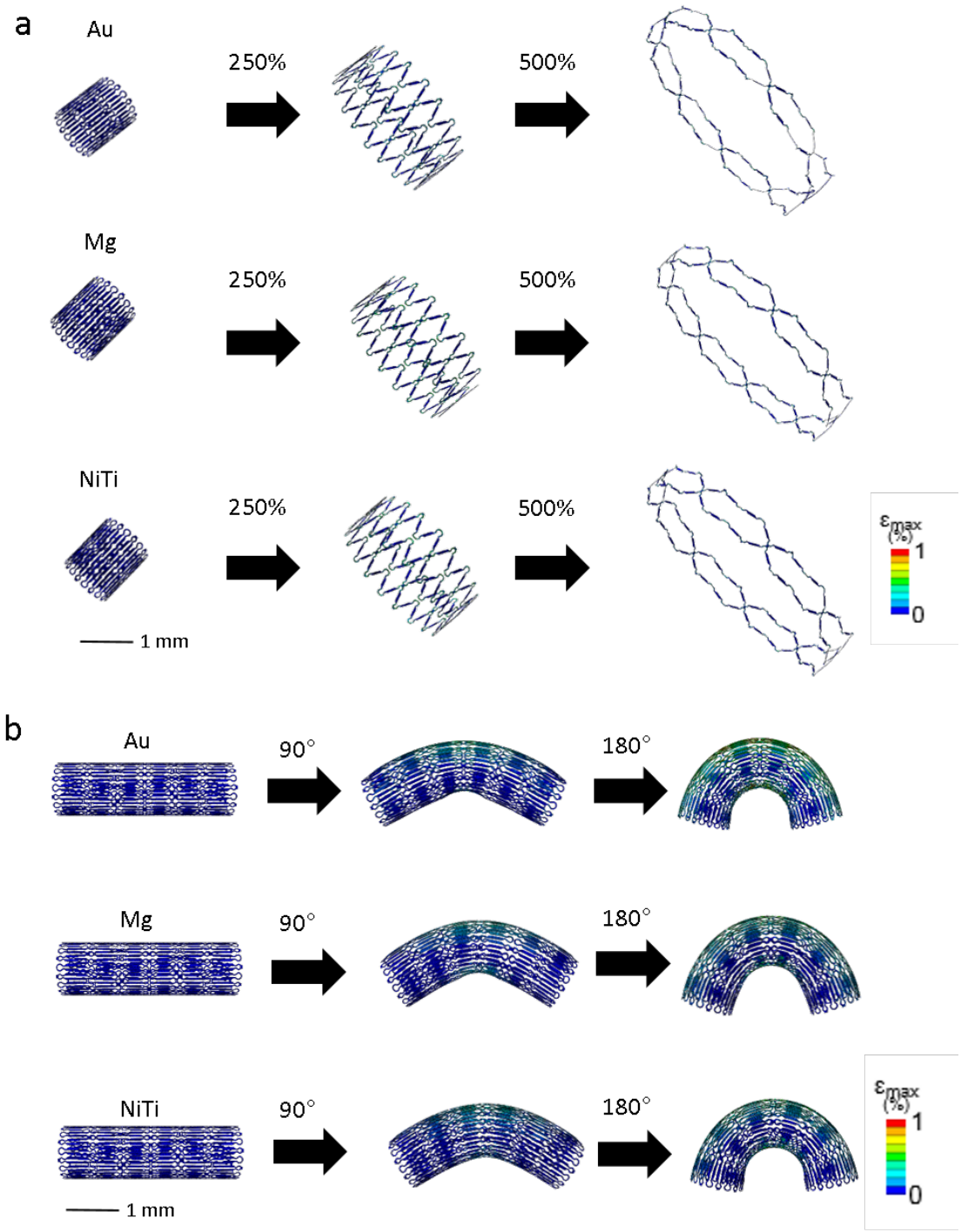

Figure 28: (a) Radial stretching (up to 500%) of Au, Mg, and NiTi sensors. (b) Bending up to 180° of Au, Mg, and NiTi sensors. Both results show negligible values from the maximum principal strains.

Table 3: Materials properties and calculated maximum principal strain (MPS) values. The fracture limits of Au, Mg, and NiTi are 5% [74], 10% [75], and 12% [66], respectively.

Materials	Young's modulus (GPa)	Poisson's ratio	MPS from 180° bending (%)	MPS from 500% radial stretching (%)
NiTi [70]	6	0.33	0.91	0.84
Mg [71]	4.5	0.35	0.91	0.89
Au [72]	79	0.4	0.98	0.94
Ecoflex [73]	0.069	0.49		
PI [68]	2.5	0.34		

4.0 COMPARTMENTALIZED STENT GRAFT TO ISOLATE THE PERFUSION OF THE ABDOMINAL ORGANS

4.1 INTRODUCTION

One of the major obstacles facing organ transplantation has been the shortage of donor organs. Despite over 120,000 patients in United States awaiting for organ transplant [76], only 1 in 4 will actually receive one, leaving the remaining patients with the immense burden of organ failure. Donation after brain death (DBD) or living donors have been considered as the preferred source of donor organs and organ recovery is done under ideal conditions to preserve organ function. As the combined number of DBD and living donors has plateaued [77], the current organ shortage cannot be resolved within these donor groups and other donor sources have been used to expand the organ donation pool.

Recent growth among donation after cardiac death (DCD) has represented a unique option to significantly expand the organ donation pool [78, 79]. DCD donors include patients with non-survivable injuries and cardiopulmonary life support is discontinued after family consent for donation. The details of DCD donors are unique from other donor sources and require that the consented donor first expire from a natural cardiac death after removal from life support. It is ethically mandatory that nothing be done to expedite the natural death of the donor and that organ recovery cannot proceed until after cardiac death. During this interval blood pressure and oxygenation fall and is known as the agonal phase. When the agonal phase exceeds 30-40 minutes, the organs are frequently discarded. In fact, despite the increase in potential DCD donors over the past decade, the number of organs recovered from DCD was only half of that observed in DBD donors [80]. Among those that are used, there is a high rate of complications [81, 82, 83, 84, 85, 86].

Ultimately the ability to increase the number of healthy donor organs is directly related to the ability to maintain organ perfusion while the donors own blood pressure is low and the blood is poorly oxygenated. The dilemma becomes how to maintain perfusion of the abdominal organs without increasing cardiac stress and without surgery, in keeping with ethical considerations. While several approaches have been described to deliver oxygen to the organs [87, 88, 89, 90], these methods all alter the course of cardiac death they are ethically prohibited before cardiac death. Since significant injury has already occurred by the time of cardiac arrest, these post-mortem approaches have not impacted the outcome of DCD organ donation.

Modern vascular therapies are increasingly delivered using catheter based techniques. Aortic stent grafts, for instance, are used to remodel blood flow of the aorta during aneurysm repair, but as a simple linear conduit, these offer no utility for improving DCD organ recovery. We reasoned that the large size of the aorta and vena cava (large vein) would allow for a stent with two compartments. A centre lumen would be similar to a traditional stent, while the outer chamber would circulate oxygenated blood separate from the systemic circulation. In this way, the oxygenated perfusion of the abdominal organs is insulated from the unstable environment of the agonal donor.

In this study, we have demonstrated proof of concept results for a dual chambered stent that isolates the perfusion of the abdominal organs from the circulation of the dying donor. As proof of concept, we used commercially available iliac limbs and covered stents to create a prototype dual chambered stent. As one of the key goals of this study, it was important to demonstrate that the narrowing of the centre lumen to 50% of normal would not significantly increase back pressure that would precipitate premature cardiac death.

A schematic illustrates the inadequate perfusion abdominal organs including liver, pancreas, bowels and kidneys during the agonal phase (Figure 29a). By contrast, with implantation of a compartmentalized organ perfusion stent, the abdominal organs are continuously perfused from an external chamber with blood that is oxygenated externally while the centre lumen of the stent continues to carry blood flow from the agonal donor to the rest of the body (Figure 29b). As a result, this feature will improve organ perfusion prior to withdrawal of life support, yet would not commit the patient to organ donation until the time of car-

diac death. The functionality of our prototype device was evaluated by measuring the flow fields in localized regions using a computational fluid dynamics (CFD) investigation, as well as by an *in vitro* measurement of local pressure alterations. In addition, we assessed the collapsibility and deployment of our device both *in vitro* bench-top and *in vivo* swine tests.

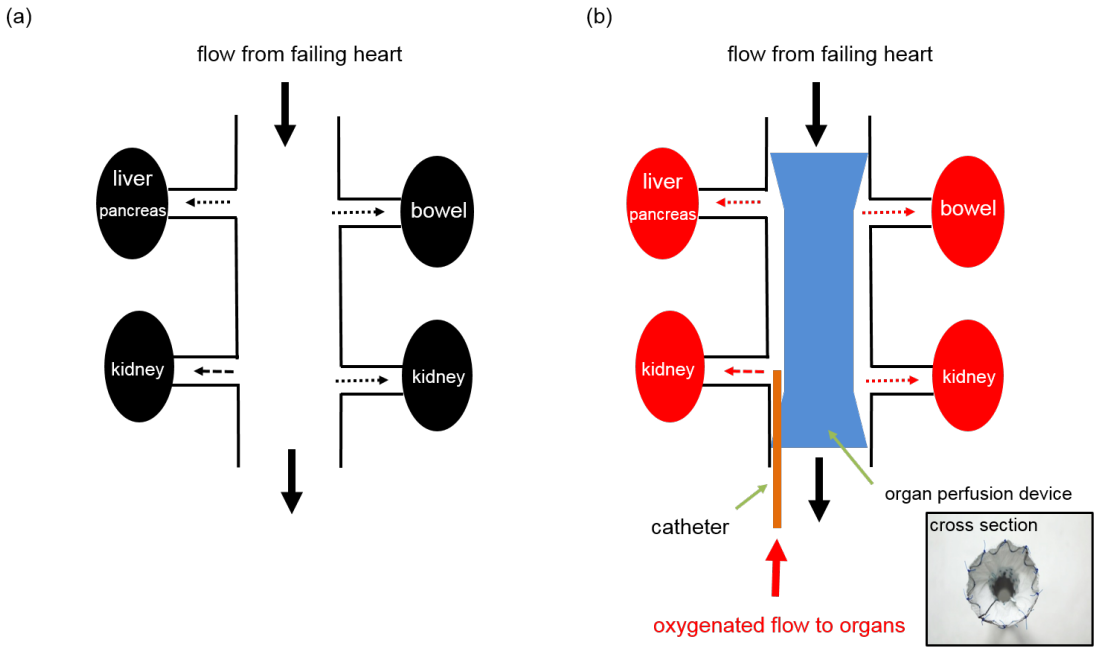

Figure 29: (a) Irreversible injury of the abdominal organs as a result of low blood flow from the failing heart. (b) The dual compartmentalised stent graft isolates the abdominal organs with oxygenated flow perfusion while the natural cardiac death process is uninterrupted. Device cross-section is shown in inset box.

4.2 MATERIALS AND METHODS

4.2.1 Creation of Organ Perfusion Stent (OPS)

Organ Perfusion Stent (OPS) for both the aorta (primary artery of the body) and vena cava (primary vein) were fabricated using commercially available stent grafts in this study. For the arterial OPS, two 12 mm diameter Dacron polyester iliac limbs seal zones (Cook, Bloom-

ington, IN) were sutured with 5.0 - 8.0 nylon sutured to both ends of the 6 mm diameter self-expanding stent graft (Viabahn stent, Gore, Flagstaff, AZ) under stereomicroscopy at 2.5 - 4.5 X magnification (SZ61, Olympus America, PA). Polytetrafluoroethylene (PTFE) sealant tape (3M, St. Paul, MN) was used to reinforce suture lines. For the venous OPS, two iliac stent grafts with a 12 mm center lumen and a tapered 23 mm seal zone (Cook, Bloomington, IN) were sewn end to end with the 12 mm ends juxtaposed.

The total length of these two devices was 13 cm. Once both arterial and venous OPS have been fabricated, an 80 cm long 10 Fr sheath (#G13033, Cook, Bloomington, IN) was integrated into the device through a hole in the proximal flare of one end of the devices. These sheaths would provide perfusion of the arterial or drainage of the venous external compartments, respectively. The 10 Fr sheath was tightly affixed to the OPS with a 5.0 size nylon suture and medical grade cyanoacrylate glue (MG30, ASI, Frankfort, IL). The distal end of the 10 Fr sheath was located 2 cm below the distal flare area to ensure the sufficient blood flow from the sheath. An additional superelastic nitinol mesh cage was manufactured using superelastic thin wires (0.012" diameter wire, NDC, Inc., CA) via a high precision mechanical bending and joining method, then subsequently added to the distal end of the 10 Fr sheath in order to prevent dynamic compression of the flow lumen. Both arterial and venous OPS prototypes were collapsed using a stent crimper (RMC, Blockwise Engineering LLC, AZ) after applying nitrogen gas (i.e., phase change to Martensite, malleable state) and decreasing the temperature. The stents were deployed via an 18 Fr and 22 Fr sheaths (Gore, Flagstaff, AZ). The prototype OPS is described in Section 4.3.1.

4.2.2 *In vitro* testing configurations

It is important to study how much the deployed stent affects the physiological hydrodynamic condition. Among many, the pressure drop created by deployment of the stent is one of the most important parameters because it directly impacts the work required of the heart. We performed *in vitro* pressure measurements as illustrated in Figure 30(a). It consisted of two separate loops: the main flow loop mimics the normal flow from the heart in the centre lumen, while the side branch loop simulates the oxygenated blood flow to the external chamber of

the stent. Figure 30(b) demonstrates the completed testing circuit based on the schematic. A centrifugal pump (Biomedicus, Medtronic, Minneapolis, MN) was used to simulate cardiac flow within the silicone tube while the peristaltic pump (FH100, Thermo Fisher Scientific, Pittsburgh, PA) was to perfuse the external chamber. A flow meter (FLR1009-D, Omega Engineering Inc, Stamford, CT) was placed adjacent to the outlet of the centrifugal pump to monitor the corresponding flow rate inside the main flow loop. A differential pressure sensor (Digi-Key Corporation, MN) with the range of ±500 Pa was connected to the pressure taps between the inlet and outlet of our organ perfusion device to measure the pressure variance across the device in the main flow. A DC power supply (GPS-4303, INSTEK America Corp., Montclair, CA) provided a 5 V voltage to the pressure sensor and an output voltage in the range of 0-5 V was measured and then converted to the pressure difference using a linear calibration curve.

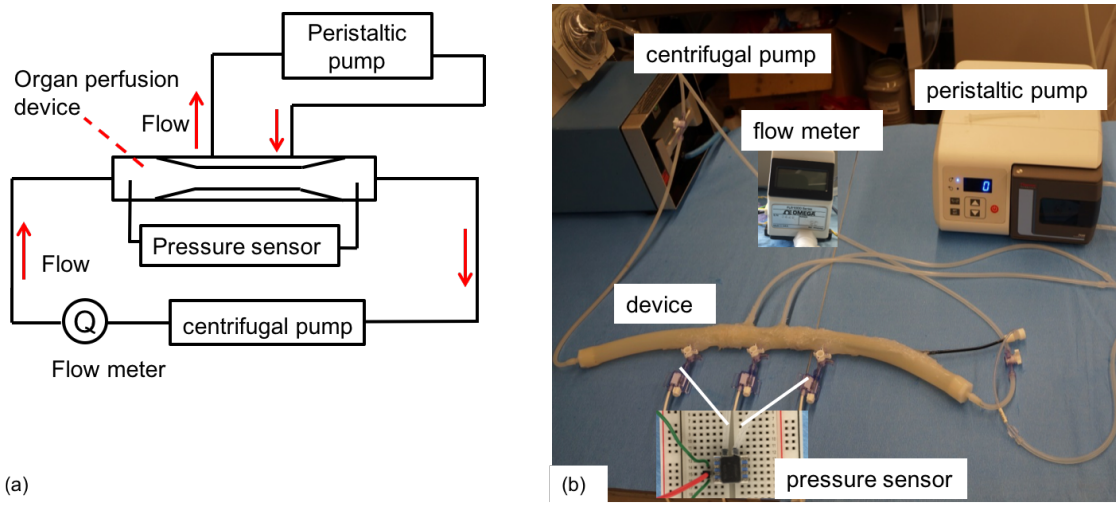

Figure 30: (a) Schematic diagram of the *in vitro* local pressure measurements. (b) Testing flow loops constructed based on the schematic diagram. The two ports on the organ perfusion device were connected to the corresponding ports on pressure sensors (shown in white line).

De-ionized (DI) water instead of blood served as working fluid in the test circuit due to the foaming and clogging issues of blood during the flow test. In order to evaluate the pressure difference through the organ perfusion device versus the flow rate of the main flow, the flow rate generated by the centrifugal pump was gradually increased from 0 to 250

mL/min in a 50 mL/min increment, and the corresponding pressure difference was recorded. Note that the flow from the centrifugal pump was approximated to be steady with constant flow rates. This setting represented the control group. Then the peristaltic pump was also switched on with increasing revolutions per minute (RPM) from 10 to 50 in increments of 10 and the corresponding pressure difference was monitored for pressure variations following deployment of the organ perfusion stent. Note that the organ perfusion device is flexible and deformable, which means the surrounding branch flow may affect the main flow. Also in reality, a pulsatile flow with systolic/diastolic pressure 120/80 mmHg and 60 beats/min will be more appropriate for human physiology conditions. However, the pressure difference across the device will be varied with time frames and this imposes challenges to pressure measurement.

4.2.3 Computational fluid dynamics (CFD) analysis

For two points along a streamline for incompressible flow in a tube, the Bernoulli equation is given as [91]:

$$\frac{P_1}{\rho g} + \frac{v_1^2}{2g} + z_1 = \frac{P_2}{\rho g} + \frac{v_2^2}{2g} + z_2 + \Delta h_f + \Delta h_m \tag{4.1}$$

where P_1 is the pressure at point 1, P_2 is the pressure at point 2, ρ is the density of the fluid, g is the gravitational acceleration, v_1 is the flow speed at point 1, v_2 is the flow speed at point 2, z_1 is the elevation at point 1 and z_2 is the elevation at point 2. The overall hydrodynamic loss is contributed by two major parts: friction on the straight section and sudden change in tube geometries.

Δh_f is the head loss due to the friction and is given by the Darcy-Weisbach equation:

$$\Delta h_f = f \frac{L}{D} \frac{v^2}{2g} \tag{4.2}$$

where f is the friction factor, L and D are the length and diameter of the straight tube, respectively. Δh_m is the minor head losses due to tube geometry changes in entries, exits, fittings and valves and can be characterized by:

$$\Delta h_m = \Sigma K \frac{v^2}{2g} \tag{4.3}$$

where K is the loss coefficient. The current tube for the main flow has two geometry changes: tapers with contraction and expansion. In between, a straight tube is placed.

For the tapered contraction, the diameter of the tube reduces from d_2 to d_1 along length l, we can define

$$\theta = \frac{d_2 - d_1}{2l}, \beta = \frac{d_1}{d_2} \tag{4.4}$$

For $\theta \leq 45°$,

$$K = \frac{0.8\sin\frac{\theta}{2}(1-\beta^2)}{\beta^4} \tag{4.5}$$

For $45° < \theta \leq 180°$,

$$K = \frac{0.5\sqrt{\sin\frac{\theta}{2}}(1-\beta^2)}{\beta^4} \tag{4.6}$$

Similarly, for the tapered expansion, the diameter increases from d_2 to d_1 along length l. For $\theta \leq 45°$,

$$K = \frac{2.6\sin\frac{\theta}{2}(1-\beta^2)^2}{\beta^4} \tag{4.7}$$

For $45° < \theta \leq 180°$,

$$K = \frac{(1-\beta^2)^2}{\beta^4} \tag{4.8}$$

In order to visualize the fluid flow patterns within the device, both the arterial and venous stents were modelled and meshed in ANSYS Workbench 15.0 Fluent (ANSYS Inc., PA, USA). Figures 31(a) and (c) illustrate the cross sections and dimensions of the arterial as well as venous OPS. The arterial stent device had a diameter of 1.3 cm in the larger section and diameter of 0.6 cm in the smaller section while venous stent device had a diameter of 2.2 cm in the larger section and diameter of 1.1 cm in a smaller section. Both of the devices had 2 cm long inlet and outlet regions, 10 cm long straight tube region and 1 cm transition regions (diameter contraction/expansion region). Figure 31(b) and (d) show the arterial stent model and venous stent model with meshed elements in ANSYS Workbench 15.0 Fluent, respectively. The entire fluid region within the OPS was partitioned into a series of elements with nodes. The inlet velocity was assigned by using the flow rate equal to 250 mL/min. Liquid water from ANSYS Fluent material database was modeled with fluid density $\rho = 998.2$ kg/m^3 and viscosity $\mu = 1.003\times10^{-3}$ kg/(m·s). The blood flow of a dying patient would expectedly decrease flow in the stent central lumen, with a reduction in the Reynolds

number and would be unlikely to deviate from laminar flow. Therefore, a laminar flow model was assumed and a set of simultaneous governing equations were solved on different nodes with pre-defined fluid properties and boundary conditions. We also assumed the device wall to be rigid and would not contract or expand with the incoming flow in order to simply the model into a pure fluid problem. The wall shear stress (WSS) for a Newtonian fluid is given by

$$\tau_{wall} = \mu \frac{\partial u}{\partial y}\bigg|_{y=0} \tag{4.9}$$

where μ is the dynamic viscosity, and $\partial u/\partial y$ at $y = 0$ is the velocity gradient on the wall. Therefore, WSS distributions on the stent wall can also be derived from the obtained velocity field.

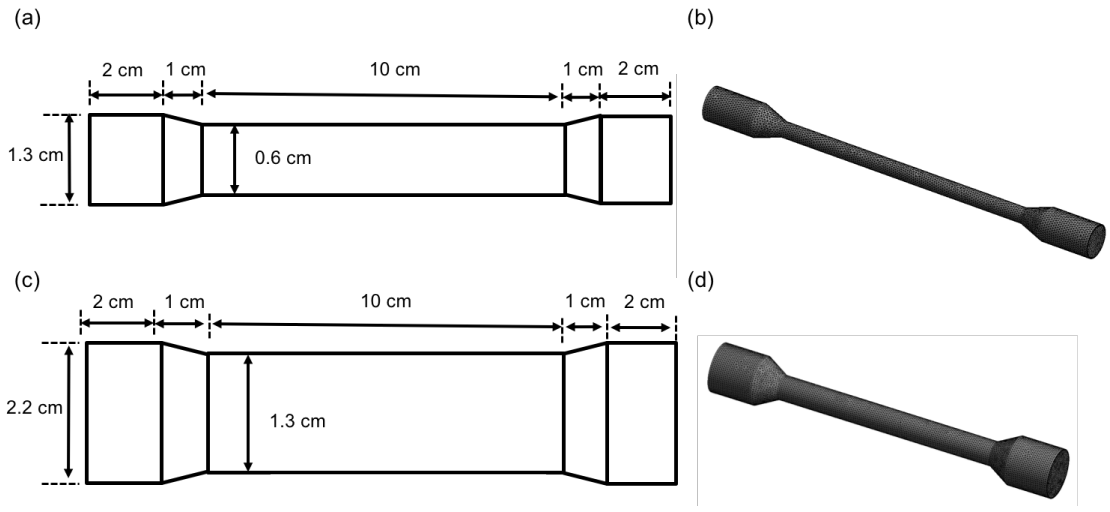

Figure 31: (a) Dimensions of the OPS in arteries. (b) Meshed arterial stent model in ANSYS Fluent 15.0 for CFD analysis. (c) Dimensions of the OPS in veins. (d) Meshed venous stent model in ANSYS Fluent 15.0 for CFD analysis.

4.3 RESULTS AND DISCUSSIONS

4.3.1 Prototype Organ Perfusion Stent (OPS)

Figure 32 illustrates the organ perfusion stent (OPS) for arterial and venous locations, respectively. The arterial OPS (Figure 32a) has 29 cm total length, which includes two flare regions (i.e., both in distal and proximal ends) for isolating cardiac blood flow from the organ area as well as a long middle sections for delivering the oxygenate blood to several organs. In order to prevent dynamic occlusion of the 10 Fr perfusion lumen, a nitinol mesh cage was attached at the distal end of the perfusion sheath as shown in figure 32. The 10 Fr sheath was attached along with the length of the arterial OPS confirming a tight integration during collapsing and deployment. This 10 Fr sheath plays an important role for device delivery, i.e., push rod. Over 10 times of collapsing and deployment testing with an 18 Fr delivery sheath *in vitro*, there was no significant device failure or damage occurred during the collapsing and deployment procedures. The venous OPS was similar to the arterial OPS, but the dimensions were larger consistent with the increased diameter of this vessel.

4.3.2 Computational Fluid Dynamics Results

With the calculation settings described in section 4.2.4, figures 33(a) and (b) demonstrate the fluid velocity contours within the arterial and venous OPS, respetctively. In arterial OPS case, the averaged flow speed increased significantly by 470% when the fluid entered the straight region from the inlet. A parabolic velocity distribution pattern with the maximum of 0.23 m/s was observed at the outlet region in figure 33(a). The WSS was then calculated from the velocity field and a maximum of 0.96 Pa was obtained on the boundary between the end of the contraction and straight region (figure 33(b)). Similarly, the averaged flow velocity increased by 290% when the fluid passed through the straight region in venous OPS case. At the outlet region, the maximum velocity was 0.074 m/s, which is much lower than the arterial OPS case. Also the WSS with a maximum of 0.18 Pa was obtained on the boundary between between the end of the contration and straght region (figure 33(d)). In summary, the arterial OPS exhibited both higher flow velocity and WSS as opposed to venous OPS

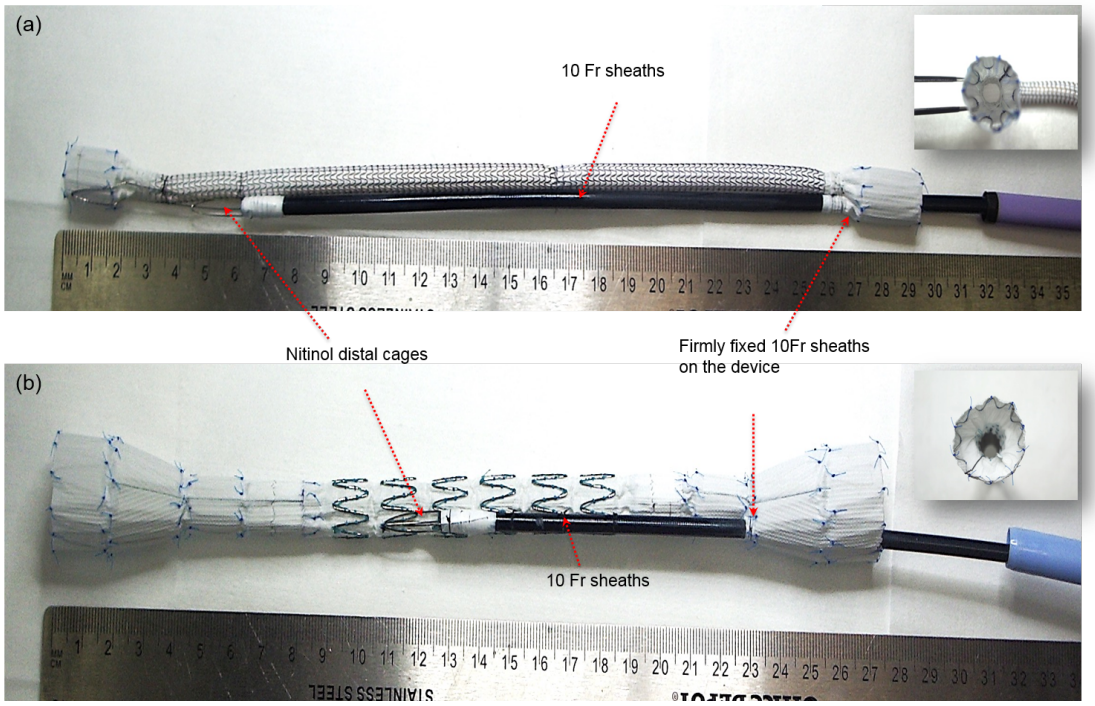

Figure 32: (Prototype OPS devices. (a) OPS designed for aortic (arterial) placement. (b) OPS for placement in the vena cava (venous).

with the same flow rate settings at inlet. This is due to smaller diameters in the arterial OPS. In two cases, the magnitudes of WSS are minimal and we expect that these would not be associated with anyserious injury of the endothelium or blood vessel wall [92].

4.3.3 *In vitro* Measurement of Local Pressure Alterations

For the arterial stent device, the pressure difference (in vertical axis) between inlet and outlet versus flow rate in the main flow loop (in horizontal axis) is plotted in figure 34(a). This baseline results of the flow loop without use of the organ perfusion stent represent the control group. Figure 34(a) reveals a linear relationship between pressure difference and flow rate with R^2 equal to 0.9802. When the flow rate in the main loop increased from 50 mL/min to 250 mL/min, the pressure difference between inlet and outlet of the organ perfusion stent increased from 0.23 mmHg to 1.56 mmHg, indicating that pressure difference only slightly

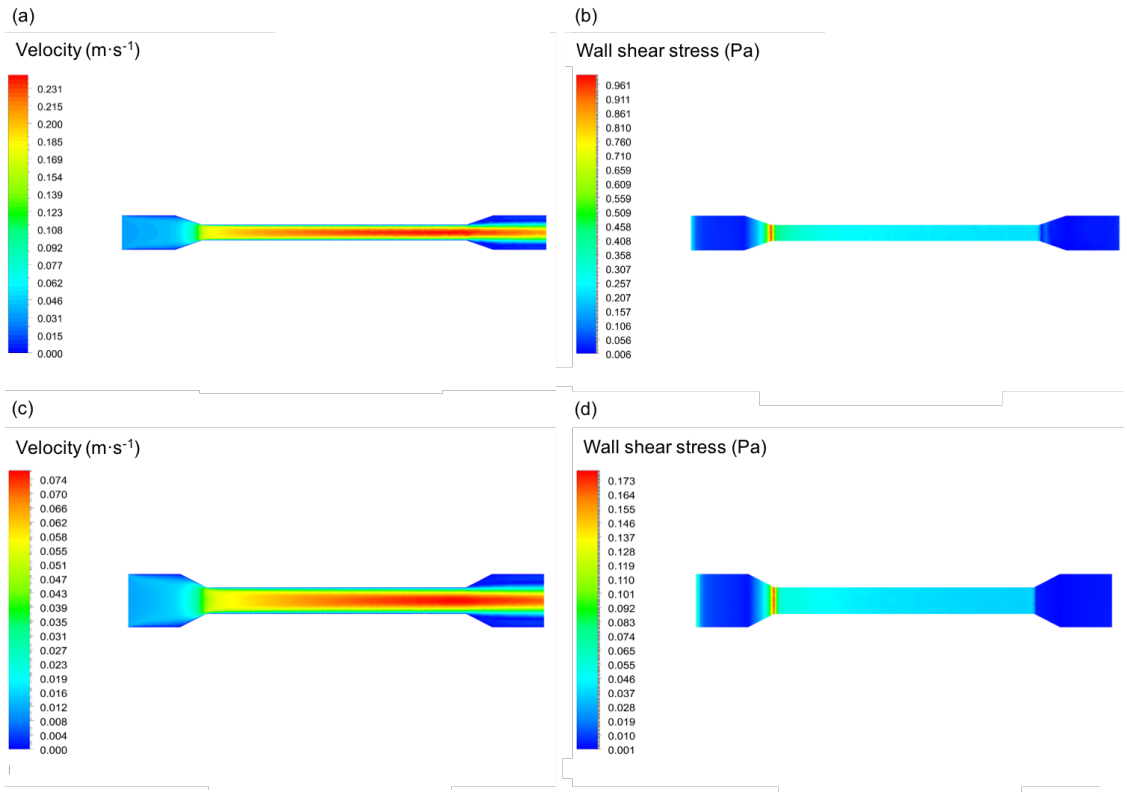

Figure 33: (a) Calculated flow velocity contours in arterial OPS. (b) Calculated WSS contours in arterial OPS. (c) Calculated flow velocity contours in venous OPS. (b) Calculated WSS contours in venous OPS.

increased by 1.33 mmHg with 200 mL/min flow rate elevations. Compared to the normal human blood pressure values (i.e., 120/80 mmHg), this pressure variation is negligible thus the implantation of our organ perfusion stent would pose no increased work on the human heart. Similarly, figure 34(b) presents the pressure difference when the perfusion procedures were applied to the side branch. The flow rate generated by the centrifugal pump was fixed at 200 mL/min. When the peristaltic pump rotation increased to 50 in a clockwise direction, the pressure change in the main stream only slightly increased by 0.15 mmHg. In addition, when the revolution direction in peristaltic pump was reversed, the change in the pressure difference is 0.14 mmHg. In summary, we conclude that the deployment of the stent in the artery and separate flow to the abdominal organs will generate a negligible load.

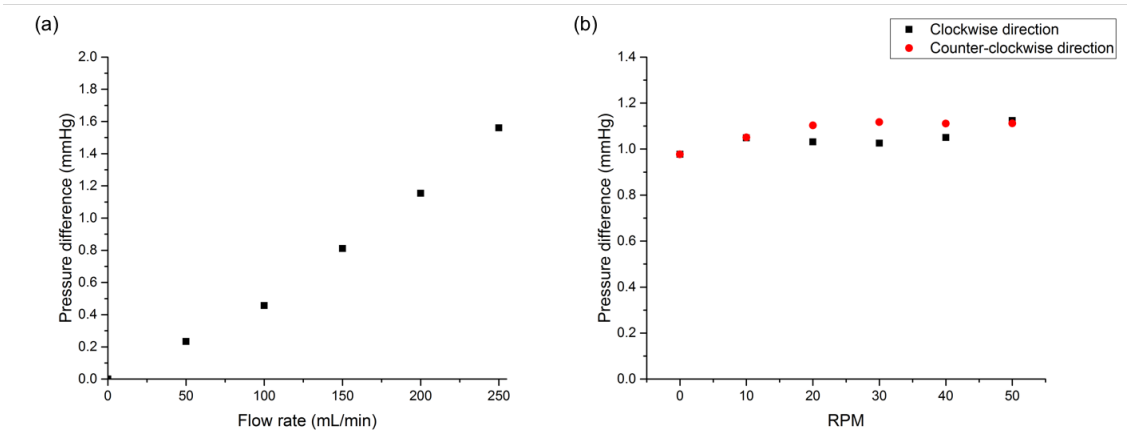

Figure 34: Measured pressure drop across the arterial perfusion stent device. (a) Pressure difference in arterial perfusion stent versus flow rate in the main stream without peristaltic pump. (b) Effect of side branch flow on the pressure drop (the main flow rate was fixed at 200 mL/min).

We repeated the procedures described above in the venous stent device using the same testing circuit configurations. Figure 35(a) summarizes the pressure difference (in vertical axis) versus the incoming flow rate (in horizontal axis) and a linear relationship was also observed with calculated R^2 equal to 0.9372. When the flow rate in the main stream increased from 50 mL/min to 250 mL/min, the corresponding pressure difference increased from 0.12 mmHg to 0.39 mmHg, indicating that pressure difference only slightly increased by 0.27 mmHg with 200 mL/min flow rate elevations in the main stream. The effects of peristaltic pump on the pressure variations across venous stent device were also assessed and the results were shown in figure 35(b). A negligible increase (0.16 mmHg) in the pressure difference between inlet and outlet was observed when the peristaltic pump rotation increased to 50 in a clockwise direction. While the revolution direction in peristaltic pump was reversed, there was a 0.22 mmHg elevation in the pressure difference compared to the control group. In summary, the simulated venous stent implantation and augmented flow to the abdominal organs did not significantly increase heart strain. In conclusion, our *in vitro*

pressure difference measurement suggests that implantation of the OPS into the vein would not significantly impact cardiac physiology.

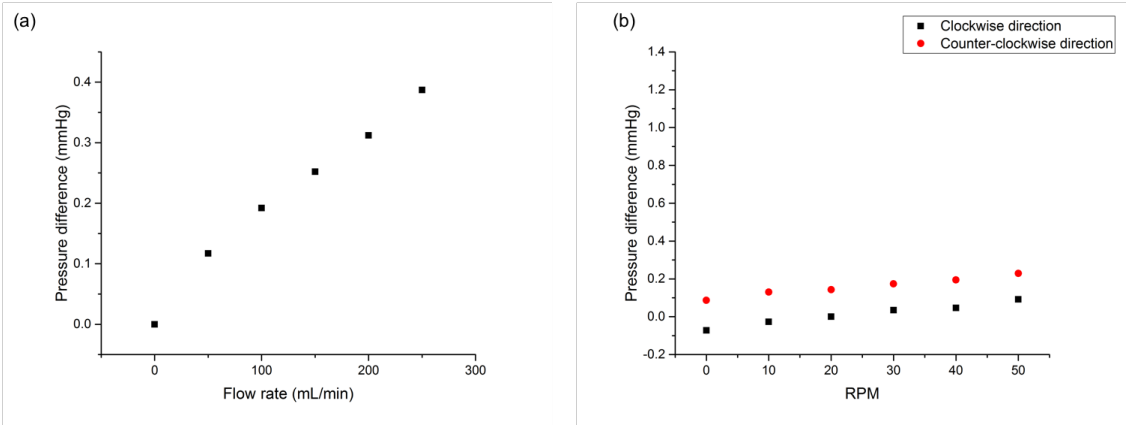

Figure 35: Measured pressure drop across the venous stent device. (a) Pressure difference in venous perfusion stent versus flow rate in the main stream without peristaltic pump. (b) Effect of side branch flow on the pressure drop (the main flow rate was fixed at 200mL/min).

4.3.4 *In vitro* Assessment on Device Delivery

Deployment of the arterial stent *in vitro* is shown in Figure 36 (a)1-5. Figure 36 a-1 demonstrates the collapsed arterial OPS (along with the 5 Fr catheter for delivery over a guidewire). By unsheathing the distal flare of the OPS was first deployed (a-2), then the distal end (with the nitinol cage) of the 10 Fr sheath was exposed (a-3). Figure 36 a-4 demonstrates deployment of 80% of the long device, then, a-5 shows the proximal flare deployment completing the device delivery.

Using a similar method, deployment of the venous OPS is shown in Figure 36(b) 1-5. Figure 8 b-1 illustrates the collapsed venous OPS in 22 Fr sheath. The 5 Fr catheter for guidewire delivery was not used here due to the bulkiness of the collapsed venous OPS device. No device failures were observed after 10 times of *in vitro* repeated collapsing and deployment tests. In addition, there was no 10 Fr sheath (i.e., push rod) migration (or failure) during collapsing and deployment, which is critical for successful and accurate delivery of the device.

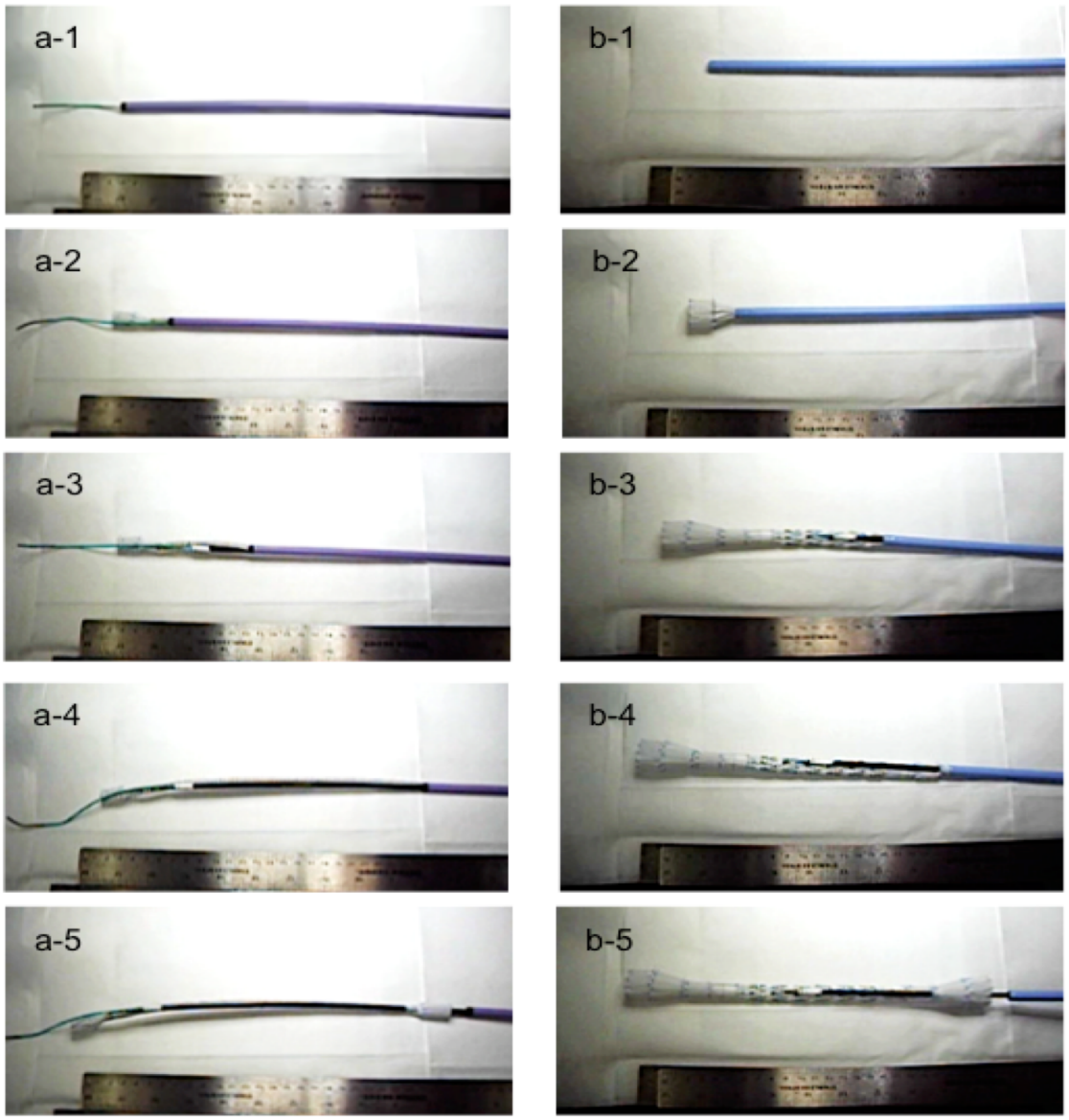

Figure 36: (a) 15: Deployment of arterial OPS with a 10 Fr perfusion lumen. (b) 15: Deployment of venous OPS with a 10 Fr perfusion lumen.

4.4 DISCUSSIONS

There are several limitations of our study. Our CFD calculations assumed the stent wall to be rigid, i.e., the wall would not move with the fluid and no expansion or contraction was

considered. However, the flexible graft materials covering the stent backbone will undergo expansion when the fluid enters the narrow straight region. Therefore, a fluid-structural-interaction model should simulate more realistic conditions. DI water instead of blood was used as the working fluid in the *in vitro* pressure measurement. Blood has fluid density ρ=1.025 kg/m^3 and viscosity μ =3.5$\times$10^{-3} kg/(m·s), which is actually 3.5 times of the DI water. Using a simple laminar model, the pressure drops with blood would be about 3 times higher than those with water assuming the blood viscosity is 3 times higher than that of water. Even accounting for this, the pressure drop in blood flow is less than 1 mmHg, which is still a minimal load to the heart. Also a pulsatile pump with systolic and diastolic pressure mimicking human conditions instead of constant flow should be used in order to monitor dynamic pressure variances. Our future work will include further evaluation of device functionality *in vivo* with advanced dynamic pressure monitoring platforms.

4.5 CONCLUSIONS

In this paper, we designed a novel compartmentalized stent graft to isolate the abdominal organs from ischemic injury. The two prototype organ perfusion stent grafts were fabricated for arterial and venous placement, respectively. One theoretical ethical concern is that the narrow section of the stent may increase back pressure and, in turn, cardiac stress, against ethical principles of the DCD donor. We examined pressure increases during device deployment *in vitro* and found only a negligibly small increase in local pressure drop across both the arterial and venous stent. These findings were consistent with our CFD estimates. The CFD analysis also showed that the local shear stress on the device is much smaller than the physiological condition. We conclude from these results that deployment of the stent would not significantly increase cardiac strain. The *in vitro* deployment test observed no device failure after 10 cycles and the device placement studies in swine model confirmed no gross vessel wall injury.

Traditional catheter approaches can certainly be used to cannulate the individual visceral vascular branches that perfuse the abdominal organs but obligates potentially hazardous in-

travascular contrast agents and requires the critically ill donor to be transported outside of intensive care unit. By contrast, the dual chambered stent rapidly consolidates multiple branches into a single compartment simplifying deployment in less than a minute. Clinically other applications of this approach may include delivery of medications directly to the abdominal organs that might otherwise have adverse effects if given systemically.

In conclusion, we believe the further development of dual chambered stents may offer the ability to increase the number and quality of livesaving donor organs for transplant while respecting key ethical considerations.

5.0 A RETRIEVABLE RESCUE STENT GRAFT FOR NONCOMPRESSIBLE HEMORRHAGE CONTROL

5.1 INTRODUCTION

Patient specific instrumentation (PSI) was introduced in the last several years to obtain a customized implant fit for patients with greater accuracy and shorter rehabilitation time as a growing trend in personalized medicine [93]. For example, PSI has emerged as a new technology in total knee arthroplasty (TKA) as a replacement for the traditional instrumentation [94]. The medical implantsmanufactured from magnetic resonance imaging (MRI), computed tomography (CT) imagery, or a combination, are specifically designed for the patient and intended to offer a faster, more accurate, and cost-effective surgery.

Recent advances in 3D printing have provided a new option to manufacture the patient-specific medical devices such as dental, spinal, and hip implants [95, 96, 97, 2, 98, 99]. Without the need for the surgeons to modify the implants into a desired shape, size and fit for the patient, implants and prostheses can be quickly produced and customized through the translation of X-ray, MRI and CT scans into digital print files [2]. It was reported that 3D printed customized implants can reduce the length of surgery time, reduce the risks of complications such as infections, and improve clinical outcomes [100, 101, 102]. While the future of 3D printing in medical implant applications is promising, for endovascular devices, which typically consist of ultra-thin metallic structures and polymeric membranes [103], there remain significant logistical issues for 3D printing. Typical endovascular devices need to be collapsed into a low-profile catheter with the diameter of a few millimeters for delivery and then deployed in the targeted vascular system up to 3 centimeters. It requires flexibility to accommodate dramatic device diameter reduction and subsequent expansion, sufficient

structural mechanical strength (e.g., radial force) to prevent device migration inside the vessels, and a smooth surface contact with the tissues to lower the risks of inflammation. These requirements cannot yet be fulfilled by current 3D printing technologies [104, 105, 106].

Some of the endovascular devices require ultra-thin polymeric membrane, commonly (expanded) polytetrafluoroethylene (ePTFE) [107, 108, 109, 110, 111, 112, 113, 114], to cover the metallic-framed backbone because it has relatively high tensile strength, controlled porosity, low surface energy, and superior hemocompatibility. This is often done by fabricating the membrane separately and then integrating it with the metallic frames. As the conventional polymeric membranes have already been set with pre-defined geometry and dimensions, modifications often need to be performed by the surgeons to tailor to the specific patient needs. It significantly lengthens the operation time and might increase the complications as well. Therefore, an approach to customize existing PTFE tubing would be beneficial to manufacture patient-specific endovascular devices within a clinically relevant timeframe. Aside from clinical use, rapidly customizable PTFE sleeves are virtually indispensable for research on custom endovascular devices. By using this approach, our group was able to quickly adapt PTFE to evolving needs and complicated sizing configurations, where other custom approaches would have introduced both significant delay and cost.

In this study, a rapidly customized expanded polytetrafluoroethylene (ePTFE) tube was investigated after combination with a laser-welded nitinol frame to create a stent graft. This device is intended for military or civilian vascular trauma, to be introduced and deployed endovascularly to rapidly control bleeding [115]. An important feature of this stent is that it allows for retrieval at the time of permanent repair, thus avoiding complications of current permanent stents that may be misplaced under emergency circumstances [116].

5.2 METHODS

5.2.1 Material selections

Two types of materials were selected to fabricate the customizable stent graft for the vascular injury management, including (1) highly stretchable expanded polytetrafluoroethylene (ePTFE) as the stent covering membrane and (2) superelastic thin nitinol wires as the metallic backbone. An extruded ePTFE tube (ZEUS, Inc., Orangeburg, SC) with an inner diameter of 0.394" $\pm$ 0.004" and a wall thickness of 0.005" $\pm$ 0.004" was used to cover the nitinol stent backbone for the study. The mechanical properties of the tube were investigated in the following section. The cold-drawn superelastic nitinol wire (Confluent, Fremont, CA) with diameter of 0.0155" was used for the stent backbone fabrication. The transformation temperature of the nitinol wire is between 5 and 18^{o}C, which is ideal for the superelastic behavior in the body temperature. Both ePTFE and nitinol are well-known biocompatible materials and widely used in endovascular devices including stents, stent grafts, occluders, guidewires and vascular filters.

5.2.2 *In vitro* and *in vivo* tests for evaluating devices functionality, feasibility, and biocompatibility

5.2.2.1 Mechanical characterization of ePTFE membrane The stress-strain behavior of the ePTFE membrane was measured with a mechanical testing system (FMS500, Starrett, MA). The 0.005 thick (thickness T) ePTFE samples were cut into 25 $\times$ 25 mm (length L $\times$ width W) size and affixed to the two film test grips (G1008, Mark-10 Co., NY), one movable on the top and while another fixed on the bottom (Figure 37(a)). The two grips were aligned carefully and the distance between two grips (D) was measured to calculate the strain. The grips on the top were connected to a load cell with the capacity of 500 N (FLC-500E, Starrett, MA) to measure the corresponding tensile force (F). As the ePTFE membrane exhibited anisotropic stress-strain behaviors, i.e., the membrane is less stiff (or easily stretched) in radial direction (along the length) than the longitudinal direction (along the width), the stretchiness tests in both radial and longitudinal directions were performed.

The travel displacement (ΔD) of the top grips was set as 40 mm with the velocity of 4 mm/min and 10 mm with the velocity of 1 mm/min for radial direction and longitudinal direction, respectively. The sampling rate was 100 Hz and a tablet connected to the mechanical testing system recorded the travel distance (ΔD) and load force (F) in real time. The stress (σ) and strain (ϵ) of the ePTFE membrane can be calculated from

$$\begin{aligned} \sigma_{radial} &= \frac{F}{W \cdot T} \\ \sigma_{longitudinal} &= \frac{F}{L \cdot T} \\ \epsilon &= \frac{\Delta D}{D} \end{aligned} \tag{5.1}$$

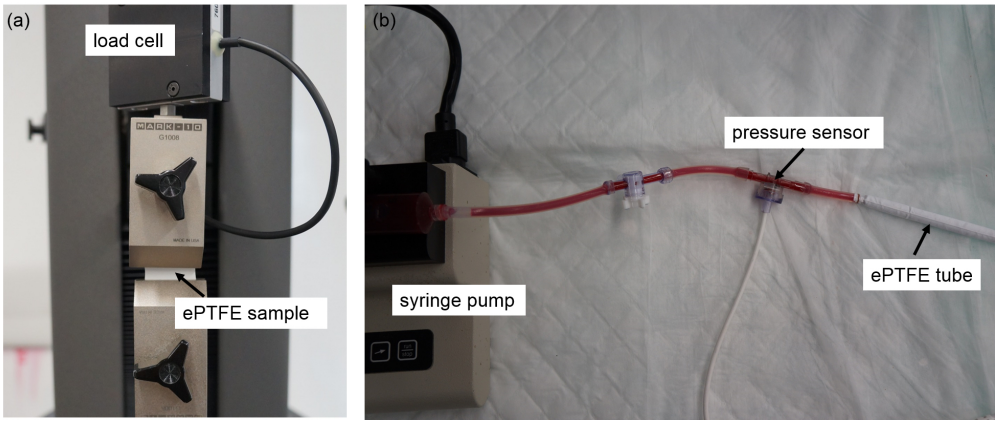

Figure 37: (a) Set-up for the mechanical stretching of the ePTFE membrane to measure the stress-strain behaviors; (b) Set-up for the ePTFE sweat test *in vitro*.

5.2.2.2 Porosity calculation with the applied strain The ePTFE membrane was stretched radially to 200%, 400% and 550% (before fracture) using the methods described in section 5.2.2.1. Four samples including original (non-stretched), 200% stretched, 400% stretched and 550% stretched ePTFE membranes were characterized by scanning electron microscopy (SEM-ZEISS Sigma500 VP, Carl Zeiss Microscopy, LLC, NY) after 45 seconds sputter deposition of thin Palladium layer. The SEM images with 1000x magnifications were imported into Matlab R2014a as the matrices of greyscale values. The number of pixels on

the ePTFE fiber region was counted in the matrices so the porosity of the ePTFE membrane with different stretchiness levels can be calculated from

$$\text{porosity} = 1 - \frac{\text{number of pixels on fiber regions}}{\text{total number of pixels}} \tag{5.2}$$

5.2.2.3 *In vitro* sweating test for evaluating potential leakage of ePTFE membrane Figure 37(b) shows the *in vitro* test setup for determining the ePTFE radial stretchiness with respect to the applied pressure induced by the incoming flow. The ePTFE tube was cut into 10 cm long with one end completely sealed using glue. Another end of ePTFE tube was connected to a pressure sensor (PRESS-S-000, PendoTECH, NJ) to measure the corresponding fluid pressure inside the ePTFE tube. The heparinized pig blood was used as the working fluid inside the test circuit and a syringe pump was utilized to generate the continuous blood flow into the ePTFE tube. The flow rate was set as 50 mL/h. At the pressure levels of 30, 60, 90 and 120 mmHg, the corresponding ePTFE tube diameter as well as length were measured respectively and plotted against the pressure level changes. The test was repeated three times to calculate the average and standard errors. At the meantime, the ePTFE tube surface was monitored for monitoring any blood leakage during the tube expansion.

5.2.2.4 *In vitro* early thrombosis evaluation of ePTFE Three sets of ePTFE samples (5mm x 5mm) were prepared with pre-stretchiness of 0%, 200% and 400%, respectively, to be fixed on the glass substrate and placed in the petri dish. Each set of 3 samples were immersed into the fresh blood directly drawn from the living pig (i.e., non-heparinized blood) for 1, 2.5 and 5 minutes to assess the early thrombotic response of the ePTFE. Then the samples were gently rinsed with saline immediately. The following protocols were used to fix the red blood cells on the ePTFE polymer surface for SEM purposes: 1) add 2.5% glutaraldehyde on sample surface for 5 minutes at room temperature and rinse with phosphate-buffered saline (PBS); 2) place the samples in 30%, 50%, 70%, 90%, 95% and 100% ethanol successively for 5 minutes each at room temperature; 3) place the samples in 100% ethanol for 5 minutes; 4) add hexamethyldisilazane (HDMS) on sample surface and incubate for 5 minutes; 5) remove

HDMS and the leave the samples dry in the room temperature. Then the samples were coated with palladium and subsequently characterized by SEM. As a control, we repeated the process described above using heparinized pig blood and the blood cell adherence on ePTFE sample was observed under SEM.

5.2.2.5 Finite element analysis (FEA) of nitinol stent crimping process The stent crimping modeling was performed in Abaqus CAE 2016. Figure 38(a) shows the 3D model used in the finite element analysis. Note that the stent model was simplified with a constant diameter cylindrical design, while the prototype has a tapered design based on the anatomy of the swine model. The crimper function was modeled with SFM3D4R elements (4-node quadrilateral surface element with reduced integration) and the stent backbone was modeled with 20,890 C3D8R elements (8-node linear brick element with reduced integration and hourglass control). The element quality was checked using the mesh verification to avoid mesh distortion. The nitinol material property was defined as Youngs modulus $E =$ 60 GPa and Poissons ratio $\nu = 0.3$ [70]. The contact between the crimper and the stent backbone surface was defined as frictionless in the tangential direction and hard contact in normal direction so the stent will be crimped along with the crimper diameter reduction. A displacement loading normal to the crimper surface with magnitude up to 40% of the stent diameter was applied on the crimper outer surface (Figure 38(a)) and the corresponding stress/strain distribution as well as reactional radial force was calculated from the software.

5.2.2.6 *In vitro* radial force measurement of nitinol backbone A stent crimping experiment was conducted to quantify the radial force of the prototype superelastic nitinol stent backbone in vitro. Figure 38(b) and 38(c) show the measurement configurations using the mechanical testing system. Dacron was selected as the crimper material due to its mechanical property. One end of the Dacron strap (Sailrite Enterprises, Inc., IN) was glued to the stainless steel bar at the bottom while the opposite end was clamped firmly by a grip connected to a load cell. The Dacron strap was wrapped around the stent backbone and exerted forces on the stent surface to crimp it approximately radially as the moving stage pulled the Dacron strap up with the displacement magnitude equal to 40% of the

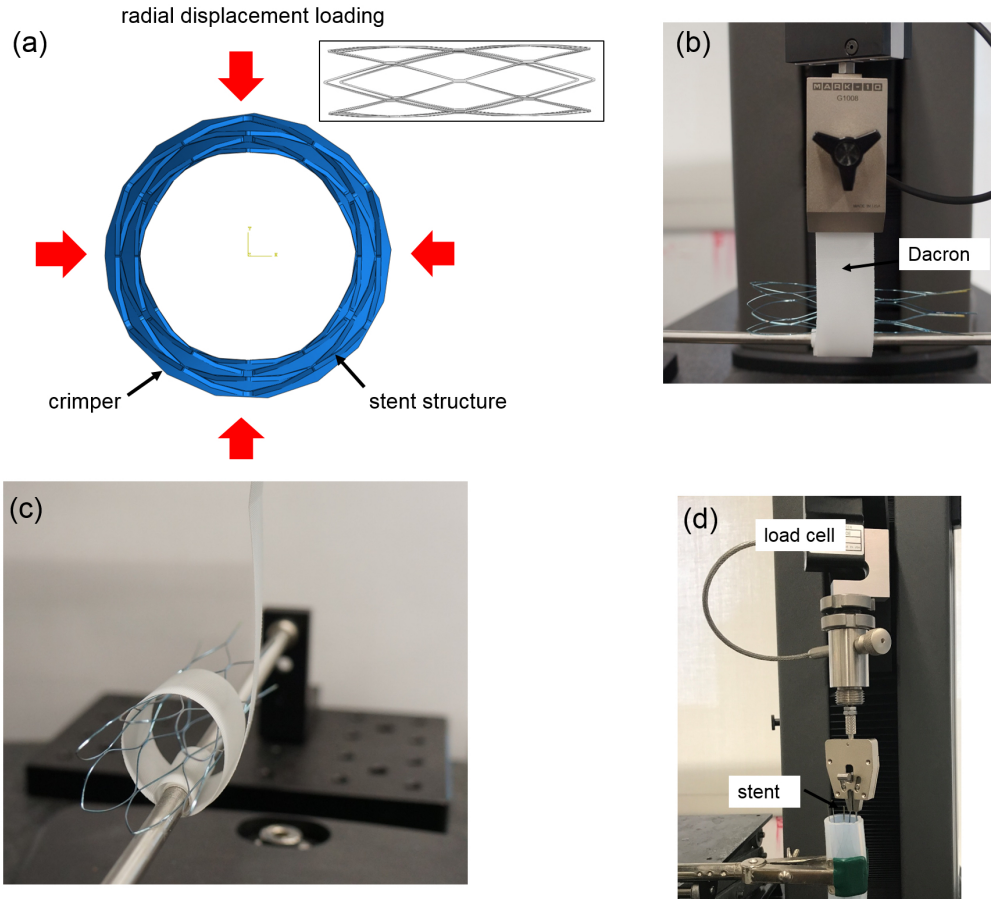

Figure 38: (a) 3D model of stent backbone and boundary conditions for stent crimping in Abaqus, (b) (c) experimental set-up to measure the radial force of the stent backbone, (d) experimental set-up for stent pullout force in a silicone tube.

stent perimeter. The start position where the Dacron strap just had contact with the stent backbone was determined when the measured load force first exceeded a small threshold value of the load cell. Both the displacement and hoop force can be measured from the mechanical testing system. Then the radial force can be calculated from the hoop force using the following equation [117]:

$$F_{radial} = 2 \cdot \pi \cdot F_{hoop} \tag{5.3}$$

The radial force with respect to stent diameter reduction (%) was plotted and compared with the FEA results. As the prototype stent has a tapered design (i.e., the diameter in the distal strut region is larger than the proximal strut region), we measured the radial force in these two regions separately.

5.2.2.7 *In vitro* force analysis and measurement to assess device migration

When the stent graft was deployed inside the vessels, the contact pressure can be calculated using the following equation with an elastic cylinder compressed into another cylinder model [118]:

$$P_c = \frac{\delta}{R\left[\frac{1}{E_o}\left(\frac{r_o^2+R^2}{r_o^2-R^2}+\nu_o\right)+\frac{1}{E_i}\left(\frac{R^2+r_i^2}{R^2-r_i^2}+\nu_i\right)\right]} \tag{5.4}$$

where δ is the overlap, R is the nominal radius, r_o and r_i is the inner radius of the outer cylinder (vessels) and inner cylinder (stent graft), respectively. And E_o, ν_o, E_i, ν_o is the Youngs modulus and Poissons ratio associated with outer cylinder and inner cylinder materials. Then the pullout force of the stent graft inside the vessels to determine the stent migration can be calculated from [118]:

$$F = \mu(P_c \times A) \tag{5.5}$$

where F is the pullout force, A is the contact surface area, and μ is the coefficient of friction.

In order to evaluate the stent migration inside the vessels, we measured the pullout force of the stent backbone from the silicone tube to mimic the stent dislocation (Figure 38(d)). The prototype stent backbone was collapsed into silicone tubes with the inner diameter of 0.5 and 0.75, respectively, i.e., the oversizing of the prototype stent backbone is about 51% and 27%. The silicone tubes were fixed using a clamp on the bottom and the upper end of the stent backbone struts was clamped by a gripper connected to a load cell. The moving grip pulled the collapsed stent backbone out of the silicone tube by the distance of 4 mm with the velocity of 1 mm/min and the travel distance as well as corresponding pullout force in real time were measured and plotted.

5.2.3 Stent graft fabrication process

A nitinol stent backbone was mainly fabricated using a precision micro-laser welding process with the mechanical bending process [115, 119]. Two nitinol wires were bent to 60^o angle for easy fabrication of the first section of the backbone. The bent wires were welded side by side making a perfect cylindrical geometry of the first section. Then additional crossed welding spots were created at every 2 cm location by aligning the two wires side by side. The intensity of laser is 1.4 kW, time for laser excitation is 1.2ms, frequency is 3 Hz with step function waves, and spot size is 700 μm. Anatomically relevant aluminum mandrel was prepared using a conventional turning process for thermal shape setting of the laser welded nitinol backbone. The laser welded nitinol backbone was placed over the aluminum mandrel and tightly fixed with 0.015 Ga iron wires (Malin Co., OH). Thermal shape setting was performed under 500 ^{o}C for 40 min in the high temperature furnace (Lindberg/Blue M Moldatherm Box Furnace, Thermo Scientific, PA), and subsequently rapidly cool down in 25 ^{o}C deionized water bath for 5 min. The nitinol backbone was removed from the mandrel for the integration with ePTFE covering membrane. Prior to the ePTFE covering process, two Tantalum (Td, Goodfellow, Huntingdon, UK) radiopaque markers were rolled from 30m thick foil, then, attached on both distal and proximal ends of the device.

Once the nitinol backbone is fabricated, ePTFE covering membrane should be prepared for the stent graft (Figure 39(a)). The 5 mm diameter ePTFE tube was stretched using 20-26 mm diameter balloon catheters (Z-MED Balloon Dilatation Catheter, B. Braun Medical Inc., PA). The length of balloon is 4 cm, therefore the balloon inflation was conducted several times for stretch the entire length of the tube. After the initial stretch of ePTFE tube using a balloon catheter, the tube diameter was tailored manually (Figure 39(b)). The stretched ePTFE tube was covered on the nitinol backbone and fixed using a biocompatible polymer adhesive (Loctite 4011, Henkel, Germany).

5.2.4 *In vivo* test with swine model

Yorkshire pigs (n=7) were placed under general endotracheal anesthesia as part of a University of Pittsburgh approved IACUC protocol with inhaled isoflurane. Abdominal exposure

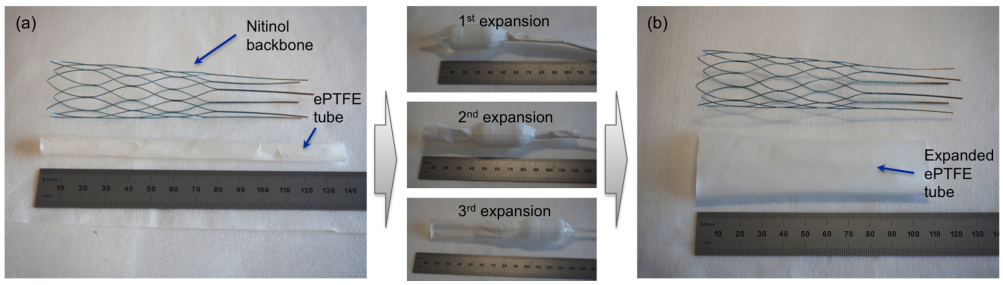

Figure 39: ePTFE covering process: (a) preparation of nitinol backbone and unexpanded ePTFE tube and (b) expanded ePTFE tube based on the anatomy of the animal model after three-step expansion

was obtained by an abdominal incision with exposure of the infrarenal vena cava (large abdominal vein). The animals were heparinized with 100 units/kg of heparin to simulate post-traumatic coagulopathy and as required by the porcine model due to rapid clotting of this model at baseline. Following 18 G needle access of the infrarenal vena cava, the seldinger technique was used to injure the cava with a 22 French dilator. The right femoral vein was accessed under ultrasound guidance followed by placement of a long 9 French sheath (Oscor, Palm Harbor, FL) by the seldinger technique. A 23-mm diameter and 10 cm long caval stent graft was delivered through the sheath and placed below the level of the renal veins under fluoroscopic guidance. Stent deployment was achieved by withdrawal of the vascular sheath while holding the wire stem of the stent stationery. A venous angiogram was then performed to document the vascular injury, stent control of the hemorrhage, and preserved flow beyond the stent. In the final step, the stent graft was retrieved by advancement of the vascular sheath to collapse the stent graft.

5.3 RESULTS

5.3.1 Results on ePTFEs material behaviors

5.3.1.1 Stress - strain behavior Figure 40(a) and (b) show the stress-strain behavior of ePTFE membranes under the tensile test using the test setup described in Section 5.2.2.1. The ePTFE membrane was stretched in radial direction of the tube, reaching the fracture strain of approximately 550% and the corresponding stress of 0.7 MPa (Figure 40(a)). This outcome demonstrates that the ePTFE membrane can be easily stretched up to 550% after the necking occurred during the tensile loading without mechanical failure. While there is no mechanical failure, there is changed structure of the fibers in ePTFE after the elongation. Detailed ePTFE structure analysis will be discussed in the next Section (41). Figure 40(b) shows the stress-strain behavior when the ePTFE membrane was stretched in longitudinal direction of the tube. The fracture occurred approximately at 8% strain and the corresponding stress at fracture was as high as 23 MPa.

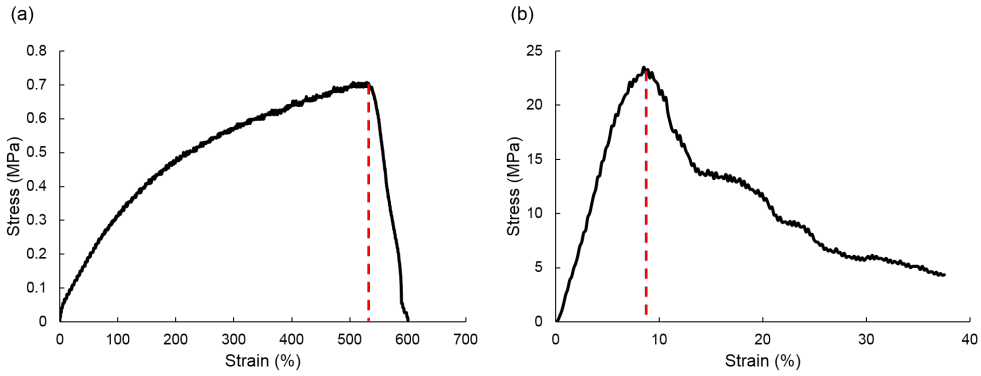

Figure 40: Stress-strain behavior of ePTFE membranes in tensile loading; (a) stress-strain curve in radial direction of the ePTFE tube; (b) stress-strain curve in longitudinal direction of the ePTFE tube

5.3.1.2 Porosity changes with applied strains in ePTFE Figure 41(a)-(d) present the SEM images of ePTFE membranes with 1000x magnifications under 0%, 200%, 400% and

550% applied strains, respectively. Figure 41(e) show the calculated porosity from Matlab with respect to the various applied strains. As can be seen, non-stretched ePTFE membrane exhibits an aligned dense microfiber structure with only 3% porosity that shows the adjacent fibers stay within a very small gap. With the increased strain in the radial direction of the tube, the gaps between fibers tend to be enlarged exhibiting a higher porosity of 14.4% and 20.87% in average for samples with 200% and 400% strain, respectively. In addition, the multi-layers of ePTFE fibers were stretched differently, therefore, wrinkled and relatively unorganized structures were found as shown in Figures 41(b) and (c). As the applied strain reached 550%, the gaps between fibers had the maximum of approximately 30 μm in length with 24.15% porosity in average, but the fiber networks were still connected and no fracture was observed under the fracture strain value. Both the qualitative and quantitative analysis on the SEM images have demonstrated that the structure porosity tends to increase along with the applied radial strain, but will reach plateau of 26% before the fracture occurs.

5.3.1.3 Sweating test results of ePTFE Figure 42(a) shows the ePTFE tube connected to the pump that is initially perfect cylindrical shape with the diameter of 5 mm without any stretch. While the pump pushes the blood into the tube, the ePTFE tube slowly expands with enlarged the pore sizes. Figure 42(c) shows the ePTFE tube diameter changes with the incoming blood from the syringe pump, which indicates the stretch levels of the ePTFE tube. The averaged diameter of the tube was significantly increased from 8.21mm to 21.97mm, 167% tube expansion as the fluid pressure elevated to 120 mmHg. No fracture or leakage was found at this level of pressure since the fracture strain of ePTFE polymer is higher than 500% in radial direction. Similarly, the ePTFE tube tends to be shortened during the expansion, and Figure 42(d) shows the length reduction with respect to the fluid pressure. Here, length reduction is denoted as the fraction of ePTFE tube length changes to the original length. At the pressure level of 120 mmHg, the ePTFE tube length decreased by about 8%, which is minimal compared to the significant diameter expansion. Hence, there is no sweating (or leakage) issue on the stretched ePTFE tube, which demonstrates that the tube can be used for the stent graft in the body where the applied pressure level is approximately 120 mmHg.

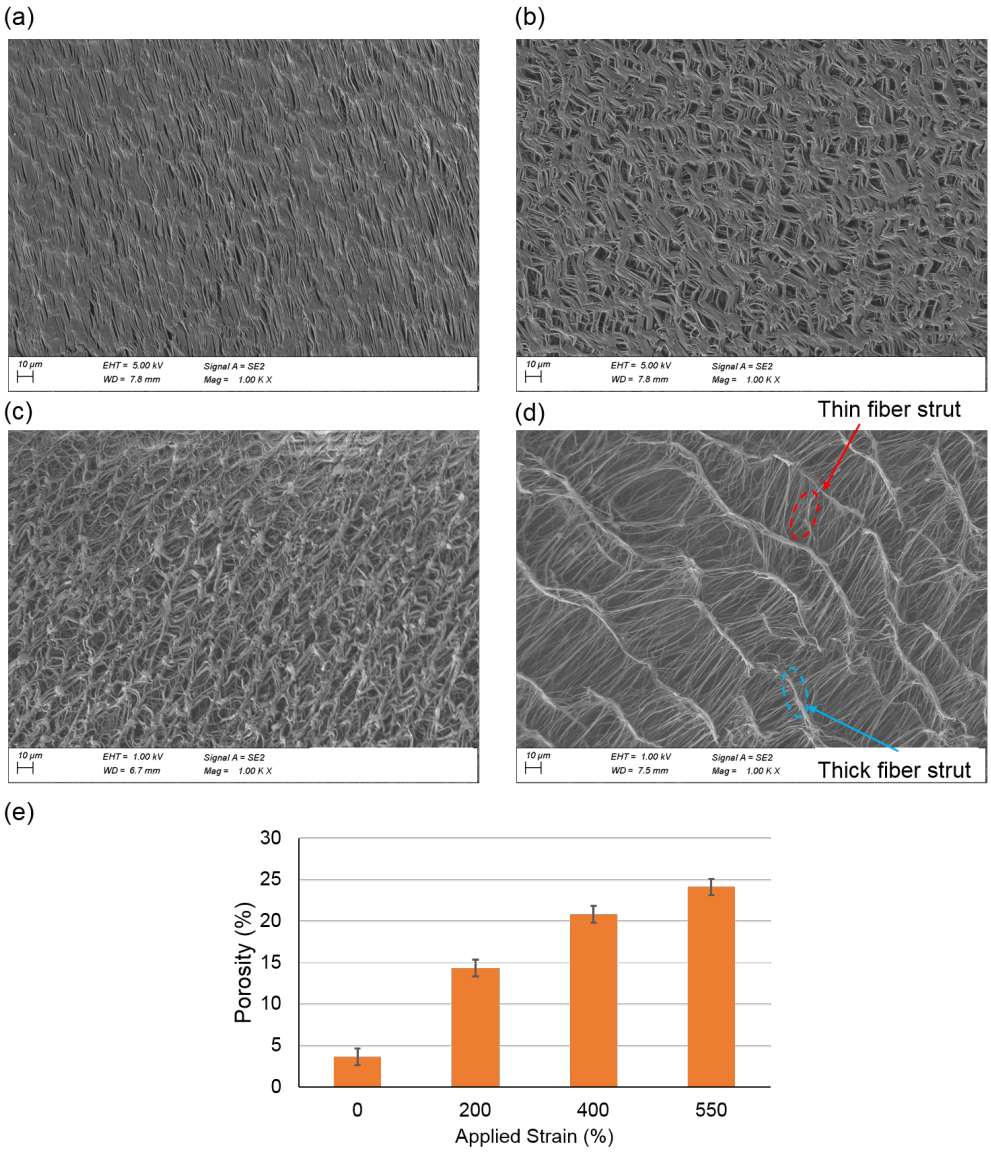

Figure 41: SEM images of ePTFE membranes with applied strain of 0% (a), 200% (b), 400% (c) and 550% (d) in radial direction under 1000x magnification. (e) (f) the calculated porosity changes with respect to applied strain.

5.3.1.4 Assessment of the early thrombogenic response of ePTFE Figure 43(a) shows the SEM images of non-heparinized blood product adherence on the ePTFE surface with 0%, 200% and 400% stretchiness levels for 1, 2.5 and 5 minutes, respectively. The

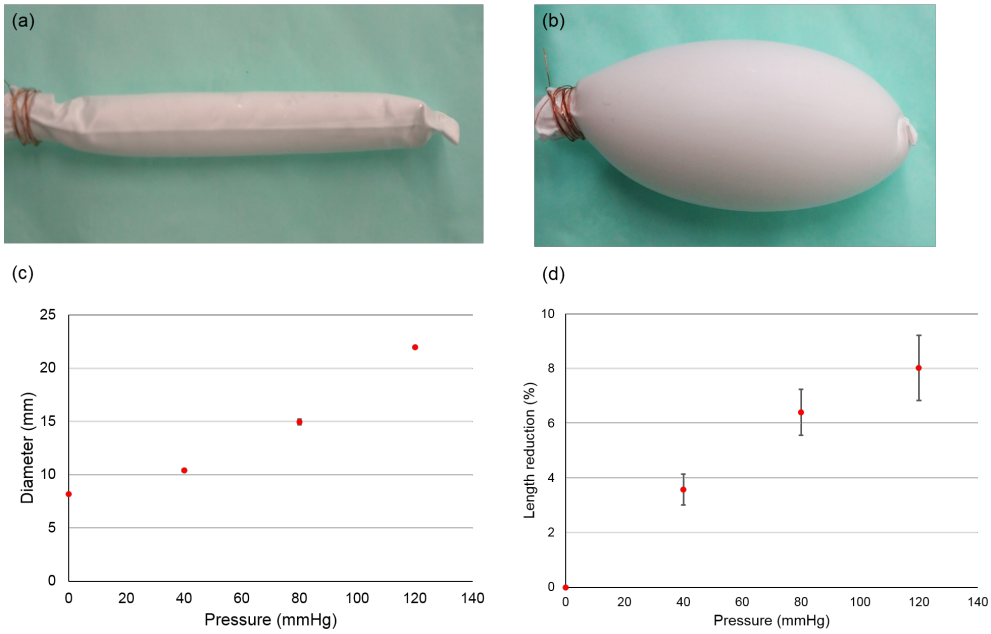

Figure 42: (a) ePTFE tube before the sweat test; (b) expanded ePTFE tube after the test; (c) ePTFE tube diameter changes with respect to fluid pressure; (d) ePTFE tube length reduction (%) with respect to fluid pressure.

number of blood cells (i.e., mostly red blood cells) adhered on the ePTFE surface increased significantly as the immersion time into the fresh pig blood increased from 1 minute to 5 minutes. It confirms that more blood cells will grow onto the ePTFE surface if it has contact with the surface for a longer period of time. For medical device applications, these results suggest minimizing the device exposure to the blood in order to reduce the risks of thrombosis on the device surface. Figure 44(b) also demonstrates that there was no significant difference on blood cell attachment on ePTFE surface for different stretchiness levels. For the stent graft fabrication, the ePTFE membrane will be expanded before wrapping onto the stent backbone and in vitro results showed stretchiness level has no influence on the thrombosis formation.

While the blood products adherence study with non-heparinized blood is important to assess the hemocompatiblity of the material used in the stent graft (i.e., ePTFE), identical

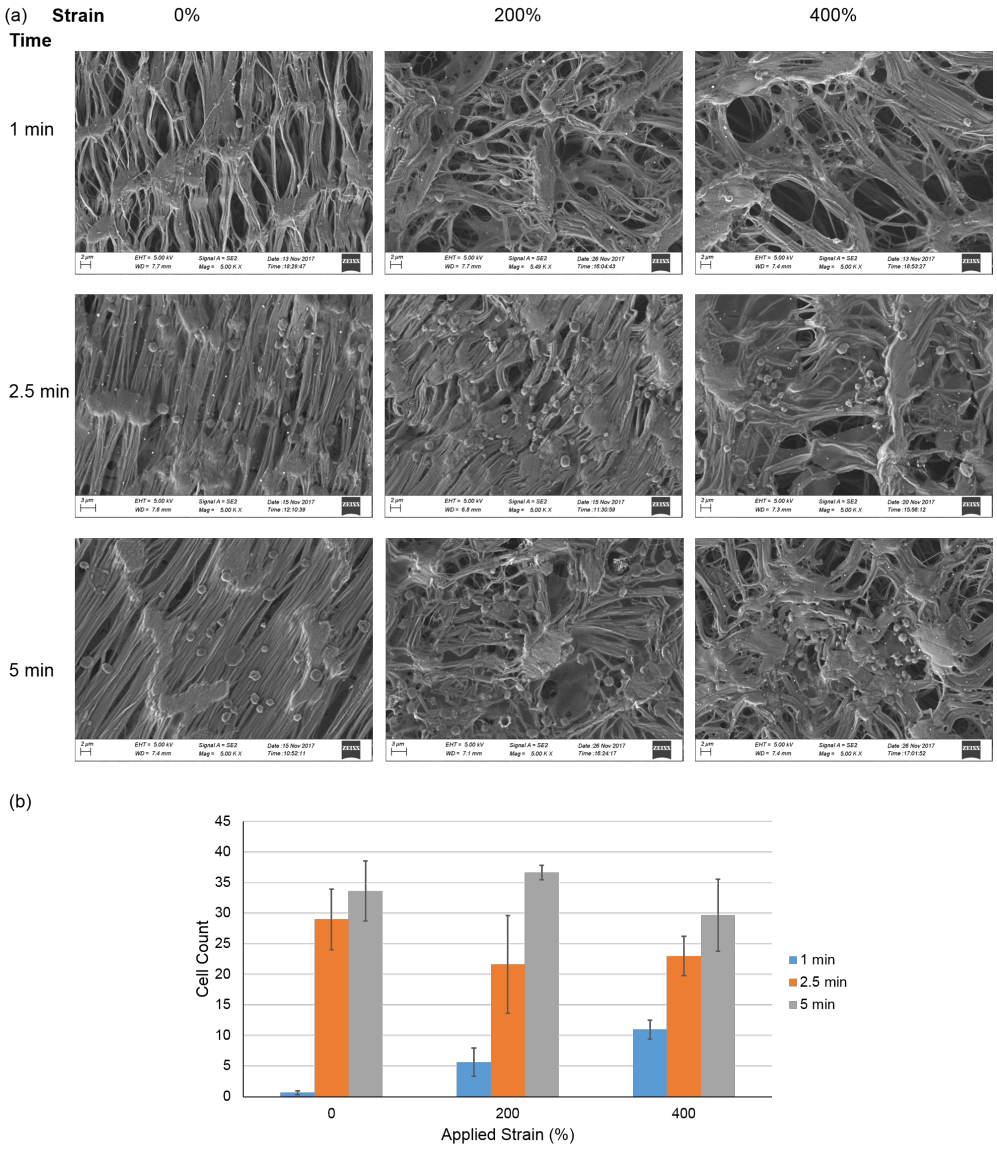

Figure 43: (a) Representative SEM images of early thrombosis on three sets of ePTFE samples after 1, 2.5 and 5 minutes in vitro under 5000x magnifications using fresh non-heparinized pig blood. (b) Number of cell counts on ePTFE samples after 1 2.5 and 5 minutes.

study is needed with heparinized blood because anticoagulant solutions frequently injected to the blood stream during the endovascular procedure. Figure 44(a) shows the representative

SEM images of blood cells adhrerence on ePTFE sample surface with heparinized blood. As the blood are less prone to coagulate on ePTFE surface with heparin treatment, all the samples with 0%, 200% and 400% stretchiness exhibit clean surface with minimal or no blood cells visible when the samples were immersed in heparinized blood for 1, 2.5 and 5 minutes, respectively. Figure 44(b) summarizes the count of blood cell attachment on the sample surface. It can be observed that the blood cells with the heparin treatment are less likely to be attached on the ePTFE sample compared with the blood cells from the one without heparin treatment. Again, this outcome demonstrate there is no significant influence of the stretchiness levels for the hemocompatiblity.

5.3.2 Results on nitinol backbones mechanical behaviors

5.3.2.1 FEA results of crimping process of the nitinol backbone Figure 45(a) and (b) show the computationally modeled stress and maximum principal strain (MPS) field when the stent backbone was crimped by up to 40% considering the targeted vessel size. The maximal stress is 456 MPa and the maximal MPS is 0.6%, which is below the fracture strain of nitinol [68]. Therefore, our nitinol backbone can be crimped down to 60% of the original size successfully without any mechanical failures. Also, as we can see from the calculated stress and strain fields in FEA results, the junctions of the struts exhibit both highest stress and strain values while the straight struts exhibit relatively negligible stress and strain values. Abaqus also calculated the corresponding radial force exerted by the stent backbone during the stent crimping process at the diameter reduction of 10%, 20%, 30% and 40% and Figure 9(c) plots the radial force against stent diameter reduction (yellow line). It can be observed that the radial force increased from 0.60 N to 2.98 N when the stent diameter reduction increased from 10% to 40%.

5.3.2.2 *In vitro* measurement of the radial force Figure 45(c) (green and blue dots) show the measured radial force using the test setup described in section 5.2.2.6. As the nitinol backbone has a tapered design, we measured the radial force in large section as shown in blue dots (distal end) and small section as shown in green dots (proximal end) separately.

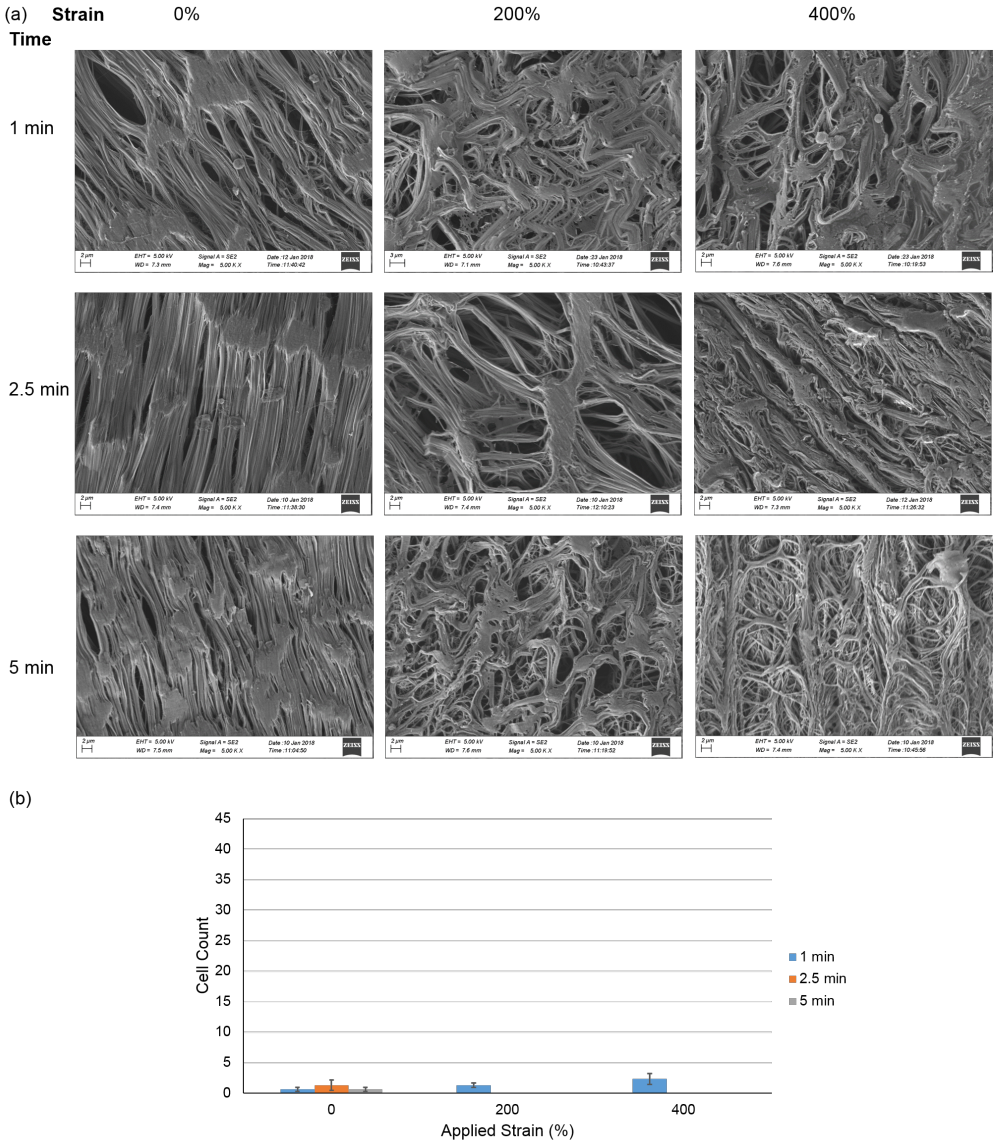

Figure 44: (a) Representative SEM images of early thrombosis on three sets of ePTFE samples after 1, 2.5 and 5 minutes in vitro under 5000x magnifications using heparinized fresh pig blood. (b) Number of cell counts on ePTFE samples after 1 2.5 and 5 minutes.

The large section exhibits a higher radial force compared with the small section, as the large section experiences a higher strain deformation when the both sections are crimped into the same diameter size. As can be seen from the plots, the radial force increased from 0.75 N

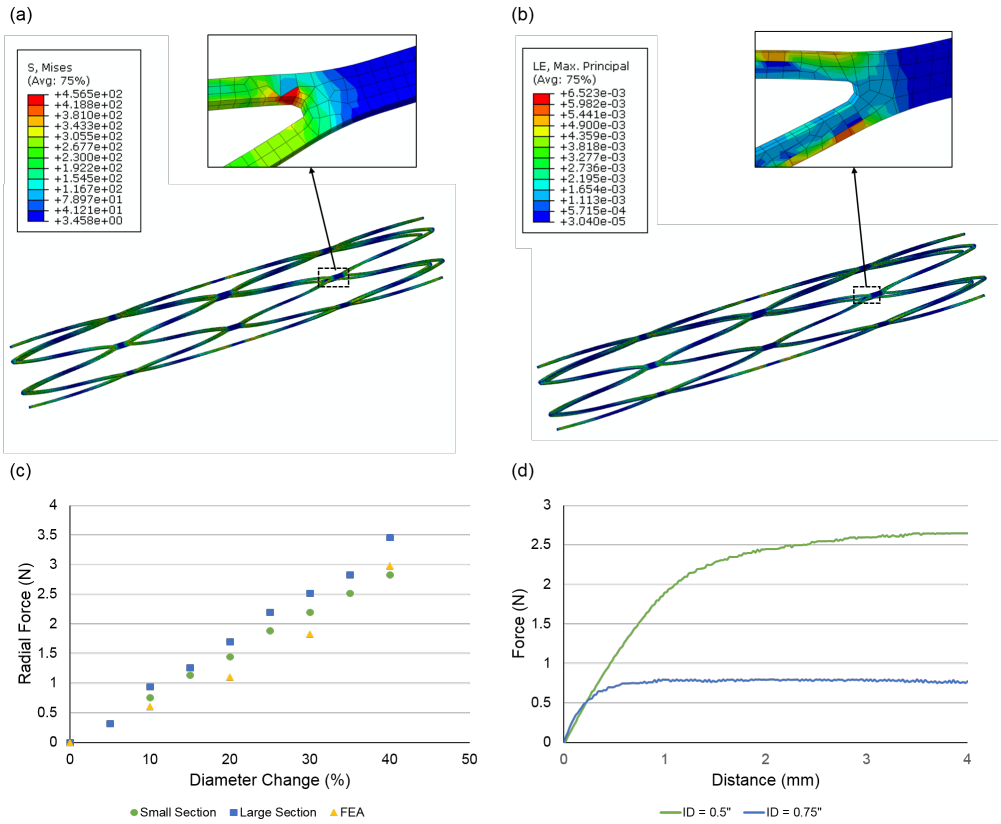

Figure 45: (a) (b) Computed stress and strain distributions during stent crimping analysis in Abaqus. Unit of stress: MPa. (c) Calculated radial force from FEA and in vitro measurement. (d) Measured pullout force in two silicone tubes with ID of 0.5 and 0.75.

to 2.83 N for small section when the stent diameter reduction ramped from 10% to 40%. Similarly, the radial force value was from 0.94 N to 3.46 N for large section. The FEA results matched well with the experimental results.

5.3.2.3 *In vitro* force analysis and measurement to assess device migration The pullout force can be defined as the frictional force between the artery wall and the stent graft during the stent movement. Here, we used a silicone tube for the artery model. The measured pullout force of the stent backbone inside a silicone tube with ID of 0.5 (green line) and 0.75 (blue line) was plotted in Figure 45(d). From the plot we can see that the pullout force in

a silicone tube with ID of 0.5 (51% oversizing) is about 2.65 N, which is much higher than the one in a 0.75 (27% oversizing) tube (0.79 N). The pullout force is related to the contact pressure between the collapsed stent and the tubes and a higher pullout force inside the tube presents lower risks of stent migration inside the targeted vessels during the treatment. On the other hand, the higher contact pressure also presents high risks of damage to the vessel walls.

5.3.3 Stent graft prototype

Nitinol stent backbone was fabricated using a precise micro-laser welding process and subsequently Td radiopaque makers were attached on both distal and proximal ends as shown in Figure 46(a). The micro-laser welding technology for the nitinol wire enables the stent backbone fully customizable since both the spot welding in narrow regions and thermal shape setting process can easily tailor the geometry customizing the backbone structure. For the in vivo studies, two prototypes have been successfully fabricated, which were smoothly collapsed and inserted in 8-9Fr delivery sheaths (Figure 46(b)). Two types of prototype devices are shown in Figure 46(c)-(f). Figure 46(c) and (d) show the nitinol backbone covered by ePTFE from outside. The expanded ePTFE by ballooning was placed over the collapsed nitinol backbone, then the backbone was deployed. A biocompatible polymer adhesive was minimally applied in each welded locations. Figure 46(e) and (f) show the nitinol backbone covered by ePTFE inside. The expanded ePTFE was placed inside the deployed nitinol backbone for attaching the membrane on the nitinol backbone. As can be seen in the panel inside the Figure 46(e), the polymer adhesive was applied everywhere the nitinol wires meet with the ePTFE membrane to securely attach the membrane.

The first prototype (Figure 46(c) and (d)) showed slightly better performance for preventing blood vessel bleeding, however, some portion of ePTFE membrane were caught by the sheath during the retrieval process. One advantage of this device is that the nitinol backbone consistently exerts its radial force, so the application of the polymer adhesive could be minimized, which is beneficial for highly collapsible structure with two different materials (i.e., nitinol and ePTFE). The second prototype shown in Figure 46(e) and (f)

showed no potential ePTFE catching issue because the ePTFe membrane is surrounded by nitinol backbone which collapsed outside. While the inside covered stent graft showed similar (or slightly lower) performance in terms of bleeding prevention, there are potential issue of the detachment of the ePTFE membrane from the nitinol backbone during the collapsing and deployment processes because all interfaces between nitinol and ePTFE were attached. Therefore, both type of devices were used in in vivo swine tests and have successfully demonstrated the feasibility and safety of the device, even though there are a few minor issues that would not deter the tests.

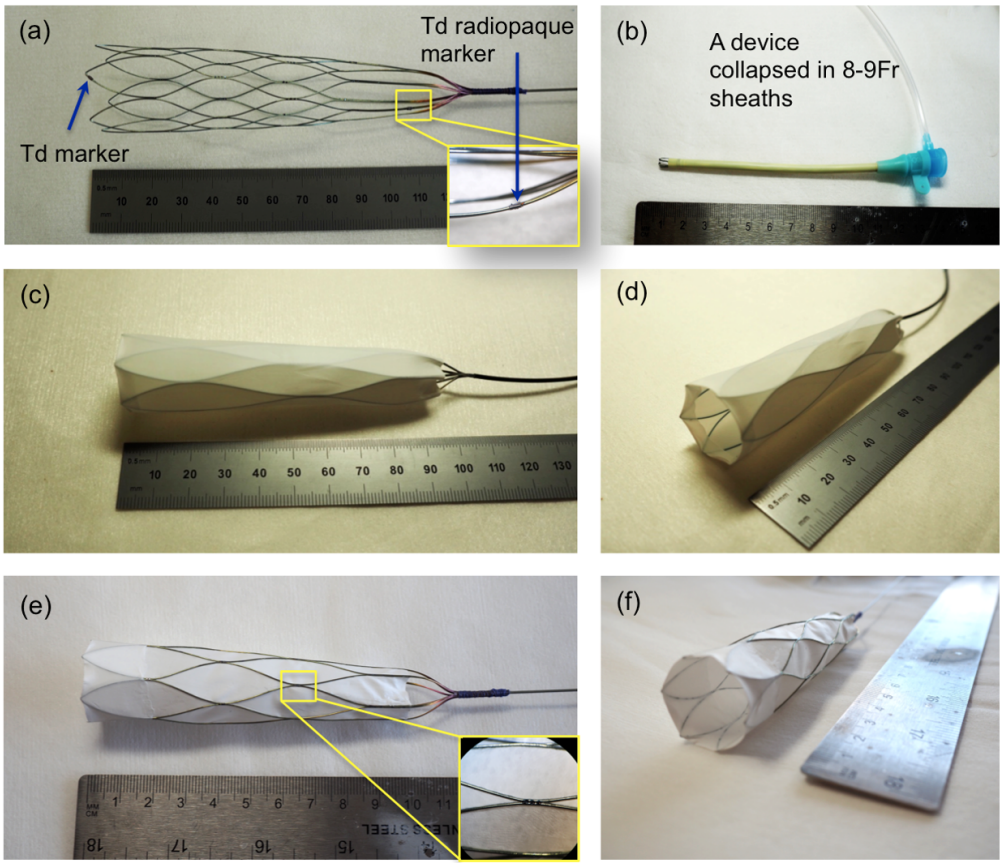

Figure 46: Prototype devices; (a) nitinol backbone with Td radiopaque makers, (b) collapsed device in 8-9Fr sheath, (c) side view of the device (outside covered), (d) front view of the device (outside covered), (e) side view of the device (inside covered), and (f) front view of the device (inside covered)

In vitro device performance test has been performed by evaluating the deployment and retrieval process. Figure 47(a) through (i) show the snapshot images of the in vitro test results on the deployment and retrieval processes of the device with a 9 Fr delivery sheath prior to the animal tests. Since the inside covered stent graft showed same performance of the outside covered stent, only the outside covered devices results are shown here. Figure 47(a) shows the fully collapsed device within a 9 Fr sheath for the venous stent graft. The sheath was withdrawn after holding the extension wire of the stent graft stationery and continued until all the device portions were deployed from the sheath (Figure 47(b)(d)). Once the device is fully deployed, the retrieval process can be tested by pulling the extension wire after holding the sheath in stationery to recapture the device (Figure 47(e)(i)). All device portions are fully collapsed and inserted within the sheath for retrieval process (Figure 47(i)). No significant visual damages or structural issues were found after 10 times repeated tests.

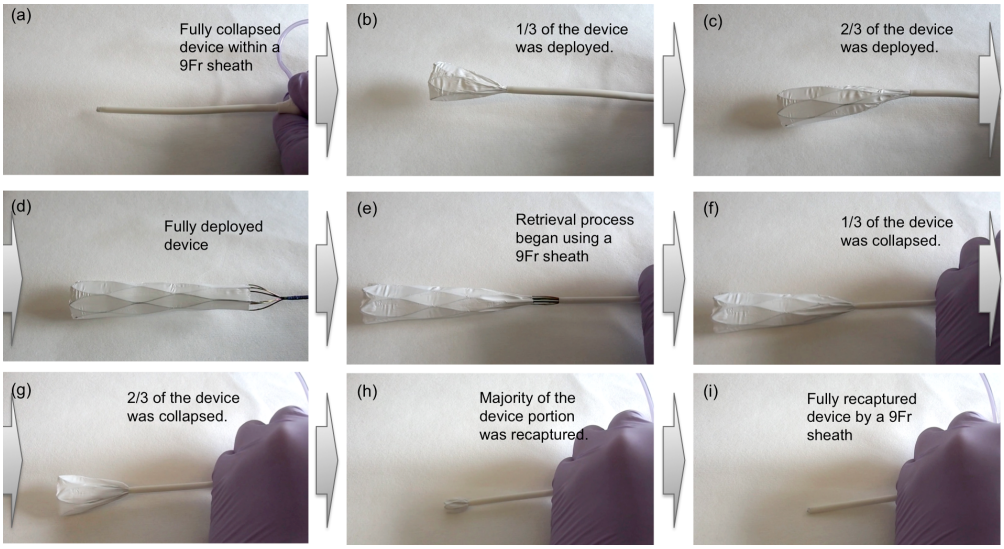

Figure 47: Device deployment and retrieval process using a 9Fr delivery sheath and outside covered stent graft.

5.3.3.1 Gross look of the device and SEM image analysis Figure 48(a) and (b) show the gross look of the harvested stent graft used in vein of the swine. As one can see in the images, there are some locations where partially detached ePTFE membrane from the

nitinol backbone observed after the device deployment and retrieval. The devices surface looks mostly pristine except a few locations where the thrombosis was formed. This issue has been resolved by adding a few tiny suturing locations in the recent devices (not shown here). More importantly, the surface of ePTFE was investigated via SEM image analysis. Figure 48(c) shows a global view of the SEM image of the ePTFE outside. There are thrombosis covered on some areas and ePTFE structure is shown beneath the thrombosis. Figure 48(d) shows highly magnified SEM image, which explains individual blood products adhered on the surface of ePTFE membrane. Aggregated platelets, fibrin networks, and accumulated red blood cells were found in the thrombosis.

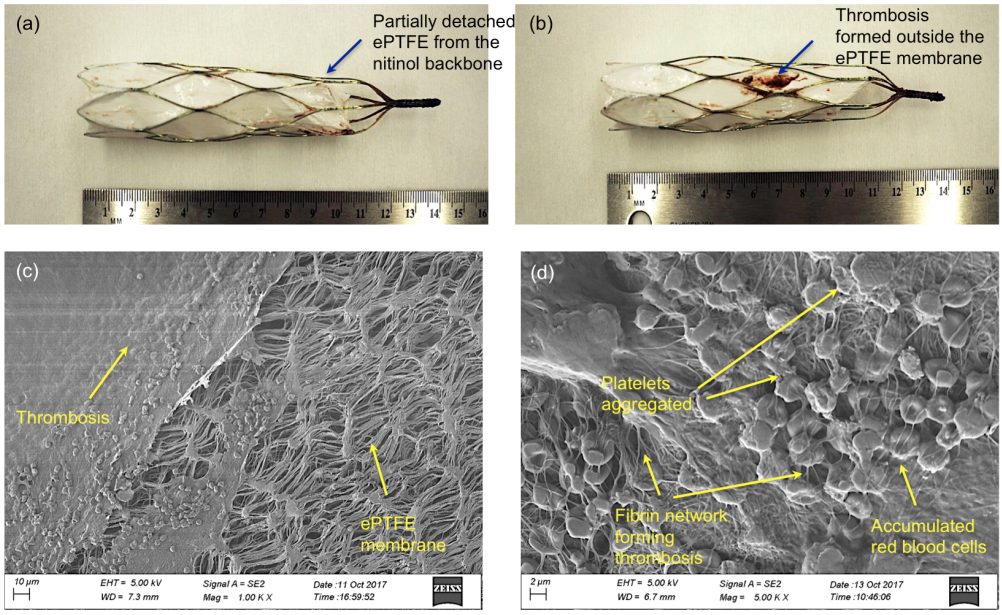

Figure 48: Gross look of the harvested device after the in vivo tests (a), (b), and SEM image analysis of the thrombosis formed on ePTFE membrane (c), (d)

5.4 DISCUSSION

Stress-strain curve of ePTFE membranes in Figure 4 confirms that the ePTFE membrane is less prone to be stretched in longitudinal direction compared with the stretchability in

radial direction, i.e., ePTFE membrane exhibits anisotropic mechanical behaviors in terms of tensile loading. This behavior can be explained from the microstructure of the ePTFE fibers observed under SEM. As the ePTFE fiber networks show the two types of fibers, the thick fiber struts (shown in blue circle in Figure 5(d)) and thin fibers connecting the fiber struts (shown in red circle in Figure 5(d)). The ePTFE membrane is easier to be stretched along the thin fiber directions and the fracture happens once the thin fibers are disconnected from the thick fiber struts. Because of this unique stretch behavior in different directions, the ePTFE tube shows anisotropic stress-strain behaviors under tensile loading. This unique behavior of ePTFE membrane is beneficial for the customizable stent graft fabrication if the device requires various diameters in one stent graft for the patients anatomy. Although the porosity increases to around 14.40% under the applied strain of 200%, no blood leakage was observed during the sweating test under 120 mmHg fluid pressure. The possible reason is that the thin fibers in ePTFE membrane tend to overlap each other during the elongation and thus reducing the pore size and creating the barriers for the blood flow to pass through.

For the mechanical behaviors of the nitinol backbone structure, there is a discrepancy between the FEA results and experimental results in terms of radial force, which can be attributed to the material property defined in FEA calculations and a simplified 3D model of stent backbone during the stent crimping modeling. Specifically, an elastic material model for the nitinol was assumed with the superelastic property simply ignored to reduce the computation complexity during the analysis. Also the 3D stent backbone model imported in Abaqus did not adopt a tapered design, both of which caused the deviations from the measurement results. In the in vitro pullout force measurement, it is only an approximation to the stent migration inside the vessels as the interactions between ePTFE grafts and vessel tissues were not taken into account. Also, the blood vessel tissue is more flexible compared to the silicone tubing used in the testing and the deployed stent will conform to the vessel geometries. Regarding the limitations in mechanical behaviors of nitinol backbone structure, the future work will include a more complete model with the defined superelastic material properties for nitinol and a tapered design in 3D stent backbone model in Abaqus. In the radial force analysis and measurement in vitro, the integration of ePTFE graft with the nitinol backbone also needs to be considered to account for the effects of expansion in ePTFE

graft. In the stent migration evaluations, the stent needs to be deployed in a more realistic tissue model to mimic the more flexible blood vessel tissues.

5.5 SUMMARY AND CONCLUSIONS

A novel customizable stent graft was manufactured from a highly-stretchable ePTFE tube and laser-welded nitinol backbone. Various in vitro study results including mechanical behavior, porosity, sweating, and biocompatibility showed the highly-stretachable ePTFE tubes ability for use in stent grafts. The stress-strain curve of ePTFE materials exhibited anisotropic behaviors as the membrane can be stretched up to 550% in radial direction while it showed negligible elongation in the longitudinal direction of the tube. The corresponding micro-structured porosity increased from 3% to 24% during the strain loading up to 550% in radial direction. Sweating test results showed that no leakage on the surface was observed under the fluid pressure of 120 mmHg, which demonstrated its reliability as a stent graft in the blood vessel. The early thrombogenic responses on ePTFE surface with 0%, 200% and 400% stretchiness level demonstrated that longer exposure time to the non-heparinized blood would lead to more blood cell adherence on the surface while the stretchiness level has no significant impact. In addition, no significant amount of coagulation was observed on the ePTFE surface with heparinized pig blood. The mechanical behaviors of nitinol stent backbone in terms of radial force and stent migration were investigated both in finite element analysis and *in vitro*. The radial force of the nitinol backbone when it was radially crimped by 40% was approximately 2.98 N, and the pullout force with the 50% oversized stent was measured as 2.65 N, which was sufficient for the stent graft. The prototype stent graft designed for bleeding control was then fabricated based on the computational modeling results using the integration process of the customized ePTFE and the laser-welded nitinol backbone. The venous size stent graft could be easily deployed and retrieved via a 9 Fr delivery sheath. Angiography results demonstrated that the deployed stent graft in the swine model showed successful bleeding control on the injured vessels. Gross look analysis showed the pristine surface of the harvest devices except a few locations with local moderate thrombosis.

The current study suggests that a highly-stretchable ePTFE tube is an excellent candidate material for the next-generation customizable stent graft improving the clinical outcomes as well as reducing the cost in device manufacturing.

6.0 SUMMARIES AND TAKEAWAYS

In this dissertation, four types of innovative implantable medical devices have been developed and evaluated. Although the functionality and materials for these devices are various, they share the same development process. A typical medical device, regardless of its functionality and behaviors, always start with the concept generated from clinical needs. The goal of developing novel implantable medical device is always to address the current unmet clinical needs or improve the performance of current treatment. Then different materials and structures need to be considered in terms of mechanical, biological and fluid behaviors before prototyping. Once the materials and device structures are determined, the prototypes can be fabricated using various manufacturing processes, such as traditional manufacturing including machining and advanced techniques including microfabrication and 3D printing. During the prototyping process, a few iterations in terms of CAD modeling, *in vitro* validations are always required to optimize the prototype devices. Finite element method is a power method to evaluate the device structural, mechanical and fluid behaviors in a complicated environment. Solidworks can be used to build the 3D model of prototype devices and then transferred to finite element analysis software such as ANSYS and ABAQUS for further analysis. The challenging issues in finite element analysis would be how to consider the realistic conditions inside the human body. As vascular systems inside the human body are highly complicated, it is critical to make assumptions to simplify our calculations during the computational modeling. Some knowledges and experiences are also helpful to get convergent solutions under complex boundary conditions and structures. Also the results from computational modeling need to be validated using *in vitro* tests to justify its assumptions. Once the prototype design is optimized, it will undergo pre-clinical testings including *in vitro* and *in vivo* evaluations. The testing system needs to be customized to meet the

specific device requirements. During this stage, multiple testing systems and devices such as mechanical tensile machines, load cells, pressure sensors and flow meters are available to measure the corresponding physiological signals, but they should be assembled appropriately as a whole testing system and should be able to mimic the human physiological conditions. Finally it is also important to validate the device designs in animal models before clinical testings and FDA approval.

My contributions of this dissertation include the 3D modeling and parameter optimizations in implantable medical device designs using finite element analysis software. Most of the finite element methods are structural analysis and computational fluid dynamics based on nitinol materials with superelastic properties. Also the customization of *in vitro* testing instrument was also proposed to evaluate different prototypes in terms of material properties, biocompatibility issues and structural behaviors.

APPENDIX

PUBLICATIONS

A.1 JOURNAL PUBLICATIONS

1. Howe, C., **Chen, Y.**, Mishra, S., Ye, S.,Wagner, W., Jeong, J., Byun, H., Kim, J., Chun, Y., Yeo W.H., Implantable, Nanomembrane Flow-Diverter System, *ACS Nano*, *under revision*, 2018.
2. **Chen, Y.**, Tillman, B.W., Go, C., Cho. S.K., Clark, W., Hur, T. B., Ding, Y., Chun, Y., A novel customizable stent graft that contains a stretchable ePTFE with a laser-welded nitinol stent, *Journal of Biomedical Materials Research: Part B - Applied Biomaterials*, *under review*, 2018.
3. **Chen, Y.**, Kim, Y.S., Tillman, B.W., Yeo, W.H., Chun, Y., Advances in Materials for Recent Low-Profile Implantable Bioelectronics, *Materials*, 11(4), 522, 2018.
4. Mishra, S., Norton, J.J., Lee, Y., Lee, D.S., Agee, N., **Chen, Y.**, Chun, Y., and Yeo, W.H., Soft, conformal bioelectronics for a wireless human-wheelchair interface. *Biosensors and Bioelectronics*, 91, 796-803, 2017.
5. Lee, Y., Nicholls, B., Lee, D.S., **Chen, Y.**, Chun, Y., Ang, C.S. and Yeo, W.H., Soft Electronics Enabled Ergonomic Human-Computer Interaction for Swallowing Training. *Scientific Reports*, 7: 46697, 2017.
6. Mishra, S., Norton, J.J., Lee, Y., Lee, D.S., Agee, N.,**Chen, Y.**, Chun, Y. and Yeo, W.H., Soft, conformal bioelectronics for a wireless human-wheelchair interface. *Biosensors and Bioelectronics*, 91, pp.796-803, 2017.

7. **Chen, Y.**, Tillman, B.W., Cho, S.K., Richards, T.D., Tevar, A.D., Gu, X., Wagner, W.R. and Chun, Y., A novel compartmentalised stent graft to isolate the perfusion of the abdominal organs. *Journal of Medical Engineering & Technology*, 41(2), 141-150, 2017.

8. **Chen, Y.**, Shayan, M., Yeo, W.H. and Chun, Y., Assessment of endothelial cell growth behavior in thin film nitinol. *BioChip Journal*, 1-7, 2016.

9. Chun, Y., Kealey, C.P., Levi, D.S., Rigberg, D.A., **Chen, Y.**, Tillman, B.W., Mohanchandra, K.P., Shayan, M. and Carman, G.P., An in vivo pilot study of a microporous thin film nitinol-covered stent to assess the effect of porosity and pore geometry on device interaction with the vessel wall. *Journal of Biomaterials Applications*, 0885328216682691, 2016.

10. Shayan, M., **Chen, Y.**, Shridhar, P., Kealey, C.P. and Chun, Y., In Vitro Study of a Superhydrophilic Thin Film Nitinol Endograft that is Electrostatically Endothelialized in the Catheter Prior to the Endovascular Procedure. *Journal of Functional Biomaterials*, 7(4), 31, 2016.

11. Tillman, B.W., Chun, Y., Cho, S.K., **Chen, Y.**, Liang, N., Maul, T., Demetris, A., Gu, X., Wagner, W.R. and Tevar, A.D., Dual chamber stent prevents organ malperfusion in a model of donation after cardiac death. *Surgery*, 160(4), 892-901, 2016.

12. Shridhar, P., **Chen, Y.**, Khalil, R., Plakseychuk, A., Cho, S.K., Tillman, B., Kumta, P.N. and Chun, Y., A Review of PMMA Bone Cement and Intra-Cardiac Embolism. *Materials*, 9(10), 821, 2016.

13. **Chen, Y.**, Emery, S.P., Maxey, A.P., Gu, X., Wagner, W.R. and Chun, Y., A novel low-profile ventriculoamniotic shunt for foetal aqueductal stenosis. *Journal of Medical Engineering & Technology*, 40(4), 186-198, 2016.

14. **Chen, Y.**, Howe, C., Lee, Y., Cheon, S., Yeo, W.H. and Chun, Y., Microstructured Thin Film Nitinol for a Neurovascular Flow-Diverter. *Scientific reports*, 6, 2016.

15. **Chen, Y.**, Jankowitz, B.T., Cho, S.K. and Yeo, W.H., Chun, Y., A novel low-profile flow sensor for monitoring of hemodynamics in cerebral aneurysm. *Biomater. Biomed. Eng*, 2, 071, 2015.

16. Barry, M.M., Shayan, M., Jankowitz, B.T., **Chen, Y.**, Duan, X., Robertson, A.M., Chyu, M.K. and Chun, Y., Smart Guidewires for Smooth Navigation in Neurovascular Intervention. Journal of Medical Devices, 9(1), 011011, 2015.

A.2 CONFERENCE PRESENTATIONS

1. **Chen, Y.**, Howe, C., Emery, S., Greene, S., Shridhar, P., Yeo, W.H., Chun, Y., A Low-Profile Flow Sensing System for Monitoring of Cerebrospinal Fluid with a New Ventriculoamniotic Shunt, 2017 IEEE 67th Electronic Components and Technology Conference (ECTC), Orlando, USA. 2017.
2. Howe, C., Lee, Y., **Chen, Y.**, Chun, Y. and Yeo, W.H., An Implantable, Stretchable Microflow Sensor Integrated with a Thin-Film Nitinol Stent. 2016 IEEE 66th Electronic Components and Technology Conference (ECTC), Las Vegas, USA. 2016.
3. **Chen, Y.**, Howe, C., Lee, Y., Chun, Y. and Yeo, W.H., Mechanical Behavior of a Thin Film Nitinol Covered Neurovascular Device, The Industrial and Systems Engineering Research Conference (ISERC), Anaheim, USA. 2016.
4. **Chen, Y.**, Barry, M.M., Shayan, M., Jankowitz, B.T., Duan, X., Robertson, A.M., Chyu, M.K. and Chun, Y., 2015, Smart guidewires for smooth navigation in neurovascular intervention. SPIE Smart Structures and Materials, San Diego, USA. 2015.
5. **Chen, Y.**, Jankowitz, B.T., Cho, S.K. and Chun, Y., A novel low profile wireless flow sensor to monitor hemodynamic changes in cerebral aneurysm, SPIE Smart Structures and Materials, San Diego, USA. 2015.
6. Barry, M.M., Shayan, M., Jankowitz, B.T., **Chen, Y.**, Duan, X., Robertson, A.M., Chyu, M.K. and Chun, Y., A Smart Guidewire for Smooth Navigation in Interventional Radiology, The Industrial and Systems Engineering Research Conference (ISERC), Montreal, Canada. 2014.

BIBLIOGRAPHY

[1] Implantable medical devices market analysis and trends - product, material - forecast to 2025, 2017. Accessed 03/29/2017.

[2] C Lee Ventola. Medical applications for 3d printing: current and projected uses. *PT*, 39(10):704–711, 2014.

[3] Kyung-In Jang, Sang Youn Han, Sheng Xu, Kyle E Mathewson, Yihui Zhang, Jae-Woong Jeong, Gwang-Tae Kim, R Chad Webb, Jung Woo Lee, Thomas J Dawidczyk, et al. Rugged and breathable forms of stretchable electronics with adherent composite substrates for transcutaneous monitoring. *Nature communications*, 5, 2014.

[4] AD Pye, DEA Lockhart, MP Dawson, CA Murray, and AJ Smith. A review of dental implants and infection. *Journal of Hospital infection*, 72(2):104–110, 2009.

[5] Ronald Lakatos. History of fracture treatment.

[6] F Burny, Monique Donkerwolcke, Françoise Moulart, R Bourgois, Robert Puers, K Van Schuylenbergh, M Barbosa, O Paiva, F Rodes, JB Bégueret, et al. Concept, design and fabrication of smart orthopedic implants. *Medical engineering & physics*, 22(7):469–479, 2000.

[7] Paul Didisheim, Don B Olsen, David J Farrar, Peer M Portner, Bartley P Griffith, D Glenn Pennington, J Heinrich Joist, Frederick J Schoen, Anthony G Gristina, and James M Anderson. Infections and thromboembolism with implantable cardiovascular devices. *ASAIO Journal*, 35(1):54–70, 1989.

[8] Jack T Holladay, Patricia A Piers, Gabor Koranyi, Marrie van der Mooren, and NE Sverker Norrby. A new intraocular lens design to reduce spherical aberration of pseudophakic eyes. *Journal of Refractive Surgery*, 18(6):683–691, 2002.

[9] Adrian JT Teo, Abhinay Mishra, Inkyu Park, Young-Jin Kim, Woo-Tae Park, and Yong-Jin Yoon. Polymeric biomaterials for medical implants and devices. *ACS Biomaterials Science & Engineering*, 2(4):454–472, 2016.

[10] Joseph R Davis. *Handbook of materials for medical devices*. ASM international, 2003.

[11] William J Buehler, JV Gilfrich, and RC Wiley. Effect of low-temperature phase changes on the mechanical properties of alloys near composition tini. *Journal of applied physics*, 34(5):1475–1477, 1963.

[12] A Szold. Nitinol: shape-memory and super-elastic materials in surgery. *Surgical endoscopy*, 20(9):1493–1496, 2006.

[13] LG Machado and MA Savi. Medical applications of shape memory alloys. *Brazilian journal of medical and biological research*, 36(6):683–691, 2003.

[14] TW Duerig, A Pelton, and D Stöckel. An overview of nitinol medical applications. *Materials Science and Engineering: A*, 273:149–160, 1999.

[15] Lenka L Stepan, Daniel S Levi, and Gregory P Carman. A thin film nitinol heart valve. *Journal of Biomechanical Engineering*, 127(6):915–918, 2005.

[16] Youngjae Chun, Daniel S Levi, KP Mohanchandra, Fernando Vinuela, and Gregory P Carman. Thin film nitinol microstent for aneurysm occlusion. *Journal of biomechanical engineering*, 131(5):051014, 2009.

[17] Dieter Stoeckel. Nitinol medical devices and implants. *Minimally invasive therapy & allied technologies*, 9(2):81–88, 2000.

[18] VE Gjunter, P Sysoliatin, and T Temerkhamor. Superelastic shape memory implants in maxillofacial surgery, traumatology, orthopaedics and neurosurgery. *Tomsk, Russia: Tomsk University Publishing House*, 15, 1995.

[19] Svetlana A Shabalovskaya. Surface, corrosion and biocompatibility aspects of nitinol as an implant material. *Bio-medical materials and engineering*, 12(1):69–109, 2002.

[20] TW Duerig, AR Pelton, and D Stöckel. The utility of superelasticity in medicine. *Bio-medical materials and engineering*, 6(4):255–266, 1996.

[21] Dieter Stoeckel, Alan Pelton, and Tom Duerig. Self-expanding nitinol stents: material and design considerations. *European radiology*, 14(2):292–301, 2004.

[22] J Ryhänen, EUOO Niemi, W Serlo, E Niemelä, P Sandvik, H Pernu, and T Salo. Biocompatibility of nickel-titanium shape memory metal and its corrosion behavior in human cell cultures. *Journal of Biomedical Materials Research Part A*, 35(4):451–457, 1997.

[23] Youngjae Chun, Daniel S Levi, KP Mohanchandra, and Gregory P Carman. Superhydrophilic surface treatment for thin film niti vascular applications. *Materials Science and Engineering: C*, 29(8):2436–2441, 2009.

[24] Allan W Tulloch, Youngjae Chun, Daniel S Levi, Kotekar P Mohanchandra, Gregory P Carman, Peter F Lawrence, and David A Rigberg. Super hydrophilic thin film nitinol

demonstrates reduced platelet adhesion compared with commercially available endograft materials. *Journal of Surgical Research*, 171(1):317–322, 2011.

[25] C Lally, Fl Dolan, and PJ Prendergast. Cardiovascular stent design and vessel stresses: a finite element analysis. *Journal of biomechanics*, 38(8):1574–1581, 2005.

[26] Wei Wu, Wei-Qiang Wang, Da-Zhi Yang, and Min Qi. Stent expansion in curved vessel and their interactions: a finite element analysis. *Journal of biomechanics*, 40(11):2580–2585, 2007.

[27] Wei Wu, Min Qi, Xiao-Peng Liu, Da-Zhi Yang, and Wei-Qiang Wang. Delivery and release of nitinol stent in carotid artery and their interactions: a finite element analysis. *Journal of Biomechanics*, 40(13):3034–3040, 2007.

[28] Ferdinando Auricchio, Michele Conti, Matthieu De Beule, Gianluca De Santis, and Benedict Verhegghe. Carotid artery stenting simulation: from patient-specific images to finite element analysis. *Medical engineering & physics*, 33(3):281–289, 2011.

[29] E Fernell, B Hagberg, G Hagberg, and L von Wendt. Epidemiology of infantile hydrocephalus in sweden. *Acta Paediatrica*, 76(3):411–417, 1987.

[30] Sergio Cavalheiro, Antonio Fernandes Moron, Carlos Gilberto Almodin, Italo Capraro Suriano, Vagner Hisaba, Patricia Dastoli, and Mauricio Mendes Barbosa. Fetal hydrocephalus. *Child's Nervous System*, 27(10):1575–1583, 2011.

[31] Ester Garne, Maria Loane, Marie-Claude Addor, Patricia A Boyd, Ingeborg Barisic, and Helen Dolk. Congenital hydrocephalus–prevalence, prenatal diagnosis and outcome of pregnancy in four european regions. *european journal of paediatric neurology*, 14(2):150–155, 2010.

[32] Therese Hannon, Peter WG Tennant, Judith Rankin, and Stephen C Robson. Epidemiology, natural history, progression, and postnatal outcome of severe fetal ventriculomegaly. *Obstetrics & Gynecology*, 120(6):1345–1353, 2012.

[33] Susy Jeng, Nalin Gupta, Margaret Wrensch, Shoujun Zhao, and Yvonne W Wu. Prevalence of congenital hydrocephalus in california, 1991-2000. *Pediatric neurology*, 45(2):67–71, 2011.

[34] Arie Drugan, Brian Krause, Alexa Canady, Ivan E Zador, Alan J Sacks, and Mark I Evans. The natural history of prenatally diagnosed cerebral ventriculomegaly. *Jama*, 261(12):1785–1788, 1989.

[35] Frank A Manning. International fetal surgery registry: 1985 update. *Clinical obstetrics and gynecology*, 29(3):551–557, 1986.

[36] Frank A Manning, Michael R Harrison, and Charles Rodeck. Catheter shunts for fetal hydronephrosis and hydrocephalus. *New England Journal of Medicine*, 315(5):336–340, 1986.

[37] Stephen P Emery, W Allen Hogge, and Lyndon M Hill. Accuracy of prenatal diagnosis of isolated aqueductal stenosis. *Prenatal diagnosis*, 35(4):319–324, 2015.

[38] Kyoko Hayashida, Keiichi Kanda, Hitoshi Yaku, Joji Ando, and Yasuhide Nakayama. Development of an in vivo tissue-engineered, autologous heart valve (the biovalve): preparation of a prototype model. *The Journal of thoracic and cardiovascular surgery*, 134(1):152–159, 2007.

[39] Jianjun Guan, Michael S Sacks, Eric J Beckman, and William R Wagner. Synthesis, characterization, and cytocompatibility of elastomeric, biodegradable poly (ester-urethane) ureas based on poly (caprolactone) and putrescine. *Journal of Biomedical Materials Research Part A*, 61(3):493–503, 2002.

[40] John J Stankus, Jianjun Guan, and William R Wagner. Fabrication of biodegradable elastomeric scaffolds with sub-micron morphologies. *Journal of biomedical materials research Part A*, 70(4):603–614, 2004.

[41] IG Bloomfield, IH Johnston, and LE Bilston. Effects of proteins, blood cells and glucose on the viscosity of cerebrospinal fluid. *Pediatric neurosurgery*, 28(5):246–251, 1998.

[42] Susan S Margulies and Kirk L Thibault. Infant skull and suture properties: measurements and implications for mechanisms of pediatric brain injury. *Transactions-American Society of Mechanical Engineers Journal of Biomechanical Engineering*, 122(4):364–371, 2000.

[43] Brittany Coats and Susan S Margulies. Material properties of human infant skull and suture at high rates. *Journal of neurotrauma*, 23(8):1222–1232, 2006.

[44] Pim NM Mooij, Jan G Nijhuis, Henk W Jongsma, and Jan JM Menssen. Intracranial pressure and fetal heart rate in a hydrocephalic fetus during labor. *European Journal of Obstetrics & Gynecology and Reproductive Biology*, 43(2):161–165, 1992.

[45] Ioannis G Sideris and Kypros H Nicolaides. Amniotic fluid pressure during pregnancy. *Fetal diagnosis and therapy*, 5(2):104–108, 1990.

[46] Andreas A Linninger, Michalis Xenos, David C Zhu, MahadevaBharath R Somayaji, Srinivasa Kondapalli, and Richard D Penn. Cerebrospinal fluid flow in the normal and hydrocephalic human brain. *IEEE Transactions on Biomedical Engineering*, 54(2):291–302, 2007.

[47] Fredric D Frigoletto, Jason C Birnholz, and Michael F Greene. Antenatal treatment of hydrocephalus by ventriculoamniotic shunting. *JAMA*, 248(19):2496–2497, 1982.

[48] Yuki Uohashi, Koichi Suzumori, and Hironari Taniguchi. Fabrication and evaluation of various types of micro one-way valves through micro rubber molding process. *Journal of mechanical science and technology*, 24(1):219–222, 2010.

[49] JM Wardlaw and PM White. The detection and management of unruptured intracranial aneurysms. *Brain*, 123(2):205–221, 2000.

[50] Jonathan L Brisman, Joon K Song, and David W Newell. Cerebral aneurysms. *New England Journal of Medicine*, 355(9):928–939, 2006.

[51] Andrew Molyneux, International Subarachnoid Aneurysm Trial (ISAT) Collaborative Group, et al. International subarachnoid aneurysm trial (isat) of neurosurgical clipping versus endovascular coiling in 2143 patients with ruptured intracranial aneurysms: a randomised trial. *The Lancet*, 360(9342):1267–1274, 2002.

[52] Jean Raymond, François Guilbert, Alain Weill, Stavros A Georganos, Louis Juravsky, Anick Lambert, Julie Lamoureux, Miguel Chagnon, and Daniel Roy. Long-term angiographic recurrences after selective endovascular treatment of aneurysms with detachable coils. *Stroke*, 34(6):1398–1403, 2003.

[53] Waleed Brinjikji, Mohammad H Murad, Giuseppe Lanzino, Harry J Cloft, and David F Kallmes. Endovascular treatment of intracranial aneurysms with flow diverters. *Stroke*, 44(2):442–447, 2013.

[54] S Claiborne Johnston, Christopher F Dowd, Randall T Higashida, Michael T Lawton, Gary R Duckwiler, Daryl R Gress, et al. Predictors of rehemorrhage after treatment of ruptured intracranial aneurysms. *Stroke*, 39(1):120–125, 2008.

[55] Nuno V Dias, Krassi Ivancev, Martin Malina, Jan-Willem Hinnen, Michel Visser, Bengt Lindblad, and Björn Sonesson. Direct intra-aneurysm sac pressure measurement using tip-pressure sensors: in vivo and in vitro evaluation. *Journal of vascular surgery*, 40(4):711–716, 2004.

[56] Sharif H Ellozy, Alfio Carroccio, Robert A Lookstein, Michael E Minor, Claudie M Sheahan, Jacob Juta, Andrew Cha, Rolando Valenzuela, Michael D Addis, Tikva S Jacobs, et al. First experience in human beings with a permanently implantable intrasac pressure transducer for monitoring endovascular repair of abdominal aortic aneurysms. *Journal of vascular surgery*, 40(3):405–412, 2004.

[57] Takao Ohki, Kenneth Ouriel, Pierre Galvagni Silveira, Barry Katzen, Rodney White, Frank Criado, and Edward Diethrich. Initial results of wireless pressure sensing for endovascular aneurysm repair: the apex trialacute pressure measurement to confirm aneurysm sac exclusion. *Journal of vascular surgery*, 45(2):236–242, 2007.

[58] Hans G Boecher-Schwarz, Kurt Ringel, Laszlo Kopacz, Axel Heimann, and Oliver Kempski. Ex vivo study of the physical effect of coils on pressure and flow dynamics in experimental aneurysms. *American journal of neuroradiology*, 21(8):1532–1536, 2000.

[59] Gádor Cantón, David I Levy, and Juan C Lasheras. Changes in the intraaneurysmal pressure due to hydrocoil embolization. *American journal of neuroradiology*, 26(4):904–907, 2005.

[60] Angelika Sorteberg, Wilhelm Sorteberg, Aquilla S Turk, Alan Rappe, Per Hj Nakstad, and Charles M Strother. Effect of guglielmi detachable coil placement on intraaneurysmal pressure: experimental study in canines. *American journal of neuroradiology*, 22(9):1750–1756, 2001.

[61] Alexander KN Lam, Match WL Ko, Leo KK Leung, John CK Kwok, Mathew MF Yuen, and David CC Lam. Characterization of pressure reduction in coil-filled aneurysm under flow of human blood with and without anti-coagulant. In *Engineering in Medicine and Biology Society (EMBC), 2013 35th Annual International Conference of the IEEE*, pages 739–742. IEEE, 2013.

[62] Christoph Groden, Jochen Laudan, Scott Gatchell, and Herrmann Zeumer. Three-dimensional pulsatile flow simulation before and after endovascular coil embolization of a terminal cerebral aneurysm. *Journal of Cerebral Blood Flow & Metabolism*, 21(12):1464–1471, 2001.

[63] Woosik Lee, Ohjin Kwon, Dong Sup Lee, and Woon-Hong Yeo. Fabrication and characterization of a conformal skin-like electronic system for quantitative, cutaneous wound management. *Journal of visualized experiments: JoVE*, (103), 2015.

[64] Kenichi Takahata and Yogesh B Gianchandani. A micromachined capacitive pressure sensor using a cavity-less structure with bulk-metal/elastomer layers and its wireless telemetry application. *Sensors*, 8(4):2317–2330, 2008.

[65] Yoshiaki Hattori, Leo Falgout, Woosik Lee, Sung-Young Jung, Emily Poon, Jung Woo Lee, Ilyoun Na, Amelia Geisler, Divya Sadhwani, Yihui Zhang, et al. Multifunctional skin-like electronics for quantitative, clinical monitoring of cutaneous wound healing. *Advanced healthcare materials*, 3(10):1597–1607, 2014.

[66] C Kleinstreuer, Z Li, CA Basciano, S Seelecke, and Mark A Farber. Computational mechanics of nitinol stent grafts. *Journal of biomechanics*, 41(11):2370–2378, 2008.

[67] P Barrett and Patrick Cunningham. Super elastic alloy eyeglass frame design using the ansys® workbench environment. *Computer Aided Engineering Associates Inc*, pages 1–11, 2004.

[68] Yanfei Chen, Connor Howe, Yongkuk Lee, Seongsik Cheon, Woon-Hong Yeo, and Youngjae Chun. Microstructured thin film nitinol for a neurovascular flow-diverter. *Scientific reports*, 6:23698, 2016.

[69] Youngjae Chun, Soojung Claire Hur, Colin P Kealey, Daniel S Levi, KP Mohanchandra, Dino Di Carlo, Jeff D Eldredge, Fernando Vinuela, and Gregory P Carman. Intra-aneurysmal flow reductions in a thin film nitinol flow diverter. *Smart Materials and Structures*, 20(5):055021, 2011.

[70] Youngjae Chun, Po-Yu Lin, Hsin-Yun Chang, Michael C Emmons, KP Mohanchandra, Daniel S Levi, and Gregory P Carman. Modeling and experimental analysis of the

hyperelastic thin film nitinol. *Journal of Intelligent Material Systems and Structures*, 22(17):2045–2051, 2011.

[71] Jiří Bočan, Jan Maňák, and Aleš Jäger. Nanomechanical analysis of az31 magnesium alloy and pure magnesium correlated with crystallographic orientation. *Materials Science and Engineering: A*, 644:121–128, 2015.

[72] Yongkuk Lee, Benjamin Nicholls, Dong Sup Lee, Yanfei Chen, Youngjae Chun, Chee Siang Ang, and Woon-Hong Yeo. Soft electronics enabled ergonomic human-computer interaction for swallowing training. *Scientific Reports*, 7:46697, 2017.

[73] Kun Kelvin Fu, Zhengyang Wang, Jiaqi Dai, Marcus Carter, and Liangbing Hu. Transient electronics: Materials and devices. *Chemistry of Materials*, 28(11):3527–3539, 2016.

[74] Jonathan A Fan, Woon-Hong Yeo, Yewang Su, Yoshiaki Hattori, Woosik Lee, Sung-Young Jung, Yihui Zhang, Zhuangjian Liu, Huanyu Cheng, Leo Falgout, et al. Fractal design concepts for stretchable electronics. *Nature communications*, 5:3266, 2014.

[75] W Wu, L Petrini, D Gastaldi, T Villa, M Vedani, E Lesma, B Previtali, and F Migliavacca. Finite element shape optimization for biodegradable magnesium alloy stents. *Annals of biomedical engineering*, 38(9):2829–2840, 2010.

[76] Organ procurement and transplantation network, 2016. Accessed 02/26/2016.

[77] RF Saidi, J Bradley, D Greer, R Luskin, K OConnor, F Delmonico, P Kennealey, F Pathan, C Schuetz, N Elias, et al. Changing pattern of organ donation at a single center: are potential brain dead donors being lost to donation after cardiac death? *American Journal of Transplantation*, 10(11):2536–2540, 2010.

[78] James L Bernat, Anthony M D'Alessandro, Friedrich K Port, Thomas P Bleck, Stephen O Heard, Justine Medina, Stanley H Rosenbaum, Michael A Devita, Robert S Gaston, Robert M Merion, et al. Report of a national conference on donation after cardiac death. *American Journal of Transplantation*, 6(2):281–291, 2006.

[79] Juan C García-Valdecasas. Dcd donors: A unique source to significantly increase organ donation. *Journal of hepatology*, 55(4):745–746, 2011.

[80] AS Klein, EE Messersmith, LE Ratner, R Kochik, PK Baliga, and AO Ojo. Organ donation and utilization in the united states, 1999–2008. *American Journal of Transplantation*, 10(4p2):973–986, 2010.

[81] AWN Reid, Simon Harper, Chris H Jackson, AC Wells, DM Summers, O Gjorgjimajkoska, LD Sharples, JA Bradley, and GJ Pettigrew. Expansion of the kidney donor pool by using cardiac death donors with prolonged time to cardiorespiratory arrest. *American Journal of Transplantation*, 11(5):995–1005, 2011.

[82] Hani P Grewal, Darrin L Willingham, Justin Nguyen, Winston R Hewitt, Bucin C Taner, Danielle Cornell, Barry G Rosser, Andrew P Keaveny, Jamie Aranda-Michel, Raj Satyanarayana, et al. Liver transplantation using controlled donation after cardiac death donors: An analysis of a large single-center experience. *Liver Transplantation*, 15(9):1028–1035, 2009.

[83] Anton I Skaro, Colleen L Jay, Talia B Baker, Edward Wang, Sarina Pasricha, Vadim Lyuksemburg, John A Martin, Joseph M Feinglass, Luke B Preczewski, and Michael M Abecassis. The impact of ischemic cholangiopathy in liver transplantation using donors after cardiac death: the untold story. *Surgery*, 146(4):543–553, 2009.

[84] David J Reich and Johnny C Hong. Current status of donation after cardiac death liver transplantation. *Current opinion in organ transplantation*, 15(3):316–321, 2010.

[85] Rebecca A Snyder, Deonna R Moore, and Derek E Moore. More donors or more delayed graft function? a cost-effectiveness analysis of dcd kidney transplantation. *Clinical transplantation*, 27(2):289–296, 2013.

[86] Robert M Merion, Shawn J Pelletier, Nathan Goodrich, Michael J Englesbe, and Francis L Delmonico. Donation after cardiac death as a strategy to increase deceased donor liver availability. *Annals of surgery*, 244(4):555–562, 2006.

[87] Ayyaz Ali, Paul White, Kumud Dhital, Marian Ryan, Steven Tsui, and Stephen Large. Cardiac recovery in a human non–heart-beating donor after extracorporeal perfusion: source for human heart donation? *The Journal of Heart and Lung Transplantation*, 28(3):290–293, 2009.

[88] MT Gravel, JD Arenas, R Chenault 2nd, JC Magee, S Rudich, M Maraschio, M DebRoy, W Miller, and JD Punch. Kidney transplantation from organ donors following cardiopulmonary death using extracorporeal membrane oxygenation support. *Annals of transplantation: quarterly of the Polish Transplantation Society*, 9(1):57–58, 2003.

[89] Jong Hoon Lee, Sung Yeon Hong, Chang-Kwon Oh, You Sun Hong, and Hyunee Yim. Kidney transplantation from a donor following cardiac death supported with extracorporeal membrane oxygenation. *Journal of Korean medical science*, 27(2):115–119, 2012.

[90] Mohamed S Noormohamed, Aditya Kanwar, Christopher Ray, Matthew C Wright, David E Cowie, Susan Stamp, David Talbot, Derek Manas, and Steven A White. Extracorporeal membrane oxygenation for resuscitation of deceased cardiac donor livers for hepatocyte isolation. *journal of surgical research*, 183(2):e39–e48, 2013.

[91] Crane. *Flow of fluids: through valves, fittings, and pipe*. 1977.

[92] SK Samijo, JM Willigers, R Barkhuysen, PJEHM Kitslaar, RS Reneman, PJ Brands, and APG Hoeks. Wall shear stress in the human common carotid artery as function of age and gender. *Cardiovascular research*, 39(2):515–522, 1998.

[93] Rajesh N Maniar and Tushar Singhi. Patient specific implants: scope for the future. *Current reviews in musculoskeletal medicine*, 7(2):125–130, 2014.

[94] Vincent Y Ng, Jeffrey H DeClaire, Keith R Berend, Bethany C Gulick, and Adolph V Lombardi. Improved accuracy of alignment with patient-specific positioning guides compared with manual instrumentation in tka. *Clinical Orthopaedics and Related Research®*, 470(1):99–107, 2012.

[95] A Dawood, B Marti Marti, V Sauret-Jackson, and A Darwood. 3d printing in dentistry. *British dental journal*, 219(11):521, 2015.

[96] Jim Banks. Adding value in additive manufacturing: researchers in the united kingdom and europe look to 3d printing for customization. *IEEE pulse*, 4(6):22–26, 2013.

[97] Emilia Mikołajewska, Marek Macko, Łukasz Ziarnecki, Sonia Stańczak, Patryk Kawalec, and Dariusz Mikołajewski. 3d printing technologies in rehabilitation engineering. 2014.

[98] Richard Van Noort. The future of dental devices is digital. *Dental materials*, 28(1):3–12, 2012.

[99] Nanfang Xu, Feng Wei, Xiaoguang Liu, Liang Jiang, Hong Cai, Zihe Li, Miao Yu, Fengliang Wu, and Zhongjun Liu. Reconstruction of the upper cervical spine using a personalized 3d-printed vertebral body in an adolescent with ewing sarcoma. *Spine*, 41(1):E50–E54, 2016.

[100] Philip Tack, Jan Victor, Paul Gemmel, and Lieven Annemans. 3d-printing techniques in a medical setting: a systematic literature review. *Biomedical engineering online*, 15(1):115, 2016.

[101] Michael P Chae, Warren M Rozen, Paul G McMenamin, Michael W Findlay, Robert T Spychal, and David J Hunter-Smith. Emerging applications of bedside 3d printing in plastic surgery. *Frontiers in surgery*, 2:25, 2015.

[102] Fabian Rengier, Amit Mehndiratta, Hendrik Von Tengg-Kobligk, Christian M Zechmann, Roland Unterhinninghofen, H-U Kauczor, and Frederik L Giesel. 3d printing based on imaging data: review of medical applications. *International journal of computer assisted radiology and surgery*, 5(4):335–341, 2010.

[103] Mahdis Shayan and Youngjae Chun. An overview of thin film nitinol endovascular devices. *Acta biomaterialia*, 21:20–34, 2015.

[104] Andreas A Giannopoulos, Dimitris Mitsouras, Shi-Joon Yoo, Peter P Liu, Yiannis S Chatzizisis, and Frank J Rybicki. Applications of 3d printing in cardiovascular diseases. *Nature Reviews Cardiology*, 13(12):701, 2016.

[105] Matthew DBS Tam, Stephen D Laycock, James RI Brown, and Matthew Jakeways. 3d printing of an aortic aneurysm to facilitate decision making and device selection

for endovascular aneurysm repair in complex neck anatomy. *Journal of Endovascular Therapy*, 20(6):863–867, 2013.

[106] Matthew D Tam, Thomas Latham, James RI Brown, and Matthew Jakeways. Use of a 3d printed hollow aortic model to assist evar planning in a case with complex neck anatomy: potential of 3d printing to improve patient outcome. *Journal of Endovascular Therapy*, 21(5):760–762, 2014.

[107] Richard R Saxon, Jeanine M Coffman, Justin M Gooding, Eileen Natuzzi, and Donald J Ponec. Long-term results of eptfe stent-graft versus angioplasty in the femoropopliteal artery: single center experience from a prospective, randomized trial. *Journal of vascular and interventional radiology*, 14(3):303–311, 2003.

[108] Thomas Bürger, Frank Meyer, Jörg Tautenhahn, Zuhir Halloul, and Jörg Fahlke. Initial experiences with percutaneous endovascular repair of popliteal artery lesions using a new ptfe stent-graft. *Journal of Endovascular Therapy*, 5(4):365–372, 1998.

[109] Mark Davidian, Stephen T Kee, Noriuki Kato, Charles P Semba, Mahmood K Razavi, R Scott Mitchell, and Michael D Dake. Aneurysm of an aberrant right subclavian artery: treatment with ptfe covered stentgraft. *Journal of vascular surgery*, 28(2):335–339, 1998.

[110] Mahmood K Razavi, Michael D Dake, Charles P Semba, UR Nyman, and Robert P Liddell. Percutaneous endoluminal placement of stent-grafts for the treatment of isolated iliac artery aneurysms. *Radiology*, 197(3):801–804, 1995.

[111] Nahel Farraj, A Srivastava, and Ashish Pershad. One-year outcomes for recanalization of long superficial femoral artery chronic total occlusions with the viabahn stent graft. *The Journal of invasive cardiology*, 21(6):278–281, 2009.

[112] Juan C Parodi, JC Palmaz, and HD Barone. Transfemoral intraluminal graft implantation for abdominal aortic aneurysms. *Annals of vascular surgery*, 5(6):491–499, 1991.

[113] Kenneth D Murphy, Goetz M Richter, Michel Henry, Carlos E Encarnacion, Van A Le, and Julio C Palmaz. Aortoiliac aneurysms: management with endovascular stent-graft placement. *Radiology*, 198(2):473–480, 1996.

[114] Zvonimir Krajcer and Edward B Diethrich. Successful endoluminal repair of arterial aneurysms by wallstent prosthesis and ptfe graft: preliminary results with a new technique. *Journal of Endovascular Therapy*, 4(1):80–87, 1997.

[115] Youngjae Chun, Sung Kwon Cho, William C Clark, William R Wagner, Xinzhu Gu, Amit D Tevar, Ryan M McEnaney, and Bryan W Tillman. A retrievable rescue stent graft and radiofrequency positioning for rapid control of noncompressible hemorrhage. *Journal of Trauma and Acute Care Surgery*, 83(2):249–255, 2017.

[116] Mehreen Kisat, Jonathan J Morrison, Zain G Hashmi, David T Efron, Todd E Rasmussen, and Adil H Haider. Epidemiology and outcomes of non-compressible torso hemorrhage. *journal of surgical research*, 184(1):414–421, 2013.

[117] Joseph Mummert, Eric Sirois, and Wei Sun. Quantification of biomechanical interaction of transcatheter aortic valve stent deployed in porcine and ovine hearts. *Annals of biomedical engineering*, 41(3):577–586, 2013.

[118] Siddharth Vad, Amanda Eskinazi, Timothy Corbett, Tim McGloughlin, and Jonathan P Vande Geest. Determination of coefficient of friction for self-expanding stent-grafts. *Journal of biomechanical engineering*, 132(12):121007, 2010.

[119] Bryan W Tillman, Youngjae Chun, Sung Kwon Cho, Yanfei Chen, Nathan Liang, Timothy Maul, Anthony Demetris, Xinzhu Gu, William R Wagner, and Amit D Tevar. Dual chamber stent prevents organ malperfusion in a model of donation after cardiac death. *Surgery*, 160(4):892–901, 2016.